Cranfield University

Computational Modelling of Environmental Flows Featuring Gas Dispersion

Loukia Gerousi

Department of Aerospace Sciences
School of Engineering

Cranfield University
Cranfield, UK

MSc by Research Thesis
School of Engineering

Computational Modelling of Environmental Flows Featuring Gas Dispersion

Loukia Gerousi

Supervisors: Dr. Sanjay Patel
Prof. Dimitris Drikakis

July 2010

Acknowledgments

First of all, I wish to express my gratitude to Professor Dimitris Drikakis for his advice and assistance throughout this year. My heartfelt thanks to Dr. Nikos Nikiforakis, for his invaluable help and support on any difficulties that I faced at any time. I would like to thank Dr. Evgeniy Shapiro and Dr. Ben Thornber for the useful instructions and recommendations they provided for my thesis. In addition, I would like to include in my acknowledgments my friends, who helped me and were my enduring “fellow-travellers” all this time. Finally, I would like to thank my family for their precious support, encouragement and for everything they have done for me all these years.

I dedicate this thesis to my mum, my dad, my brother, my family and Angelos.

Abstract

This study particularly aims at understanding flow and pollutant dispersion when flat terrain, single hill and hill with obstacles are present. The emissions of ethylene from a point source are located in eight different positions. For the hill cases, the sources are located downwind from the top of the hill, and the data are collected at various locations.

The commercial software packages Gambit 2.4.6, Fluent 6.3.26 and Tecplot 360 are used for the two-dimensional mesh generation, for the flow simulation and for the validation respectively. The numerical results are compared with experimental and numerical data for the single hill case and for the point source using the Spalart-Allmaras model, k-ε Standard, k-ε RNG and k-ε Realizable models. The comparison of the results shows that the k-ε Standard model is in good agreement with the experimental and numerical data.

Results also show that the mass fraction of ethylene is highest for the flat terrain case. The next highest mass fraction of ethylene is found for the case with the hill and obstacles, and the single-hill case has the lowest. Moreover, upwind of the first obstacle the average mass fraction is larger than inside the first and the second canyons, and the minimum pollutant is downwind of the last obstacle. The average mass fraction of ethylene is measured at the corners of the canyons, and the results show that generally the bottom left corners have a higher mass fraction than the middle and bottom right side.

List of Contents

Chapter 6

Chapter 7

Chapter 8

List of Figures

List of Tables

Nomenclature

A	Flow area
A_o, A_s	Functions of velocity gradients
C_{b1}	Spalart-Allmaras Turbulence model constant
C_{b2}	Spalart-Allmaras Turbulence model constant
C_{v1}	Spalart-Allmaras Turbulence model constant
$C_{1\varepsilon}$	k-ε Standard, RNG and Realizable Turbulence models constant
$C_{2\varepsilon}$	k-ε Standard and RNG Turbulence model constant
C_2	k-ε Realizable Turbulence model constant
D_h	Hydraulic Diameter
G_b	Generation of turbulence kinetic energy due to buoyancy
H	Hill Height
H_d	Height of the domain
k	Turbulent kinetic energy
l	Characteristic length
$\dot{m}$	Mass fraction
p	Pressure
Re	Reynolds number
T	Time
u,v	Components of the velocity vector in x and y direction.
x,y	Cartesian coordinates
U^*	Friction velocity
U_∞, U_0	Free stream velocity
U	Mean velocity
y^+	Mesh dependent dimensionless, sublayer scaled distance
W_d	Width of the domain
Z_o	Roughness length

Greek Letters

α_k	k-ε RNG Turbulence model constant
α_ε	k-ε RNG Turbulence model constant
ε	Turbulence dissipation rate
κ	Karman constant
μ_τ	Turbulent viscosity
μ_{eff}	Effective viscosity (μ+μt)
ν	Kinematic viscosity
$\tilde{\nu}$	Molecular kinematic viscosity
ρ	Density
σ_κ	k-ε Standard Turbulence model constant
σ_ε	k-ε Standard and Realizable Turbulence models constant
σ_{w1}	Spalart-Allmaras Turbulence model constant

Abbreviations

ABL	Atmospheric Boundary Layer
CFD	Computational Fluid Dynamics
LNG	Liquid Natural Gas
RANS	Reynolds-Averaged Navier-Stokes
RNG	Renormalisation Group
UDF	User Defined Function

Chapter 1

1. Introduction

Environmental pollution is the contamination of the physical and biological components of the atmosphere system to such an extent that normal environmental processes are adversely affected. Contamination effects are certainly many and wide ranging and can cause damage to humans or other living organisms or instability to the ecosystem. All types of pollutant, air, water, soil pollution, have an impact on the living environment.

Sources of contamination can be summarized in three categories:

1. Agricultural: It affects urban areas due to the use of pesticides, insecticides that increase the pollutant in soils. Previous agricultural areas that have been urbanized have remains of such chemicals and have high chances of water contamination of water supplies and soils [1].
2. Urban: Contamination can be caused by restructuring the land surface (building and road construction), extensive use of gasoline, smokestacks, vehicle exhaust fumes, industrial activities.
3. Industrial: Contamination can be caused by the usage of toxic materials, by the industries. Even in the occasion of moving or closing down the particular industrial sites, the areas have already been contaminated, making almost impossible the use of land for other purposes without expensive clean-up. This can have serious effects on people living in such areas.

All three categories consist of the major threats of the environment. Surrounding areas can also get polluted, due to the transport of emissions through the atmosphere [2]. Also because of the increasing amounts of pollutants in the atmosphere, and the dangers those pollutants can hide, make it imperative for thorough studies of atmospheric flow and dispersion near urban areas [3]. Furthermore, other reasons for environmental pollution are “terrorist attack”, which for instance can be biological or chemical [4] and natural events like volcanic eruptions and sandstorms [5].

A large amount of the worldwide population lives in urban areas and air pollution is increasing more and more each year. This evolution has lately inspired many urban studies. Air pollution is related to meteorology and topography of each area. Dispersion of gases is crucial for the safety of people in the urban areas.

Computational fluid dynamics (CFD) provides a solution through the simulations of gas emission in geometrically complex situations and is a technique that can be applied in both industrial and non-industrial areas. CFD is a tool for the analysis of systems involving fluid flow, turbulent flows, heat transfer and associated phenomena such as chemical reactions, and is based on simulations.

Turbulent flows can be observed through various means, during our everyday life, such as a smoke from a chimney, a waterfall, water in an ocean, sea, lake or wind. For more detailed observations of this phenomenon the above can be examined in laboratories. In the processing of liquids or gases with pumps, compressors, pipe lines, vehicles, airplanes, the flows are generally turbulent. In engineering application turbulent flows are prevalent, but less easily seen. An important characteristic of turbulence is its ability to transport and mix fluid much more effectively than a comparable laminar flow. Different models have already been used in order to study CFD. All these models meet some criteria, such as the level of description, cost and ease of use, range of applicability, and the accuracy.

There are different ways of studying turbulent flows using CFD and the most commonly applicable methods today are based on the principles of Direct Numerical Simulation (DNS), Large-eddy simulation (LES) and Reynolds-Averaged Navier-Stokes (RANS) [6].

Direct numerical simulations (DNS) consist of solving the Navier-Stokes equations directly in all scales of turbulent motions. DNS verify the instantaneous velocity from which all the other information can be determined from that for one realization of the flow. Additionally, because all the scales of motion need to be resolved, in high Reynolds numbers where there is great difference between the small and large scales, the computational cost increases rapidly. The computational difficulty decreases if the flow is stationary and decreases even more if boundary layer equations can be used. In order to calculate the turbulent flows the consideration of the computer programs to solve the model equations should be considered and developed. The cost and the difficulty depend on the available software, algorithms and the complexity of the model. In addition, another reason for the cost and

difficulty of DNS is due to the accomplishment of the computer program to perform the calculations and the results to be extracted. This depends on the amount of human time, skill needed to perform the computation and the available computer resources.

In Large-eddy simulation (LES) the effect of the smaller scale motions are modelled and superior to simulate the flow near the wall. This requires a very fine grid next to the wall. LES is a method that solves the Navier-Stokes equation with a filtering operator in order to decompose the instantaneous velocity into the sum of a filtered component of the velocity. The filtered velocity field, represents the motion of the largest eddies and provides as well an approximation to the large scale motions in one realization of the turbulent flow. This method is based on a filtering technique that cuts off the small scales of turbulence and resolves the bigger ones. LES requires less computational effort than DNS but more effort than those methods that solve the RANS. The computational demands also increase significantly in the vicinity of walls, and simulating such flows usually exceeds the limits of modern supercomputers today.

The Reynolds-averaged Navier-Stokes (RANS) equations are ensemble averaged equations of motion for fluid flow. This method is based on the Reynolds decomposition, the flow variables are split into the sum of mean and fluctuating components. Reynolds stresses are obtained from a turbulent viscosity model. Due to the low requirements in computational power, RANS has become the preferred approach in engineering applications. It has applications particularly to high Reynolds flows, where the methodology underlying DNS and LES is not realizable economically.

This study is based on RANS because they are computationally less expensive and the computational time is less from the other two models. The purpose of this work is to analyze the performance of various RANS models on flows around a single hill and aims to understand the flow and pollutant dispersion at flat terrain, single hill and hill with obstacles. The emissions are located in eight different positions and for the hill cases the sources are located downwind from the top of the hill.

To understand the flow and the dispersion of pollutant in a complex terrain a study of flow and dispersion should be done firstly for a simple topography. In any air pollution study, firstly it is necessary to have information about wind directions and speed. The reason applying those measures in the CFD model is to estimate concentrations of pollutant at any distance from the source of the emission. The

capacity to dilute pollutants depends on the speed of the wind and this has the effect to determine the concentrations of pollutant [7].

For many years in CFD various models have been used. The desirable target of this use of models is to understand environmental flows and dispersion of pollutant in urban areas. The new and improved boundary conditions have the specificity to take more into account the atmospheric boundary layer called also the friction layer or the 'roughness layer' near the ground. The roughness of the terrain surface will influence the wind speed and the dispersion of pollutants and as a result any study's metrics. A main factor to consider for any simulation in CFD is the influence of the terrain. This occurs due to the fact that the ground level concentrations will be affected by any land elevations and high turbulences can be caused by a very steep terrain. Topography and urban influences have to be considered with caution because of the impact on the wind speed and pollutant dispersion. In most of the urban areas the tall buildings affect the airflow and the transport of pollutants. The main reason for this is that a recirculation or cavity zone is generated next to the buildings, when an air stream gets too close to them. In this region a highly turbulent flow is set up depending on the height of the buildings. When the air passes over an obstacle, a recirculation zone exists and the size of this recirculation depends on the size of the obstacle and its angle. Separation and reattachment are known as a recirculation zone. This may occur on smooth surfaces due to high angles or curvature of the boundary or can be caused by a discontinuity in the surface geometry. This recirculation zone will affect the concentrations of pollutants around this critical zone.

A commercial Computational Fluid Dynamics (CFD) software, Fluent, is used to simulate the flow and the dispersion of these pollutants near buildings, urban areas, hills etc. as it offers the possibility to investigate very complex geometries in high resolution. This study will examine the effect of topography on the dispersion of ethylene in the atmosphere from a point source located in different positions. To evaluate the accuracy of results, they are compared with experimental and numerical data.

1.1. Aims and Objectives

The aim of this study is to understand the flow and pollutant dispersion in the wake of a single hill, a single hill with obstacles and a flat terrain. Moreover, the effect of manmade topography on the dispersion of a chemical pollutant is also considered. The objectives are to evaluate which turbulence model is the best to use for this study and also to determine the areas of higher concentration.

This project considered the dispersion of ethylene in the presence of a combination of natural (e.g. a hill) and manmade topography (e.g. buildings) in order to determine the concentrations of pollutant in different regions of the domain and how the emissions are influenced by the obstacles. The case of a flow regime which generates a recirculation bubble in the wake of the hill will be taken into account. Ethylene has been chosen in order to be compliant with the experimental data of Khurshudyan et al. [17]. This work extends the research by Kim et al. [8] into a regime where the ratio of the heights of the buildings to the height of the hill is smaller.

Chapter 2

2. Literature Review

2.1. Flow around hilly terrain

The flow of wind in cases with a hilly terrain is a very complex problem but by using a fundamental approach to this problem, simple configurations and a standard type of flow must be conducted first followed by more complex situations. A number of authors have studied the above problem, by doing experimental and numerical simulations.

Griffiths et al. [9] have done a comparison between wind tunnel measurements and numerical simulations with Fluent software by using the k-ε standard turbulent model. They simulate hills of varying aspect ratios in order to analyse the flow around the hills. Depending on the shape of the hill, the flow separation downwind of the hill differs and the steeper the hill the longer the recirculation bubble.

Ferreira et al. [10] have done a comparison between numerical and experimental results to describe the flow around hills with different shapes, by using the k-ε model, which showed that the extension of the recirculation region is strongly dependent on the hill shape. In addition Pearse et al. [11], found out that surface roughness has a significant effect on the flow quantities and causes changes up to 20% in the mean velocity close to the ground. Furthermore, Gayev and Savory [12] have observed that trees can slow down winds through drag, trap contaminants below leaf level, etc. Tree trunks may actually increase turbulence intensity near the ground.

Meroney et al. [13], illustrate how over complex terrain local wind speeds may vary over 100% in a distance of a few hundred metres as a result of flow separation terrain shadowing or flow enhancement. Furthermore, to produce equivalent wind speeds near ground level requires accurate reproduction of surface roughness, shape and vegetation.

The measurements of the wind speeds predicted by Carpenter et al. [14] are higher values over the single shallow hill. For the two sinusoidal hill shapes the largest measured wind speed is measured on the crest of the single steep hill. When the hill configuration varies, the mean wind speeds decreases compared to the single

hill configuration and also decreases downwind of the first hill in the series. The gust speeds at the crests of the hills show little variation between different configurations and between adjacent hills, except that the highest gust speeds occur on the second hill for the multiple steep hill test. Steps in the upwind profile of a hill produce large changes in the wind characteristics at the crest of the hill. The height of the step, the distance of the step from the crest and the slope of the hill at the location of the step are all important factors that influence the resulting flow at the crest of the hill.

The flow around three conical hills with various slopes was examined by Pearse [15], who illustrates that as the flow approaches the upwind foot of the conical hills the velocity is reduced, and as the flow moves towards the hill crest the maximum velocity occurs at the crest of the hills. The greatest increase at the crest of all three hills, in the mean velocity occurs for the steepest conical hill.

Castro and Snyder [16] have investigated cases with different hills and sources placed at various heights and distances from the hill. The numerical models used have led to the examination of different parameters that affect the size of the recirculation region and the concentrations data. The results have shown that the roughness of the surface can modify the recirculation region and their study suggests taking into account the roughness of the hill. In this study, amplification factors, which are the ratios of maximum ground-level concentrations in the presence of the hills to those in the absence of the hills, and the stack heights are also used to examine the effect of the position of sources on the concentration data, in order to explain the role of the hill on the diffusion and transport phenomenon. The aspect ratio of the hill (defined as the ratio of width/height) and the position of the sources, with respect to the reattachment point were found to affect the amplification factors. Their investigation concludes that amplification factors increase when the source height is close to the reattachment point.

Khurshudyan et al. [17] have done a wind tunnel experiment for studying air flows and dispersion of pollutants in hilly terrain with various slopes. Three hills were used, having small, medium and steep slopes. The ethylene was emitted through a porous sphere. They measured the mean velocity upwind, at the summit, and downwind of each of the hills, and similarly for the pollutant distribution. These results were compared with theoretical models, for treating flow and dispersion over two dimensional hills. The models with the small and medium slopes have a good agreement with the theoretical models but not the model with the steepest slope.

This model does not have a good agreement with the theoretical model due to the steep hill, because of its existence, a high turbulence is present, with a reduced velocity downwind of the hill.

A simulation of hills of two dimensions with different slopes has been studied by Castro and Apsley [18]. They used the k-ε turbulence model in order to compute the flow over the hill and to make a comparison with the experimental data of Khurshudyan et al. [17]. These data are obtained for different hills with various slopes and a source at different positions near the hill. In terms of velocities of the flow, the differences between experimental and computed values are mostly observed at the downwind base of the hill. However, at the upwind base of the hill all computed data are very close to the experimental data of the models and almost similar velocities are found for different hill heights.

Arya, et al. [19] have experimented with various hill shapes and they found that the recirculation zone changes depending on the shape of the hill. Beyond about five hill heights, the hill induced perturbation in mean velocity. Regarding the pollutant emissions, which are in various positions, the effect they will produce will depend on the shape of the hills. If the point source is at the central line of the hill, and if the hill does not have any recirculation, then the emissions will not be affected by the hill but if the hill is steep then the concentrations at ground level will be reduced. If the emissions are located downwind of the hill, the ground level concentrations will be very high and this position of the source will be the worst situation to consider when a pollutant emission release is diffused in any urban area. In this case, the high level of pollutant concentration can be dangerous for the entire environment. But if the emission source is located at the upwind of the hill, the ground concentration level will significantly decrease and the environment will be less affected.

Lai and Chan [20] have done a study over a two dimensional hill with a small slope which demonstrated that when there is an upwind source located at the upper layer, the concentrations decrease with distance along the upwind side of the hill and tend to be a constant near the hill top. Results from this study show that the concentration distribution depends on the wind, and the position of the source.

Young-Rae et al. [21] developed a particular code using the Reynolds-average Navier-Stokes equations in order to simulate the flow field. The results of this research have demonstrated that the shape and aspect ratio of the hill is related to the

pollutant concentration on the ground. The height of the source and its location are also key factors to the value of these concentrations.

Egan [22], states that the main effects of topography on the dispersion of pollution result from changes to the mean flow, turbulence and the possibility of advection into recirculation regions. In addition some wind tunnel studies have been accomplished by Arya and Gadiyaram [23], in which they have examined hills with various slopes, and discovered that the steeper the hill, the larger recirculation it has. A result of this study is that the hill slope and the aspect ratio are very important parameters for flow dispersion.

Finardi et al. [24] have investigated the effect of complex terrain on the wind field. They have described and then analysed the wind characteristics and their influence on pollutant dispersion in order to simplify computation and modelisation of wind conditions. The report of the study proposed a terrain classification based on the morphology of the terrains and their influence on the wind field. For each class of terrain, the wind characteristics are separately considered and categorised regarding their influence on pollutant dispersion.

Mello and Yanagihara [25] studied the mean concentration and flow over a two-dimensional triangular hill with a point pollutant source. They have performed simulations and calculations with a k-ε turbulence model and the results have shown that the numerical results of mean concentrations are always lower than experimental results in this case. The reason is because the experimental data are given by C/Cmax which are relative measurements of concentrations and are very influenced by the maximal concentration Cmax and where this value is collected. If this value is measured very close to the source then, as suggested by Apsley and Castro [26] and Bocon and Maliska [27], the numerical approach is known to measure unsatisfactory results near the source. Except for this point, generally in this study for the mean and the variance of the concentration and also for the velocity profiles, the numerical results are in good agreement with the experimental results.

The dispersion of pollutant has been investigated by Chatzipanagiotidis and Olivari [28] with experiments in a wind tunnel with a hill and a stack located at the left side of a hill in various heights. Measurements have been done in order to determine the pollutant concentration of the plume. The results have shown that the pollutant dispersion is influenced by the upstream flow conditions in terms of local and maximum concentrations, particularly when the thickness of the boundary layer

varies significantly. In addition, the height of the stack plays a big role for the dispersion of the plume. For example, when the stack is half the hill's height, then the concentration of the pollutant at the area near the hill will be higher than if the stack height was higher than the hill.

2.2. Flow around single buildings, street canyons and hill with buildings

A configuration of a street with buildings in a row along both sides described as street canyon by Nicholson [29] and the dimensions of it are described as 'ratio', which is the height of the building (H) to width of the street (W). Dispersion in street canyons depends on the rate at which the streets exchange air vertically, with the top level of the atmosphere and laterally, with connecting streets.

There are various configurations of street canyons and depending on each configuration, the flow will change. If the spacing between the buildings is too large and the height is low, then their flow fields do not interact. Oke [30] reported that if the spacing is closer between buildings, the wakes are disturbed and due to the smaller spacing between the buildings, an isolated roughness flow regime exists (Figure 2-1a). If the height of the buildings are such that they disturb the strength and cavity eddies the flow regime changes and is known as wake interference flow (Figure 2-1b). If the buildings are so close that the bulk of the flow does not enter inside the street canyon, then within the canyon single vortices exist and this is known as skimming flow regime (Figure 2-1c).

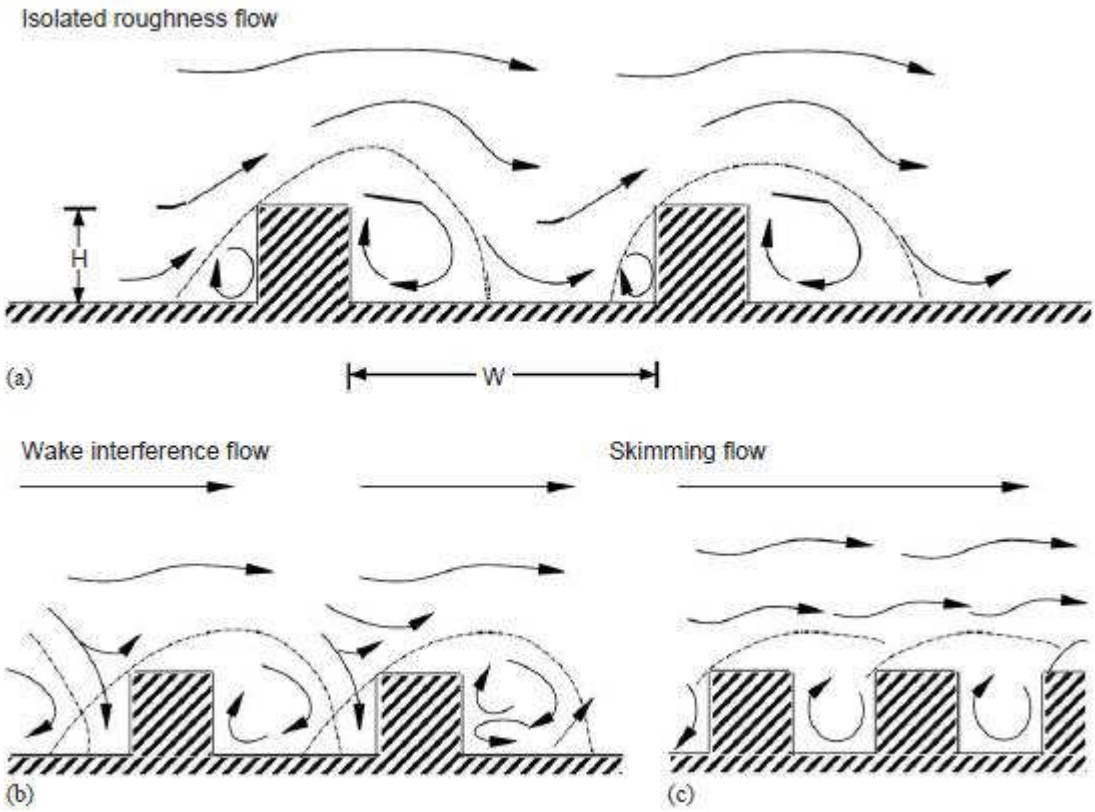

Figure 2-1 Perpendicular flow regimes in urban canyons for different aspect ratios [30].

Many experimental and numerical studies are dealing with fluid flow around buildings. Stathopoulos and Storms [31] have investigated wind flow between two rectangular buildings for particular configurations and the most crucial velocity conditions is for the buildings of various heights. The experimental study has demonstrated that turbulence conditions exist more when the wind is perpendicular to the centre line of the passage. In addition, as the width of the passage increases, the velocity in this area is lower and the turbulence intensities in the passage are higher.

Chang and Meroney [32] have conducted research to understand the concentrations and flow distributions around buildings in an urban area. From their simulations they have observed that the upwind wall areas have higher concentrations than the downwind wall areas. This happens due to the two circulations flows inside the street canyon. One circulation flow is clockwise and carries the pollutant to the upwind wall of the street canyon, resulting in higher concentrations on the upwind wall. The other is a lower circulation flow which is counter clockwise and carries some emission to the downwind wall of the street canyon, so the ground corner of the

downwind wall also has high concentrations. In the case of an isolated building because there is no wake zone to transport pollutant to upwind, the higher concentrations are located at downwind wall.

Meroney et al. [33] studied the flow and the dispersion of gases emitted by sources using various k-ε turbulent models using Fluent software. Numerical results were compared with experimental results, which showed that for the same cases different results were predicted for the reversal flow. Also an adapted grid can help by having details of the recirculation zone.

Zhang et al. [34] have compared a k-ε model based on the eddy viscosity concept with the wind-tunnel experiments of Castro and Robins [35] for different approach flow conditions. A numerical model was used to examine the influence of shear and flow turbulences around a building. It was found that the upwind shear promotes the development of the upwind vortex at the front of the building, while it reduces the size and strength of the much larger cavity in the lee of the building. The result is that by increasing the wind and the turbulence intensity, the recirculation zone weakens.

Chang et al. [36] focused on the formation of vortices inside street canyons and they have observed that in deep canyons two vortices may be generated. The upper vortex is driven by the ambient wind flow and the lower one is driven by the circulation of the upper vortex. The particularity of these vortices is that their directions are opposites.

Experimental investigations have been achieved by Higson et al. [37], on flow and dispersion around an isolated building, where the tracer gas was upwind of the building and with the help of a detector system the concentrations were measured. The purpose of this work is to compare the concentration distributions measured at various locations in field and wind tunnel data. The difference in the concentration distributions may be partially due to the difference instrument response time. The field detector is faster and has greater resolution for the high frequency concentration fluctuations. However, by filtering the field data into that used in the wind tunnel, some parameters are affected.

In the same field, Wedding et al. [38] observed that a tall and isolated structure are helpful in mixing pollutants in the downwind side of the building but they have also noticed that in the leeward side of the building a large concentration level of pollutants may be measured.

Mavroidis et al. [39] have done a comparison on dispersion between wind tunnel and field which shows that the plume is more dispersed in the field due to the atmospheric wind. In order to understand the complexity of the dispersion in wind tunnel, Snyder [40] has conducted physical simulation studies in wind tunnels and these studies show a high potential to understand the wide range of complex dispersion phenomena. The main advantage using wind tunnels is the control of variables at will and economy in terms of time and money.

Delaunay [41] has illustrated the flow when, on the top of a building, a chimney exists. He shows that the second order scheme for turbulence modelling seems necessary to reproduce recirculating flows on the roof and near the obstacles.

Characteristics of flow and dispersion have been initially examined in a wind tunnel by Robins and Castro [42], who have investigated the importance of the velocity and the turbulence fields generated by the flow dispersion around buildings. Because flow dispersion in the surrounding area of buildings is very complicated, data about concentrations need to be completed with some knowledge of their velocity and also of turbulence fields in order to examine the diffusion characteristics of the flow. Also, concentration fields have been measured by Robins and Castro [43] from the release of pollutants in the vicinity of large obstacles and the study has shown that the maximum concentration and its position are function of the pollutant dispersion velocities and the height of the source.

Pollution dispersion modelling in an urban area is examined by Galani et al. [44] who observe that the presence of the vortices inside a street canyon increases the concentration of pollutant within the canyon. Moreover the wind speed, direction and height of the buildings all play a big role in the dispersion of the plume. The wind velocity increases with height and causes a decrease in the pollutant concentration levels.

Hoydysh and Griffiths [45] have investigated the effect of buildings and generally the influence of crosswind area on the concentration levels in an urban area. They concluded that tall and isolated obstacles are responsible for the decrease of the pollutant concentration and these structures can be used in order to reduce it.

Ahmad et al. [46] reported in their study that the flow and the dispersion of pollutants inside a street canyon depend on its geometry (building shape, aspect ratio, and length-to-depth ratios). The formation of vortices inside the canyons is also due to the geometry of the buildings. In deep canyons, the vortices are not affected by the

external wind flow on the top of the canyon. Ahmad et al. have observed better ventilation for short canyons because corner vortices are created but this effect is limited when the street length is increased. When the ventilation is not effective enough, the trapping of pollutants in the corners of the building is observed and is due to the formation of intermittent vortices in these areas. The trapping of pollutants inside the street canyon will depend on the location of the canyons. A stable rotating vortex is generated inside the canyons in urban areas, this stable vortex has the effect to suppress the ventilation of the street and results in the trapping of the pollutants. The trapping of pollutants can be reduced by forming intersections to the wind flow in order to create better ventilation in those corners where the pollutants are blocked by the corner vortices.

Ogwawa et al. [47] investigated a cavity wake length behind a cube, which is influenced by the wind direction and the turbulence intensity. As the turbulence intensity increased, the cavity wake length decreased. The turbulent intensity was varied by changing both the upwind roughness and the wind direction.

For CFD simulations Blocken et al. [48] advise assessing the effects of horizontal inhomogeneity by simulating the cases in an empty domain, before conducting simulations with the building models present. They distinguished three different regimes of flow conditions in passages between the buildings: Resistance, Interaction and Isolated flow. The experimental study by Stathopoulos et al. [49] and numerical study by Blocken et al. [48] indicate that these regimes appear to occur within a well-defined almost universal range of the ratio of the passage width divided by the building influence scale.

Chu et al. [50] have determined the dispersion of emissions around buildings and provide information about the height of the emissions and the pollutant. A result from their study is that near the inlet the wind velocities are large at the edges of the buildings, decrease in wake areas and are reduced inside canyons. These unbalanced wind velocities will influence the pollutant dispersion. When the wind speed is around 1.5m/s and the source is located at 2 metres height, the buildings are blocking the dispersion of the pollutant but when the wind speed is increased to 5m/s, then the pollutant goes inside the canyon. On the other hand, when the source is located at 20 metres height no matter what the wind conditions, the pollutant is spread over a large area. Pollutant concentrations are usually blocked left in the canyons and this is due to the existence of vortices, where the pollutant cannot be easily dispersed. The different

heights of buildings will affect the distribution of pollutants and moreover when the wind becomes stronger, the pollution around the buildings will be lower.

Tampieri et al. [51] have conducted a review of characteristics of the mean flow and turbulences in the lee of a two dimensional obstacle. With a view to understanding why in this area of hills and other obstacles the mean velocity is usually reduced, they studied a case with a source placed in this specific zone and then analysed the dispersion and concentrations. In order to understand the behaviour of the dispersion, wind tunnel data were analysed and compared with model predictions. The observations and measurements of this study have shown that turbulent flow is characterised by the existence of coherent structures that affect significantly the dispersion in the short-term. The analyses of the concentrations data demonstrate that these structures also have a large influence on the long-term average concentrations. This work invites us to take greater account of the turbulent flow behaviour and especially the presence of large vortices in the lee of obstacles as these have a big influence on dispersion.

Kim and Baik [52] have used a configuration model for a simple building of two dimensions and have examined the effects of inflow turbulence intensity and pollutant dispersion on the urban street canyon. They have also pointed out that the more the turbulent intensity at the inflow increases, the more the turbulent kinetic energy rises. Consequently, the diffusivity and horizontal velocity at the height of the roof grow and the vortex strengthens. Turbulent intensity at the inflow plays an important role in the concentration in the street canyon. If the inflow turbulent intensity increases, the level of concentration at any altitude will grow at the beginning but at the end this concentration will be negligible. The low concentration results from the transport of pollutant which is fast due to the high inflow turbulence intensity and velocity.

Vardoulakis et al. [53] have made a review of the scientific understanding of dispersion, air pollution phenomena in urban area. They have reported for example that high pollutant concentrations have been always measured on the leeward side of urban canyons under perpendicular wind conditions. The review has also pointed out that for the most part of the researches different combinations of monitoring and modelling techniques for understanding pollutant dispersion in urban street have been adopted. Mathematical and physical models are used to optimise pollutant dispersion monitoring.

A study of flow and pollutant dispersion in urban street canyons has been done by Baik and Kim [54] where they have used a two dimensional k-ε turbulent model. From their research it has been shown that when the height or width of buildings is increasing, the vortices are also increasing. The motion at the bottom, downwind of the canyon, is stronger than in the upwind canyon and the same happens with the turbulent kinetic energy because of stronger wind shears near the downwind of the canyon. Results show that vortex circulation plays a major role in the way that emissions are distributed in street canyons.

Sagrado et al. [55] have conducted studies to determine the behaviour of wind flow and pollutant dispersion in urban canyons using wind tunnel measurements and Fluent software. The results of this research state that pollutant concentrations are affected by the height of the downwind canyon wall. Increases in this height generate a decrease in the pollutant concentrations in this area.

Vardoulakis et al. [56] studied the dispersion of pollutants within urban street canyons where generally the highest level of pollutants are concentrated because of the presence of buildings which can not permit natural ventilation. Within the canyon, wind vortices may be created and high concentration levels have been observed on the leeward side of regular canyons.

Experiments by Mavroidis and Griffiths [3] examined the characteristics of flow and dispersion near obstacles. Mean velocity measurements indicated that the effect of the shape of an individual obstacle embedded in the array on mean flow and dispersion is significant in the near wake region of this obstacle and is then reduced until it becomes negligible approximately two rows downwind.

The pollutant dispersion of emissions in various two dimensional street canyons has been examined by Nazridoust and Ahmadi [57]. Their research indicates that the pollution depends on the building height and the wind speed. They have concluded that a large recirculation region with up to four vortices might be observed in the street canyons depending on wind speed, building height and street width. They have used a two dimensional k-ε turbulent model in order to simulate a symmetrical and asymmetrical street canyon and have also done a comparison with wind tunnel experiments. It has been found, for the symmetrical canyon, that the pollutant concentration is higher at the upwind wall of the canyon than the downwind.

For the asymmetrical canyon, because of the different heights of the buildings, more vortices have been observed at the top of the canyon. Also for pollutant dispersion,

the height and arrangement of buildings play an important role. The emissions which are transported by the air are trapped inside the canyons, but as the velocity increases, the concentration of pollutant reduces inside the canyons.

Ayata [58] has investigated the problem of building height and roof effect in Turkey. Buildings do not generally have a simple shape (rectangular) and many studies can be found in the literature analysing the importance and effect of building and roof shapes. Wind pressure distributions on a roof depend upon roof geometry. In his study, Ayata used Fluent and the k-ε turbulence model to simulate the airflow. The results of this investigation have demonstrated that the roofs have the effect of increasing the level of protection of houses and buildings and also of decreasing the air velocity magnitude at the front of the house. But the phenomenon of turbulence observed that turbulence is larger in front of houses with roofs. This investigation has also shown that pyramid shaped roofs decrease turbulence and that this is even lower than in the case of rectangular shaped roofs.

Davidson et al. [59] have presented the results of the dispersion of pollutant from a source point through a large group of obstacles. Detailed field results for the flow and dispersion have permitted the conclusion that there are two mechanisms which affect the behaviour of a plume as it passes through a large group of obstacles. The first is the divergence and the convergence of streamlines through the obstacles, and the second is the changes in turbulence. In this study the first mechanism increases the overall height of the plume by approximately 50% and changes to the structure of the turbulences have little effect on the concentrations and spread of the plume.

Kim et al. [8] have used a two dimensional k-ε turbulence model in order to study the flow and pollutant dispersion when a single hill and two buildings exist in a street canyon. The curve of the hill is very important to the size of the recirculation. As the angle of the curve is enlarged, the recirculation becomes larger. When there are both single hill and buildings, the flow is changing due to the height and angle of the buildings and hill. Furthermore, with a source located upwind of a hill, as the hill slope increases, the maximum concentration decreases in the downwind region of the hill.

Cao and Tamura [60] have made an experimental study, with a hill and a number of small cubes on the hill surface, in order to present the roughness. Vertical profiles of the turbulence statistics over the rough hill were compared with the profiles over a flat surface covered by cubes with the same pattern. Furthermore, for a smooth hill with the same shape, measurements were taken to identify the surface roughness effects. The results show that the roughness affects the flow and especially the flow over the hill. The speed-up ratio above the crest of a rough hill is larger than that of a smooth hill. The separation bubble of a rough hill extends further downstream, resulting in a larger reattachment length than a smooth hill.

Arya and Gadiyaram [61] found that the recirculation zone which appears downwind of one obstacle, depends on the obstacle's slope. The ground level concentrations when the emissions are on the top of the hill are less than if they are located on a flat terrain and the measurements are taken from the same position. The hill slope and the aspect ratio are the most important parameters in determining the flow and dispersion characteristics.

A study has been conducted on the use of CFD in predicting a pedestrian wind environment Franke et al. [62]. They call for a validation study with an experimental wind tunnel or water tunnel, before any simulations take place, in order to secure the help of complete data sets. The built area should be less than 3% of the whole domain and the outflow should be situated far from the built area in order to have a developed flow. In general, the numerical diffusion that appears in the results of first order schemes is significantly reduced by the use of a second order scheme and the accuracy is increased. Also in the examined area, the grid should be based on the convergence study to check if the values in this area are still the same. So for this study, a second order scheme is used, the built area is taken to be less than 3% of the whole domain and the resolution proposed by the convergence study is used.

Chapter 3

3. Classification and description of the fluid flow

In this section the main classes that distinguish fluid flows are summarised.

3.1. Laminar and Turbulent flows

The presence of turbulence offers another way to classify flows. Laminar flow is characterised by lower velocities and fluid particles that move in smooth lines. Thus, the flow can be said to move in layers.

On the other hand, in turbulent flows the paths of individual flow particles are not straight but are disordered, permitting fluid mixing to take place. Turbulent flow involves secondary components with arbitrarily, random and irregular behaviour, superimposed on the principal motion of fluid. A single particle follows an unpredictable path in three dimensions. It should be noted that most fluid flows in engineering applications are turbulent.

The distinction between laminar and turbulent flow may be made by means of the Reynolds number. This number is defined as $\mathrm{Re} = \frac{\rho U l}{\mu}$ where ρ is the fluid density, μ the dynamic viscosity of the fluid, U a characteristic velocity, and l is a characteristic length. In general engineering conditions, laminar flow occurs for flow through pipes, at a Reynolds number $\frac{\rho U d}{\mu}$ below 2000, where d is denoted as the pipe diameter. Given the same flow conditions, turbulent flow occurs for Re > 4000 and transitional flows occurs for 2000<Re<4000 [63].

3.2. Steady and Unsteady flows

The time-dependence of a flow classifies it as steady or unsteady. Since steady flow is usually easier to implement, a suitable frame of reference may be chosen so that the flow appears to be steady. Turbulent flows are usually considered to be steady by using time-averaged values of the velocity field.

3.3. Viscous and Inviscid flow

Viscous flow is dominated by the effects of viscosity. For instance where the velocity gradients are large, the effect of viscosity is significant on the characteristics of the flow, and in the same manner when these velocity gradients are small, the behaviour of the flow is, of course, less affected by viscosity. The boundary layer is defined as the region with dominating viscous effects in high Reynolds numbers.

3.4. The Navier-Stokes equations for incompressible flow

Computational fluid dynamics solves the Navier-Stokes equations, which are non-linear differential equations that describe the flow of a fluid whose stress depends linearly on velocity and pressure. The unsimplified equations do not have a general closed-form solution, so they have to be solved by numerical means. The equations can be simplified in a number of ways so that they are easier to solve. The Reynolds Averaged Navier-Stokes equations are based on the time averaging of the flow quantities which are really important for solving engineering problems.

In the present study, the flow is at a much lower speed ($M<<0.3$), so that compressibility effects can be neglected and incompressible flow assumed.

CFD solves the fundamental governing equations of fluid dynamics, namely continuity, momentum and energy. Note that, in this study, the flow is considered to be incompressible, so that ρ is constant, which simplifies the Navier-Stokes system and the energy equation is not specified.

3.5. Continuity Equation

The continuity equation is based on the law of conservation of mass, which says that the mass of a closed system, irrespective to what is happening inside the system, will remain constant:

$\frac{\partial \rho}{\partial t} + \nabla(\rho V) = 0$, where ρ is constant because the flow is incompressible so:

$$\frac{\partial u}{\partial x} + \frac{\partial v}{\partial y} = 0$$

Where: u and v are the components of the velocity vector in the x and y direction respectively.

3.6. Momentum Conservation Equations

The principle of conservation of momentum is in fact an application of Newton's second law of motion for an element of fluid. According to that, the net force acting on the fluid particle under consideration must equal its mass times its acceleration.
The equations are given by:

3.6.1. Conservation of u momentum

$$\frac{\partial u}{\partial t} + u\frac{\partial u}{\partial x} + v\frac{\partial u}{\partial y} = -\frac{1}{\rho}\frac{\partial p}{\partial x} + \upsilon\left(\frac{\partial^2 u}{\partial x^2} + \frac{\partial^2 u}{\partial y^2}\right)$$

3.6.2. Conservation of v momentum

$$\frac{\partial v}{\partial t} + u\frac{\partial v}{\partial x} + v\frac{\partial v}{\partial y} = -\frac{1}{\rho}\frac{\partial p}{\partial y} + \upsilon\left(\frac{\partial^2 v}{\partial x^2} + \frac{\partial^2 v}{\partial y^2}\right)$$

Where: p=pressure, υ=viscosity, u =x-velocity and v =y-velocity

3.7. Conservation equation for scalars (for concentrations).

3.7.1. The conservation equation for a tracer

The balance for matter or temperature is given below:

$$\frac{\partial c}{\partial t} + \sum_j u_j \frac{\partial c}{\partial xj} = Dc \sum_j \frac{\partial^2 c}{\partial x_j^{\,2}} + S_c$$

Introduction of the fluctuations to the concentration C = c + c' in the conservation equation and temporal averaging gives the following expression (same procedure as with the current fluctuations above):

$$\frac{\partial c}{\partial t} + \sum_j u_j \frac{\partial c}{\partial xj} = Dc \sum_j \frac{\partial^2 c}{\partial x_j^{\,2}} + S_c - \sum_j \frac{\partial}{\partial x_j} \overline{(u_j' c')}$$

(I) (II) (III) (IV) (V)

I: local temporal change of concentration (storage)

II: divergence of advective transport (due to a concentration gradient)

III: diffusion; Dc: molecular diffusion coefficient for tracer c

IV: source minus sink term (volume term), which accounts for all other (chemical, biological etc.) processes which depend on the scalar c (sources, sinks, production, reactions...).

V: Divergence of the turbulent tracer flux.

Analogously to the Reynolds stress, fluctuations have to be considered for the turbulent transport of tracers. Accordingly, a term describing the turbulent tracer flux is introduced $\overline{uj'c'}$. The molecular diffusion (III) can usually be neglected in comparison to the turbulent flux (V). When the fluctuations are due to eddies of small size, the turbulent flux $\overline{uj'c'}$ can be described with the so-called eddy formulation.

The philosophy of the eddy formulation is that the temporal average $\overline{uj'c'}$ which represents the sum of the many small fluxes eventually add up to a flux which can be considered a diffusion type flux. It depends on (i) the local gradient $\frac{\partial c}{\partial xj}$

and (ii) the turbulent diffusion coefficient Kj. The form is identical to molecular diffusion, however the Kj is usually several orders of magnitude larger than the molecular diffusivity. Kj is a function of the turbulent flow and not of the H2O properties or water constituents.

3.8. Reynolds –averaged Navier-Stokes

Reynolds-averaged Navier–Stokes (RANS) equations are the oldest approach to turbulence modelling. The central equations for fluid dynamics are the Navier-Stokes equations, which are non-linear differential equations that describe the flow of a fluid whose stress depends linearly on velocity and pressure. The unsimplified equations do not have a general closed-form solution, so they are only used in computational fluid dynamics. The equations can be simplified in a number of ways. All of the simplifications make the equations easier to solve. An ensemble version of the governing equations is solved, which introduces new apparent stresses known as Reynolds stresses. The idea behind the equations is Reynolds decomposition, whereby an instantaneous quantity is decomposed into its time-averaged and fluctuating quantities. The RANS equations are primarily used to describe turbulent flows. These equations can be used with approximations based on knowledge of the properties of flow turbulence to give approximate time-averaged solutions to the Navier–Stokes equations. For incompressible flow the equation is the following:

$$\rho \overline{u}_j \frac{\partial \overline{u}_i}{\partial x_j} = \rho \overline{f}_i + \frac{\partial}{\partial x_j}\left[-\overline{p}\delta_{ij} + \mu\left(\frac{\partial \overline{u}_i}{\partial x_j} + \frac{\partial \overline{u}_j}{\partial x_i} \right) - \rho \overline{u_i' u_j'} \right]$$

The left hand side of this equation represents the change in mean momentum of fluid element owing to the unsteadiness in the mean flow and the convection by the mean flow. This change is balanced by the mean body force, the isotropic stress owing to the mean pressure field, the viscous stresses, and apparent stress $\left(-\rho \overline{u_i' u_j'}\right)$ owing to the fluctuating velocity field, generally referred to as the Reynolds stress. This nonlinear Reynolds stress term requires additional modelling to close the RANS equation for solving, and has led to the creation of many different turbulence models.

3.8.1 Boussinesq hypothesis

This method involves using an algebraic equation for the Reynolds stresses which include determining the turbulent viscosity, and depending on the level of complexity of the model, solving transport equations for determining the turbulent kinetic energy and dissipation. The models available in this approach are often referred to by the number of transport equations associated with the method. For example, the Mixing Length model is a "Zero Equation" model because no transport equations are solved. The k-ε model is a "Two Equation" model because two transport equations (one for k and one for ε) are solved. The following chapter analyse these two types of models.

Chapter 4

4. Numerical Methods

4.1. Turbulence models

"Turbulence is an irregular motion which in general makes its appearance in fluids, gaseous or liquid, when the flow passes solid surfaces or even when neighboring streams of the same fluid flow passes over one another." Wilcox [65], this definition was originally proposed by Taylor and von Karman in 1937. Turbulence modelling is very important for CFD by creating mathematical models which approximate and describe the physical behaviour of turbulent flows. The ideal model should not be very complicated but should capture the fundamental nature of the physics involved in the flow. Generally Navier-Stokes equations are sufficient to describe the fluid flow but if more details are required, a large amount of complex mathematics might be needed.

Much software exists today, in order to solve the equations of flow, and provides various RANS models for turbulence. Fluent is a commonly used CFD software package and also the software is used for the simulations in this study. There are various mathematical models used in flow modelling to understand turbulence. The turbulent models presented in this work are the Spalart-Allmaras, and all the family of k-ε models.

4.2. One equation model

Spalart-Allmaras model

The most common simple, one equation model is the Spalart-Allmaras model. It is designed in particular for aerospace applications concerning wall-bounded flows and can be used when the mesh at the wall is coarse or fine. This model solves an additional transport equation for a modified turbulent kinematic viscosity. Turbulent viscosity is determined from [66]:

$$\mu_t = \rho \tilde{\nu} \left[\frac{\left(\tilde{\nu}/\nu\right)^3}{\left(\tilde{\nu}/\nu\right)^3 + {c_{\nu 1}}^3} \right]$$

And $\tilde{\nu}$ is determined from the modified viscosity transport equation:

$$\rho \frac{D\tilde{\nu}}{Dt} = \underbrace{\rho c_{b1} \tilde{S} \tilde{\nu}}_{Generation} + \frac{1}{\sigma_{\tilde{\nu}}} \left[\underbrace{\frac{\partial}{\partial x_j} \left\{ \left(\mu + \rho \tilde{\nu} \right) \frac{\partial \tilde{\nu}}{\partial x_j} \right\} + \rho c_{b2} \left(\frac{\partial \tilde{\nu}}{\partial x_j} \right)^2}_{Diffusion} \right] - \underbrace{\rho c_{w1} f_w \frac{\tilde{\nu}}{d^2}}_{Destruction}$$

Where in these equations: μ_τ =turbulent viscosity, ν=molecular kinematic viscosity. For this model the constants are given by default [67]:

$C_{\nu 1}$=7.1, C_{b1}=0.1355, C_{b2}=0.622, $\sigma_{\tilde{\nu}} = \frac{2}{3}$

$C_{w1} = \frac{C_{b1}}{\kappa^2} + \frac{(1+C_{b2})}{\sigma_{\tilde{\nu}}}$, κ=0.4187.

4.3. Two-equation k-ε model:

Within these methods, two transport equations are solved for two additional transport variables, one for the turbulent kinetic energy (k) and the other for the dissipation rate (ε). These variables are used to identify the characteristics of the flow.

The k-ε model has three variations:

- ✓ The k-ε Standard Model
- ✓ The k-ε RNG Model
- ✓ The k-ε Realizable Model

The k-ε Standard Model

This is the most widely used model in industry and is valid only for fully turbulent flows. The Standard k-ε model is a semi empirical model based on model transport equations for the turbulence kinetic energy (k), and its dissipation rate (ε), from the observation of physical phenomena and applicability to a wide range of flows with satisfactory accuracy. It has also reasonable accuracy for a wide range of turbulent flows such as industrial flows and heat transfer.

The turbulence kinetic energy k, is given by the following equation [66]:

$$\underbrace{\rho U_i \frac{\partial k}{\partial x_i}}_{Convection} = \underbrace{\mu_t \left(\frac{\partial U_j}{\partial x_i} + \frac{\partial U_i}{\partial x_j} \right) \frac{\partial U_j}{\partial x_i}}_{Generation} + \underbrace{\frac{\partial}{\partial x_i} \left\{ \left(\mu_t / \sigma_k \right) \frac{\partial k}{\partial x_i} \right\}}_{Diffusion} - \underbrace{\rho \varepsilon}_{Destruction}$$

And the dissipation rate is given by:

$$\underbrace{\rho U_i \frac{\partial \varepsilon}{\partial x_i}}_{Convection} = \underbrace{C_{1\varepsilon} \left(\frac{\varepsilon}{k} \right) \mu_t \left(\frac{\partial U_j}{\partial x_i} + \frac{\partial U_i}{\partial x_j} \right) \frac{\partial U_j}{\partial x_i}}_{Generation} + \underbrace{\frac{\partial}{\partial x_i} \left\{ \left(\mu_t / \sigma_\varepsilon \right) \frac{\partial \varepsilon}{\partial x_i} \right\}}_{Diffusion} - \underbrace{C_{2\varepsilon} \rho \left(\frac{\varepsilon^2}{k} \right)}_{Destruction}$$

Where in these equations: U=velocity, μ_{eff} =turbulent viscosity, k=turbulence kinetic energy, ε=turbulence dissipation rate. For this model the constants are given by default [67]:

$C_{1\varepsilon} = 1.44$, $C_{2\varepsilon} = 1.92$, $\sigma_k = 1.0$, $\sigma_\varepsilon = 1.3$.

The RNG k-ε Model

The RNG k-ε mainly comes from the k-ε standard model, using a mathematical technique called the Renormalisation Group (RNG) method. This model is similar in form to the standard k-ε equations but includes an analytical formula for a turbulent Prandtl number, a differential formula for effective viscosity, the effect of swirl on turbulence and an additional term in the ε equation that improves the analysis of rapidly strained flows. The use of this model is usually for transitional flows, wall heat, mass transfer and high streamline curvature.

The turbulence kinetic energy k, is given by the following equation [66]:

$$\underbrace{\rho U_i \frac{\partial k}{\partial x_i}}_{Convection} = \underbrace{\mu_t S^2}_{Generation} + \underbrace{\frac{\partial}{\partial x_i}\left(a_k \mu_{eff} \frac{\partial k}{\partial x_i}\right)}_{Diffusion} - \underbrace{\rho\varepsilon}_{Dissipation}$$

where $S \equiv \sqrt{2S_{ij}S_{ij}}$, $S_{ij} \equiv \frac{1}{2}\left(\frac{\partial U_j}{\partial x_i} + \frac{\partial U_i}{\partial x_j}\right)$

And

$$\underbrace{\rho U_i \frac{\partial \varepsilon}{\partial x_i}}_{Convection} = \underbrace{C_{1\varepsilon}\left(\frac{\varepsilon}{k}\right)\mu_t S^2}_{Generation} + \underbrace{\frac{\partial}{\partial x_i}\left(a_k \mu_{eff} \frac{\partial \varepsilon}{\partial x_i}\right)}_{Diffusion} - \underbrace{C_{2\varepsilon}\rho\left(\frac{\varepsilon^2}{k}\right)}_{Destruction} - \underbrace{R}_{\substack{Additional\ term\ related\ to\ mean\ strain\ \&\ turbulence\ quantities}}$$

Where in these equations:

U=velocity, μ_t =turbulent viscosity, μ_{eff} =effective viscosity, α_k ,is the inverse effective Prandtl number for k and ε. k=turbulence kinetic energy, ε=turbulence dissipation rate. For this model the constants are given by default [67]: $C_{1\varepsilon} = 1.42$, $C_{2\varepsilon} = 1.68$.

The Realizable k-ε Model

The expression 'Realizable' comes from the model's properties, which satisfy certain mathematical constraints on the normal stresses, consistent with the physics of turbulent flows. This model shares the same turbulent kinetic energy equation with the standard k-ε model. It is very practical for planar and round jets and is good for cases when they have rotation and recirculation.

It is different from the standard k-ε model in its alternative formulation for turbulent viscosity [66]:

$$\mu_t \equiv \rho C_\mu \frac{k^2}{\varepsilon} \quad \text{where} \quad C_\mu = \frac{1}{A_o + A_s \frac{U^* k}{\varepsilon}}$$

The transport equations for dissipation rate, ε is given by:

$$\rho\frac{D\varepsilon}{Dt}=\frac{\partial}{\partial x_j}\underbrace{\left[\left(\mu+\frac{\mu_t}{\sigma_\varepsilon}\right)\frac{\partial\varepsilon}{\partial x_j}\right]}_{Diffusion}+\underbrace{\rho c_1 S\varepsilon}_{Generation}-\underbrace{\rho c_2\frac{\varepsilon^2}{k+\sqrt{\nu\varepsilon}}}_{Destruction}+\underbrace{c_{1\varepsilon}\frac{\varepsilon}{k}c_{3\varepsilon}G_b}_{Buoyancy}$$

Where in these equations:

U=velocity, μ_t =turbulent viscosity, A_o, A_s, U^* are functions of velocity gradients, σ_ε is the inverse effective Prandtl number for k and ε, k=turbulence kinetic energy, ε=turbulence dissipation rate, G_b is the generation of turbulence kinetic energy due to buoyancy. For this model the constants are given by default: $C_{1\varepsilon}=1.42$, $C_{2\varepsilon}=1.68$, $\sigma_\varepsilon=0.2$ [67].

Chapter 5

5. Modelling

The simulations of this study are validated with the experimental and numerical data of Khurshudyan et al. [17] and Castro and Apsley [18] respectively.

In the present work, a simulation is performed of the flow over a two-dimensional symmetrical hill in order to observe the recirculation behind the hill. The commercial software that was used for the inspection of this study is Fluent 6.3.26 and for the generation of the grid, Gambit 2.4 was applied.

The dimensions of the computational domain, as can be seen in Figure 5-1 are: -40H upwind of the summit of the hill and +40H downwind, in total W_d=9360mm, with domain height H_d=13.7H, where H is the height of the hill. The hill midpoint is at zero.The dimensions of the hill are as follows: height=H=117mm, length=W=702mm, with a roughness length Z_o=0.16mm.

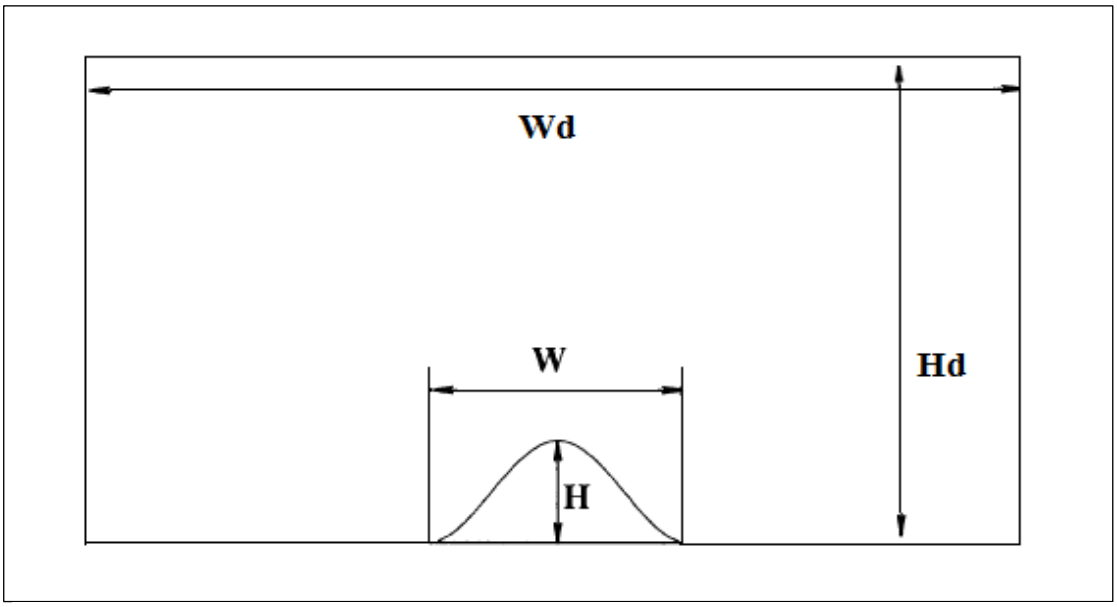

Figure 5-1 Size of the whole domain.

The Reynolds number is Re=3x10^4 in this experiment which is based on the height of the hill and the inlet velocity which is 4m/s. The friction velocity is $\frac{U_*}{U_\infty} = 0.047$ where U_∞ is the free stream velocity.

The Inlet Velocity is specified at inflow as:

$$U = \begin{cases} \frac{U_*}{\kappa} \ln\left(y / z_0\right), 0 < y \le h \\ \text{and } U_{\infty,} y > h \end{cases}$$

Where h is the depth of the boundary layer, chosen so as to make the mean velocity and turbulent kinetic energy profiles continuous. In order to calculate h, the following values are used: U=4m/s, U_*=0.188m/s, κ =0.41, z_o=0.00016m, giving h=0.9838m.

In general the finer the grid is the more accurate results are. When the size of the grid is very fine then accuracy is increasing. So in order to capture all the details near the wall the grid should be very fine. However the equation predicts at y=0 (ground) that $U = \infty$. This is of course impossible because the velocity on the surface should be zero. Only in the area around the hill the velocity varies and this is due to the recirculation zone that exists. The log formula for the boundary layer is applied for heights greater than the height of the roughness.

The Turbulent kinetic energy and Dissipation rate are specified as:

$$k = \begin{cases} C_\mu^{-1/2} U_*(1 - y/h)^2, y < 0.9h \\ \text{and } k_\infty, y > 0.9h \end{cases}$$

$$\varepsilon = \frac{C_\mu^{3/4} k^{3/2}}{\kappa z}$$

The hill is described by the functions:

$$x = \frac{1}{2}\xi\left[1 + \frac{a^2}{\xi^2 + m^2(a^2 - \xi)}\right]$$

$$z = \frac{1}{2} m\sqrt{a^2 - \xi^2}\left[1 + \frac{a^2}{\xi^2 + m^2(a^2 - \xi)}\right]$$

Where:

$m = n + \sqrt{n^2 + 1}$, $|\xi| \le a$ and n=H/a is the average slope which is for this case 26°.

And where a=half-width of hill, ξ=arbitrary parameter, x is directed along the approach flow direction (origin at hill center) and z is directed vertically upwards. Since the surface is two-dimensional, the equation does not include the y parameter.

5.1. Boundary Conditions and Computational Techniques

Flow calculations were undertaken using Fluent software and a vertical stretching two-dimensional structured grid is used. For the inlet boundary conditions, at the main inlet the streamwise velocity has been set up with a User Define Function (UDF) which is a function to define the discrete phase boundary condition type and it can be found in the Appendix. Moreover, for the velocity inlet boundary conditions, the specification method used for this study is the turbulence kinetic energy (k) and the turbulent dissipation rate (ε) which are defined with a UDF for the k-ε Standard and k-ε RNG models.

The C_μ constant is no longer the same for the Realizable k-ε model because it is computed from a more complicated equation. In this study the data were not enough to specify this number. That is why k-ε Realizable model has different boundary conditions from the other two k-ε models. For the Spalart-Allmaras model the k and ε can not be specified. For this reason the turbulent intensity and the hydraulic diameter are specified for the last two models. Turbulent intensity is defined as the ratio of the root-mean-square of the velocity fluctuations, u' to the mean flow velocity u_{avg} and the hydraulic diameter is given by $D_h = \frac{4A}{P_w}$ where A is the cross-sectional area, P_w is in the 2D case equal to 2.

The discretisation of the various terms was second order upwind scheme (more details at the Appendix B), except Pressure which was Presto (Pressure Staggering Option). The Presto scheme is well suited for flows with curved domains and for the steep pressure gradients involved in swirling flows. The Mach number is very low, Mach

number=4/330=0.012, (where U=4m/s) and is less than 0.3M consequently, for this reason the flow is supposed to be incompressible. So a 2D incompressible solver is chosen and this flow is a steady flow. The air properties used in this study are the following:

Temperature ($^{\circ}C$)	Density (kg/m^3)	Viscosity (kg/ms)
$27^{\circ}C$	1.225	1.789

Table 5-1 Air Properties.

The boundary conditions represent the influence of the surroundings that have been cut off by the computational domain. At the inflow boundary a velocity inlet is used, in order to specify the velocity of the domain. At the bottom, a wall boundary is used, because of the tunnel and also to bind fluid and solid regions. At the boundary behind the hill, where the fluid leaves the computational domain, an outflow boundary is used [62]. Outflow boundary conditions are used to model flow where the detail of the flow and pressure are not known prior to any solution of the flow problem. No conditions are defined at outflow boundaries. Outflow boundary condition is appropriate where the exit flow is close to a fully developed condition, as the outflow boundary condition assumes a zero normal gradient for all flow variables except pressure. The solver extrapolates the required information from interior. Furthermore, an overall mass balance correction is applied.

Also, at the top, a symmetry boundary is set down which enforces the parallel flow. Calculations of a boundary layer over ground for the single hill case wind tunnel for y^+=1 are:

$\mathrm{Re} = \frac{\rho U l}{\mu}$, where in this case Re= 3×10^4

The equation is given by: $y = \frac{y^+ \mu}{\rho U^*}$

Where:

y=the distance from the wall and the first cell

μ=air viscosity = $1.789\times10^{-5} kg/ms$

ρ=air density = 1.225 kg/m^3

U^*=friction velocity= 0.188 m/s

y^+=is a mesh-dependent dimensionless distance that quantifies to what degree the wall layer is resolved

$$y = \frac{y^+ \mu}{\rho U^*} = \frac{1.789 \times 10^{-5}}{1.225 \times 0.188}$$

So the distance from the wall and the first cell is considered to be 7.768×10^{-5} mm.

5.2. Grid

Gambit 2.4.6 was used for geometry and mesh generation. The grid geometry is relative to the single hill case and represented in Figure 5-2.

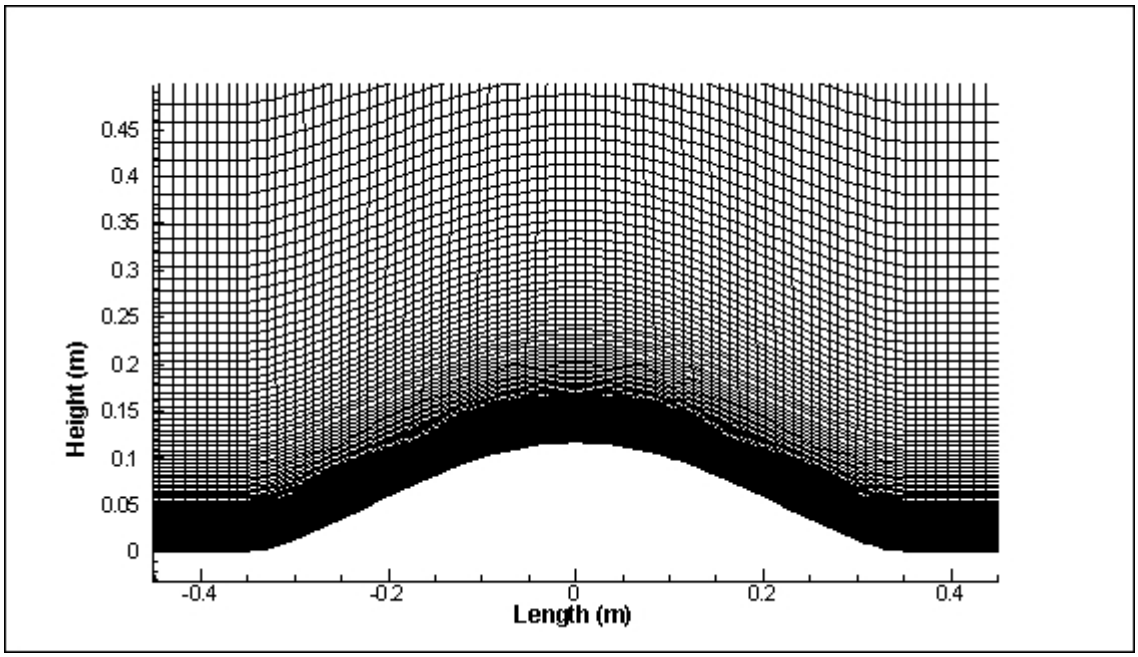

Figure 5-2 Mesh distribution around the

5.3. Grid convergence study

There is a choice of four turbulent models. Four models are being selected in order to assess their suitability: the Spalart-Allmaras model, and from the family of k-ε models, the Standard, the RNG and the Realizable. To get an indication of the grid resolution, the k-ε Standard model is initially used. For this case, the cells of the mesh are quadrilaterals so the grid is structured. The number of nodes for the mesh dependency study in the horizontal and vertical directions are the following: (60x40), (100x80), (200x160) and (300x300).

A grid convergence study has been done in order to check the dependency of the results compared to the mesh size. Figures 5-3, 5-4, 5-5 and 5-6 represent the size of the recirculation bubble downwind of the hill in various mesh sizes.

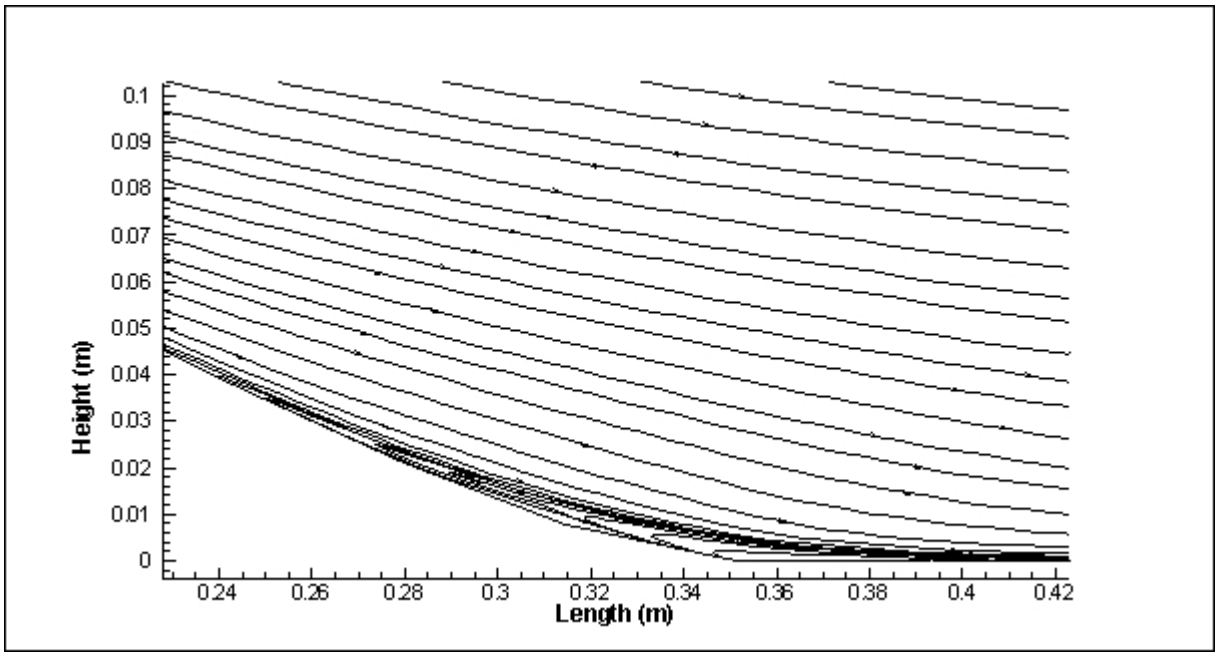

Figure 5-3 Plot of the velocity distribution within the flow field using streamline field for a grid with 2400 cells.

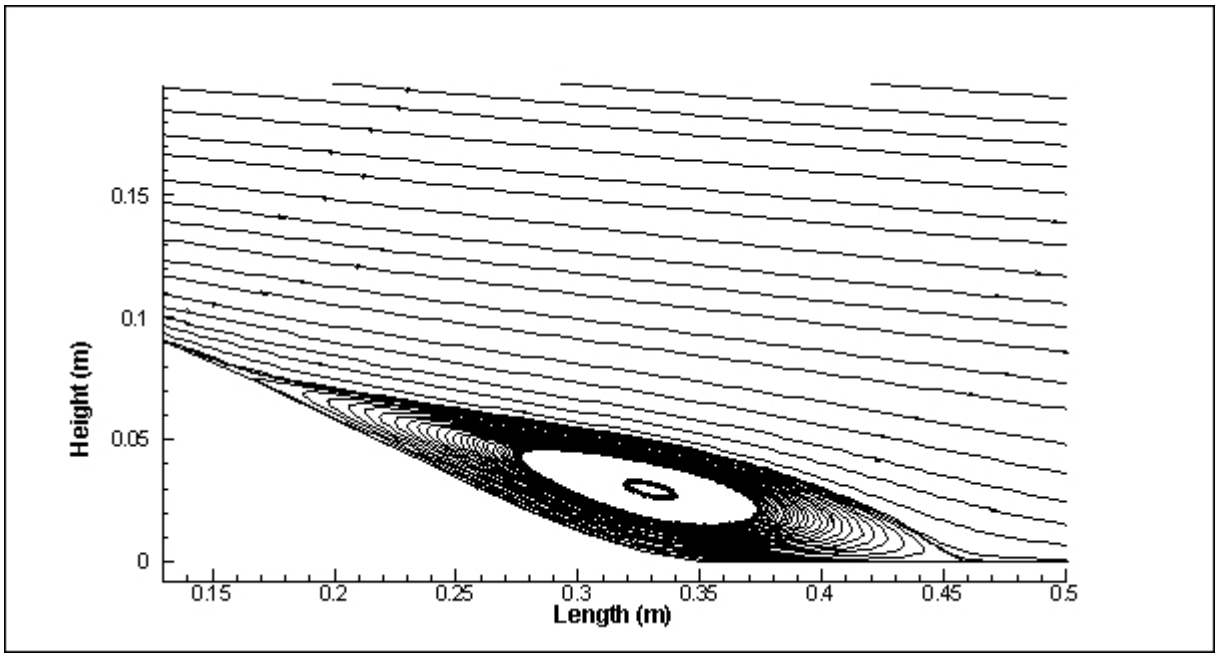

Figure 5-4 Plot of the velocity distribution within the flow field using streamline field for a grid with 8000 cells.

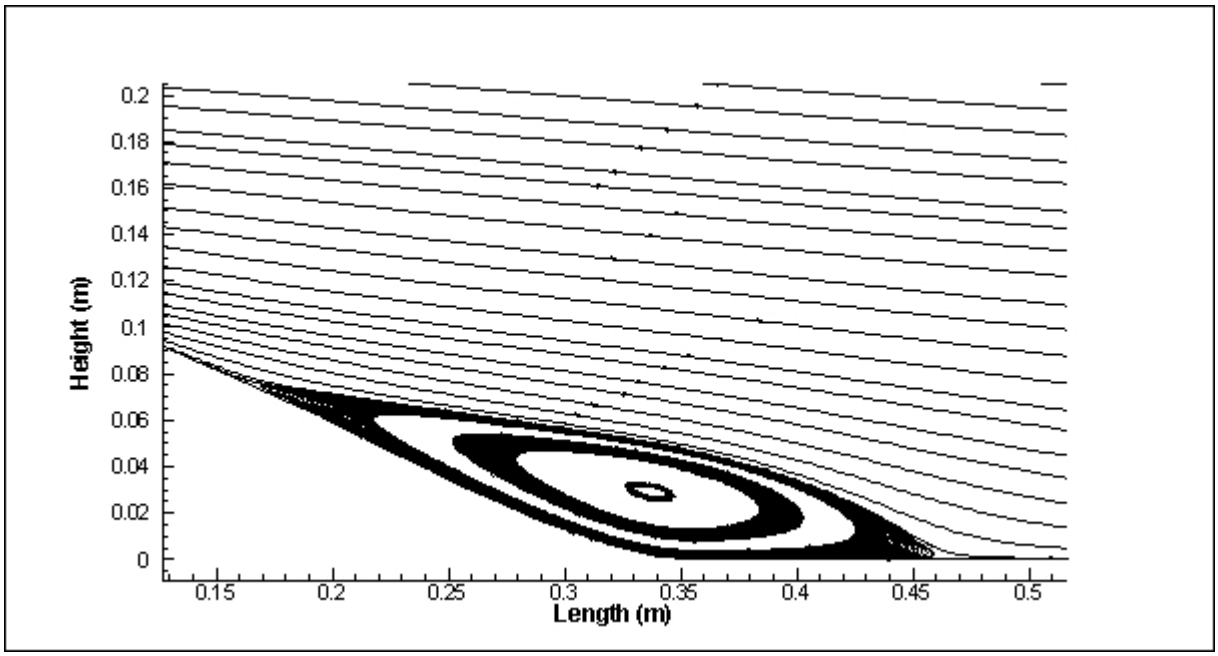

Figure 5-5 Plot of the velocity distribution within the flow field using streamline field for a grid with 32000 cells.

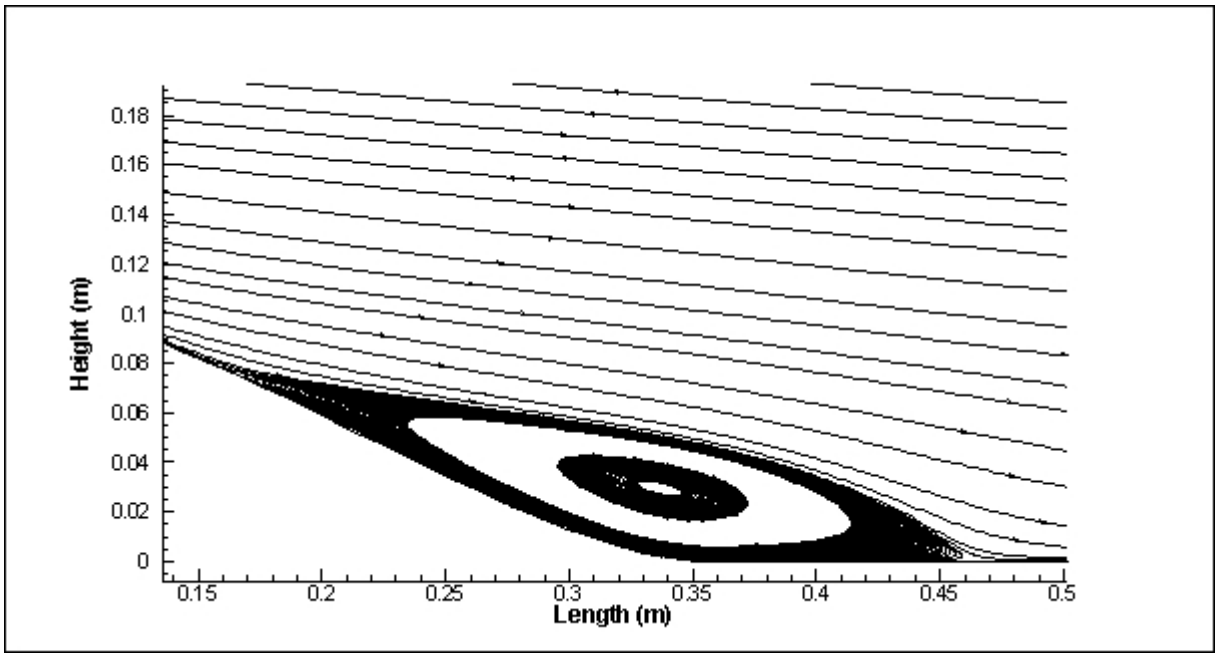

Figure 5-6 Plot of the velocity distribution within the flow field using streamline field for a grid with 90000 cells.

The coarse grid (Figure 5-3) has 2400 cells, and the recirculation is about 0.176m with a separation extent up to 0.239m and reattachment up to 0.415m. The medium grid (Figure 5-4) has 8000 cells, and the recirculation is about 0.310m with a separation extent up to 0.150m and reattachment up to 0.460m. The fine grid has 32000 cells (Figure 5-5) in which the recirculation zone is 0.315m and lays between 0.154m and 0.469m the same also applies to the grid of 90000 cells (Figure 5-6). Numerical results by Castro and Apsley [18] demonstrate that the reattachment downwind of the top of the hill is 0.479m which is significantly lower than the experimental, by Khurshudyan et al. [17], determined the reattachment at 0.760m.

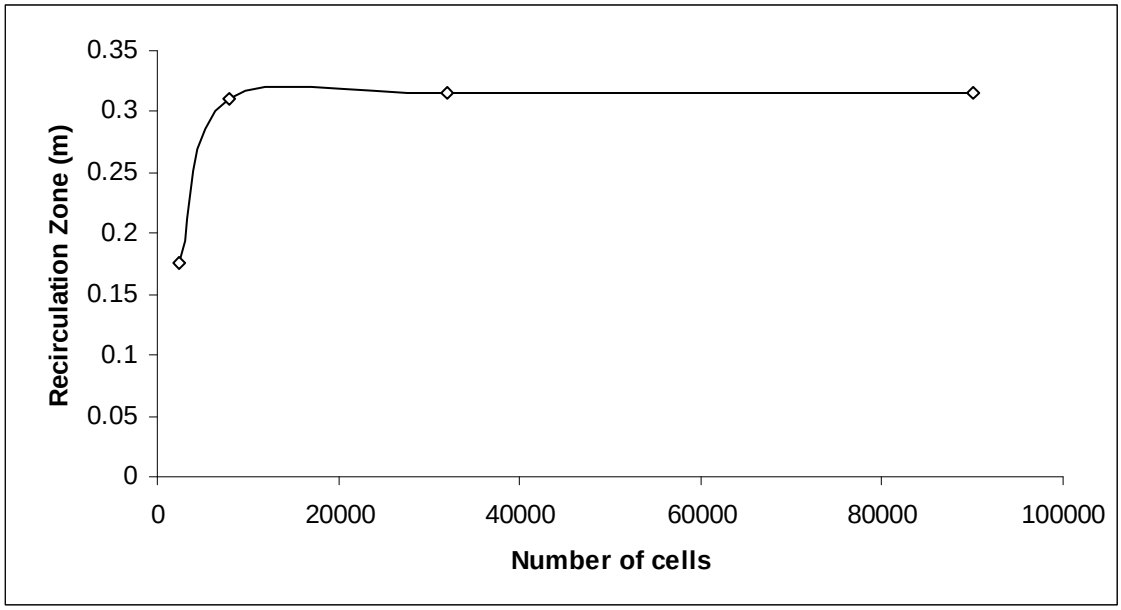

Figure 5-7 Length of the recirculation zone as a function of the number of computational cells.

Figure 5-7 shows how the recirculation zone changes depending on the grid. When the domain has a small number of points, it will not be as accurate as a domain with two or three times the number of nodes. Also, with more points it will take longer for the simulation to converge. As the number of nodes inside the domain increases, the length of the recirculation zone becomes constant. From this it can be concluded that the grid of 32000 cells is sufficient for the purpose of this project. The grid with 90000 cells has the same results as the grid of 32000 cells, but because the time for the simulation is doubled, the grid with 32000 cells is used and preferred for the simulations. The horizontal velocities on the top of the hill at x=0m and downwind of the hill at x=0.351m, have also been considered for the grid convergence study. The next figure shows the horizontal velocity on the top of the hill.

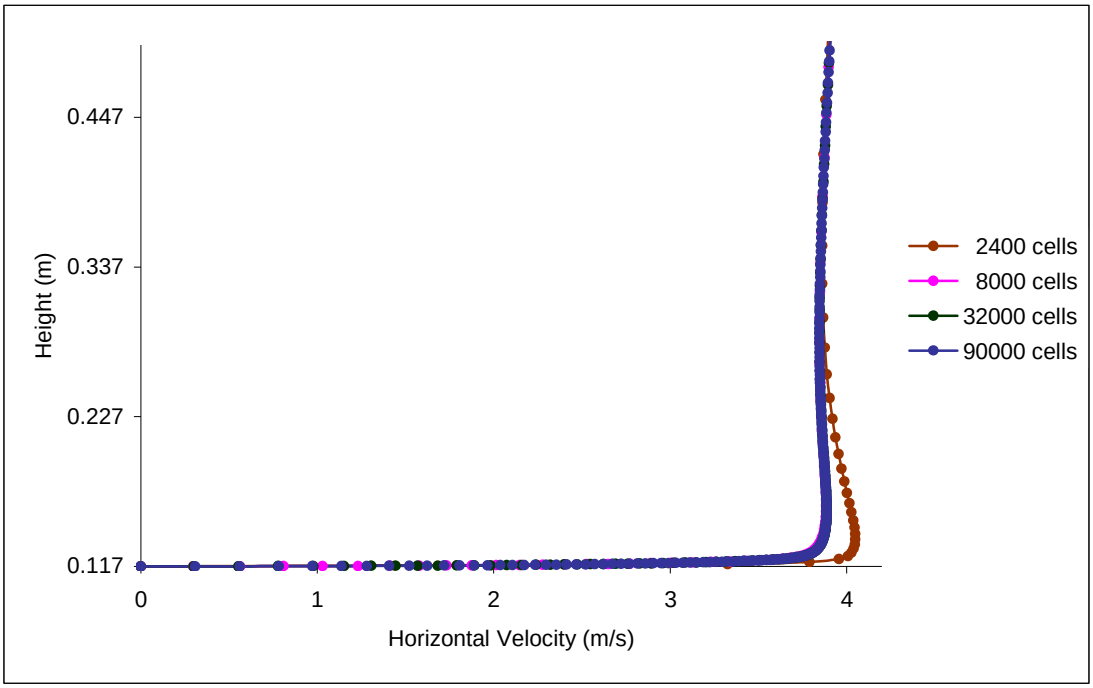

Figure 5-8 Horizontal velocity profiles for the hill at the summit.

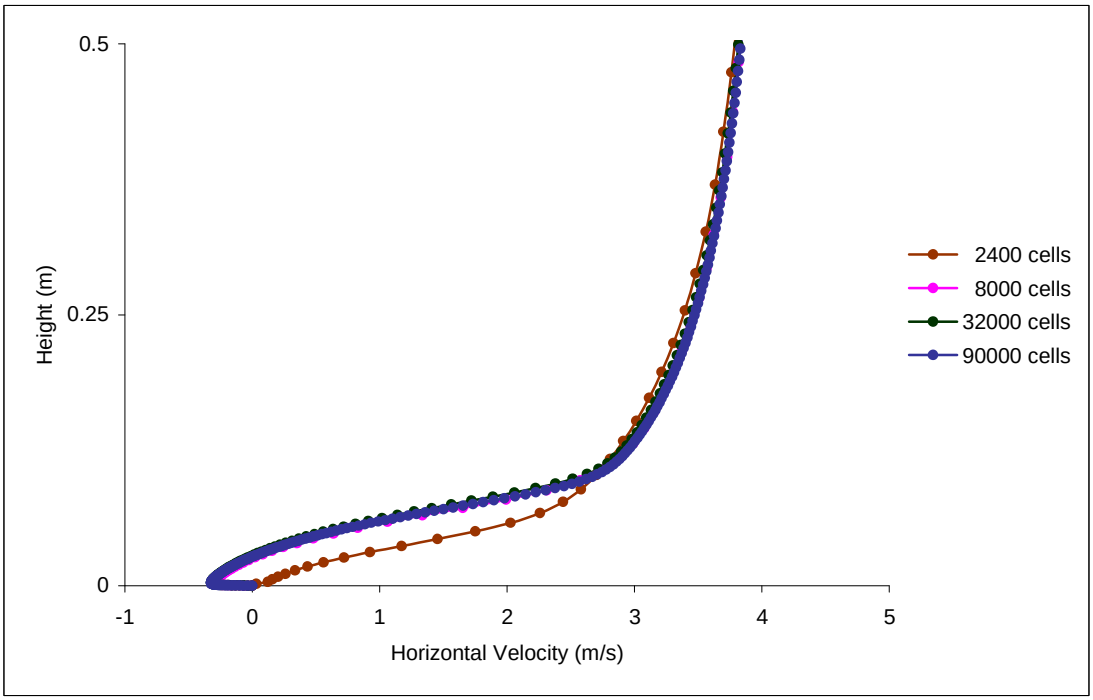

Figure 5-9 Horizontal velocity profiles for the hill at the downwind base.

Figure 5-8 shows the horizontal profiles of the velocity and, as can be observed, the mesh with 2400cells is not fine enough to be as accurate as the other meshes. On the other hand, the results of the other three meshes are very close to each other, with the mesh of 32000 cells and 90000 cells giving the same results. This can also be observed in Figure 5-9 which shows the horizontal velocity downwind of the hill.

From Figure 5-9 it can be observed that the line from the mesh with 2400 cells does not have the same behaviour as the other lines, especially at the beginning where the difference is large. The other three meshes follow the same trend, the mesh with 32000 cells gives the same results as the mesh with 90000 cells, so the mesh with 32000 cells is used for the simulations of this study in order to reduce the simulation time.

Chapter 6

6. Validation of the model

The objectives of this section are to select a suitable turbulence model which will be the model whose outcomes are close to the experimental results, in order to assess the pollutant transport performance of the model. The comparison will be done as well with the numerical results of Castro and Apsley [18]. The flow calculations were undertaken using their own code based on the finite volume for a non-orthogonal curvilinear coordinate system. The discretised momentum equations include buoyancy and rotation terms so that the code can be used for more general atmospheric flow simulations. The resulting terms representing departure from first order upwind scheme were included in the source terms. In this study the validation has been done with the mesh of 32000 cells. A number of runs have been done with: Spalart-Allmaras (1 equation model), k-ε Standard model (2 equation model), k-ε RNG model (2 equation model), k-ε Realizable model (2 equation model).

6.1. The mean flow and turbulent fields for the single hill case

Figures 6-1, 6-2 and 6-3 represent the vertical profiles of the x-component of velocity normalised by the free stream velocity $U_\infty = U_0$. The data are collected at the upwind base located at (-351,0), for the summit at (0,117) and downwind base of the hill at (351,0) respectively.

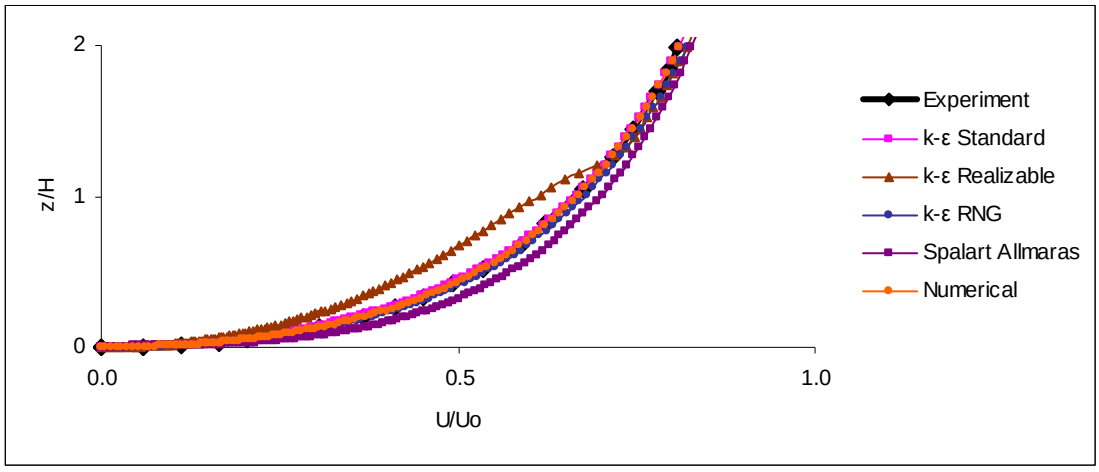

Figure 6-1 Velocity profiles for the hill at the upwind base.

The upwind base for the Spalart-Allmaras model, on the one hand follows the same trend but on the other hand it is on average 2.6% away from the experimental line. The line of the k-ε Realizable model, does not match with the experimental line and it has 1.7% difference from it. Closer to the experimental line is the k-ε Standard and RNG model with the first one on average 0.5% different from the experiment and the second model on average 0.3% different. Furthermore, at the upwind base the numerical data by Castro and Apsley [18] are almost synchronized with the experimental data.

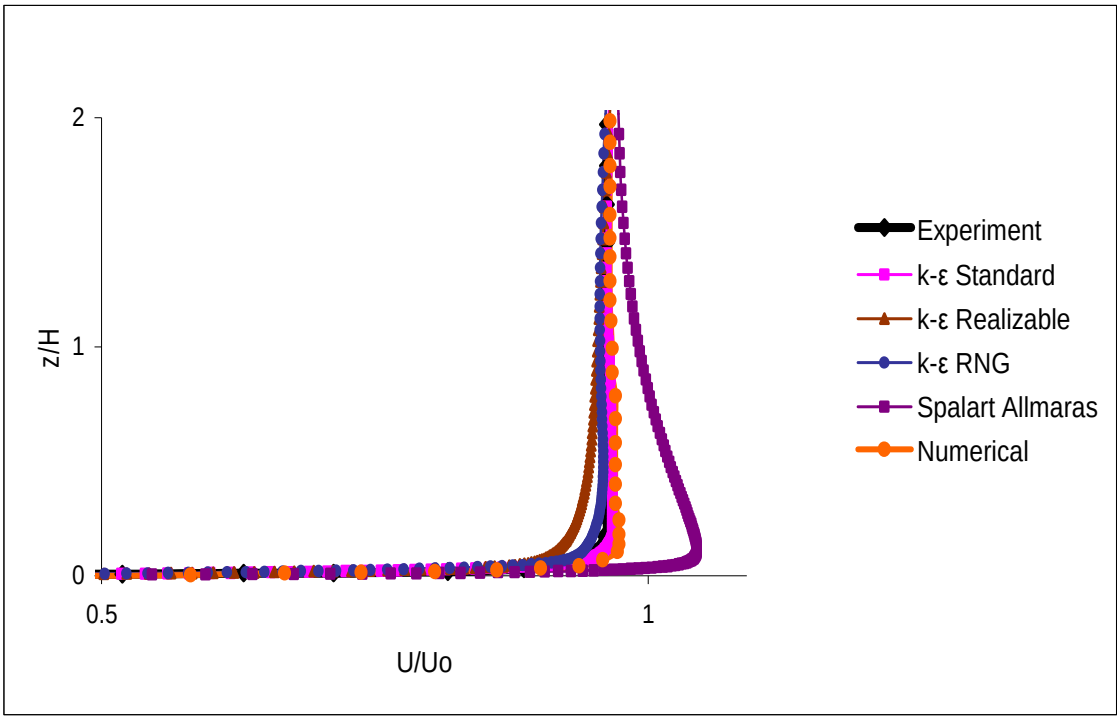

Figure 6-2 Velocity profiles for the hill at the summit.

Concerning the summit, the results for the Spalart-Allmaras and k-ε Realizable model do not match with the experimental line, as Spalart-Allmaras has on average an 8.2% difference and Realizable 3.1% from the experiment. The k-ε Standard and RNG models are very close to the experimental line with on average 0.4% difference for the k-ε Standard and 1.2% difference for the RNG model. Over the summit both numerical and experiment data indicates a nearly uniform velocity over several hill heights. For the downwind case, it can be seen from the beginning that the Spalart-Allmaras has 18.1% difference and k-ε Realizable has 21.7% difference from the

experimental line. The k-ε RNG model is closer to the experiment but not as close as the k-ε Standard model, which is the only model from those four that matches with the experiment. The differences between the k-ε RNG with experimental data is 14.2% and the k-ε Standard model with experimental data is 5.4%. Furthermore, the numerical results for upwind, summit and downwind of the hill from Castro and Apsley [18] are almost synchronized with the experimental data, with some discrepancies at the downwind base.

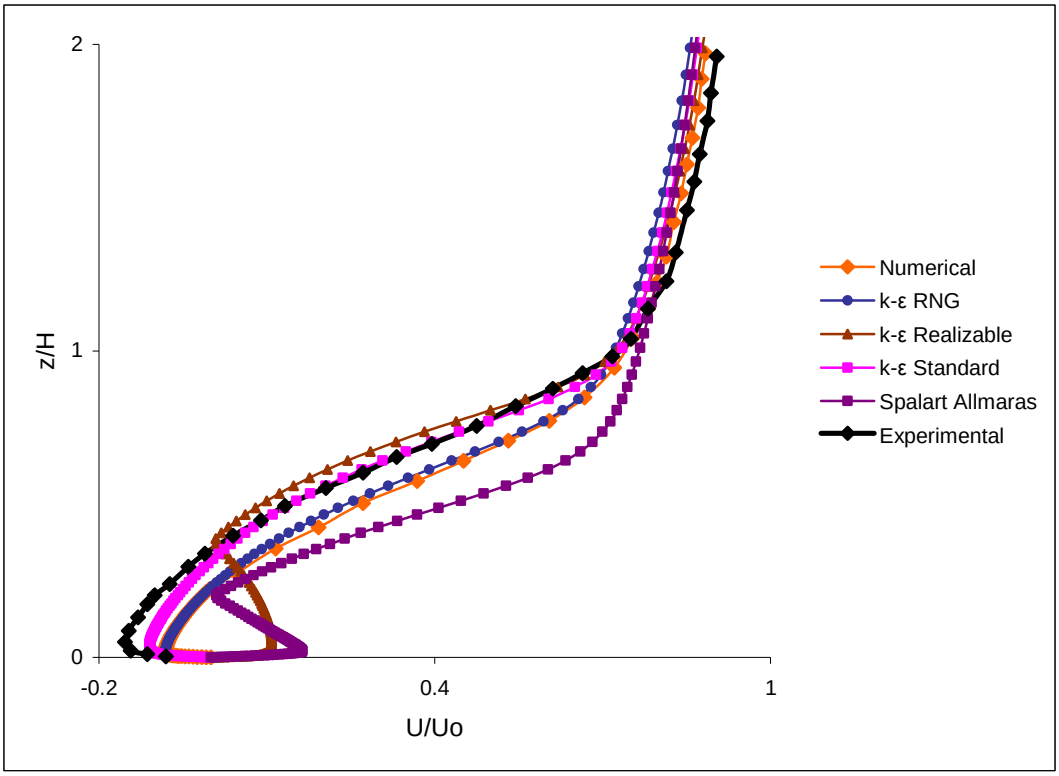

Figure 6-3 Velocity profiles for the hill at the downwind base.

In order to observe the flow differences between these four turbulence models, streamlines and contours of horizontal velocity have been examined downwind of the hill and are represented in the following figures.

k-ε Standard model:

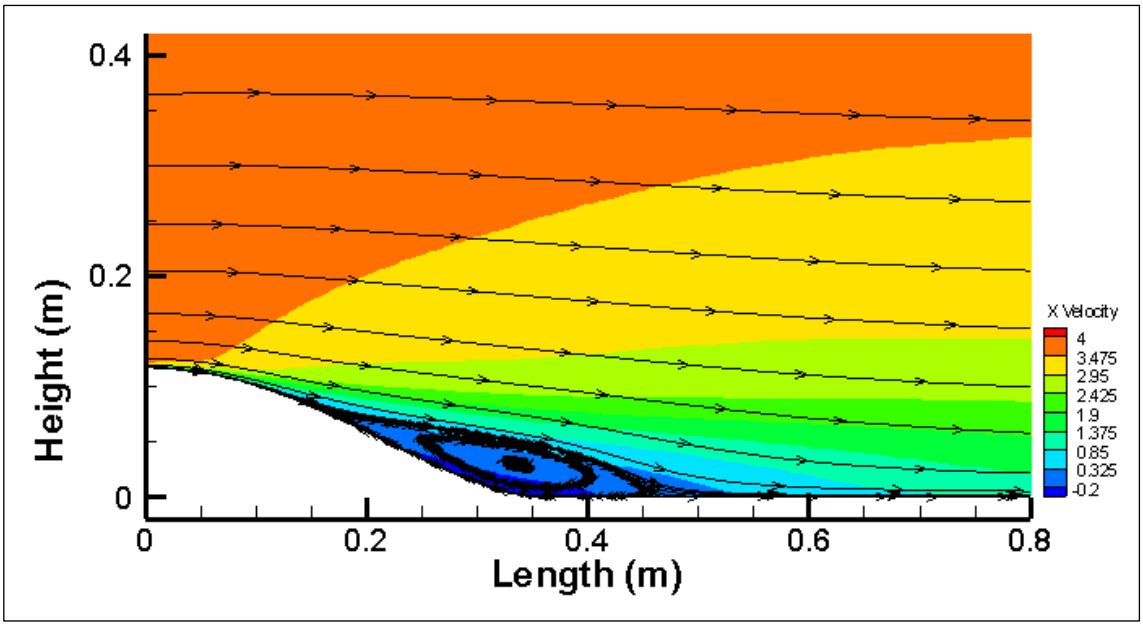

Figure 6-4 Streamlines and contours of horizontal velocity for k-ε Standard model.

k-ε RNG model:

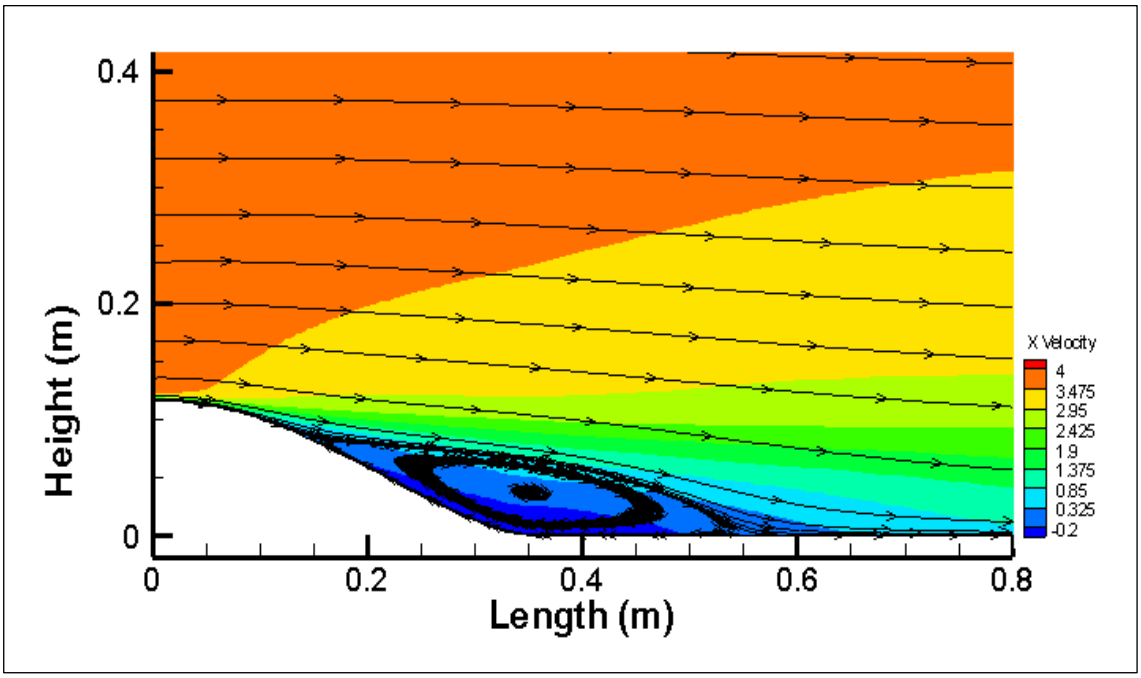

Figure 6-5 Streamlines and contours of horizontal velocity for k-ε RNG model.

k-ε Realizable model:

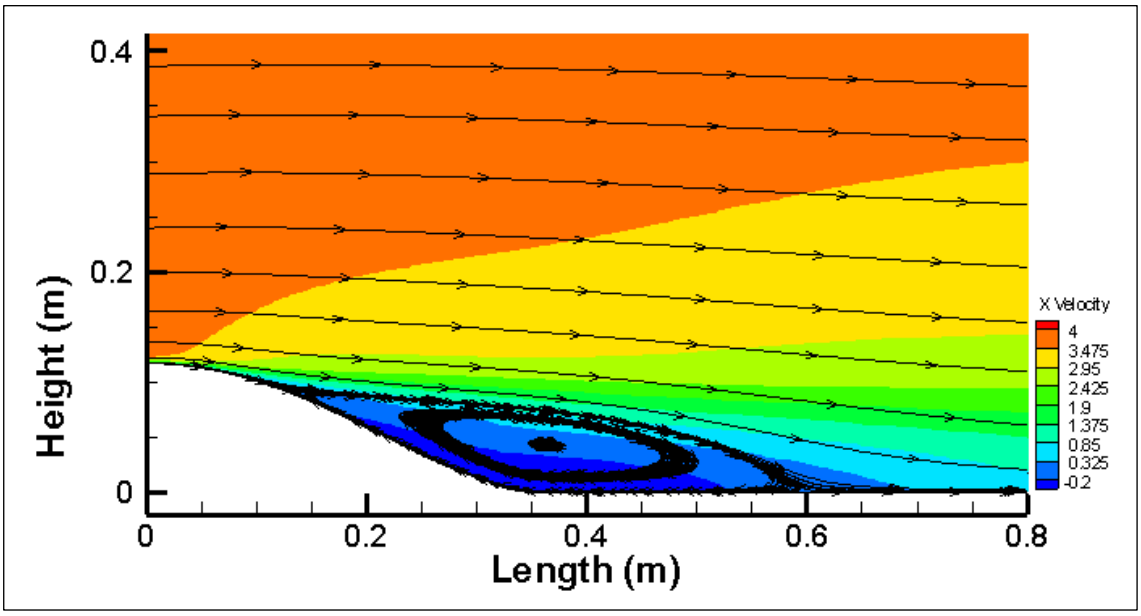

Figure 6-6 Streamlines and contours of horizontal velocity for k-ε Realizable model.

Spalart-Allmaras model:

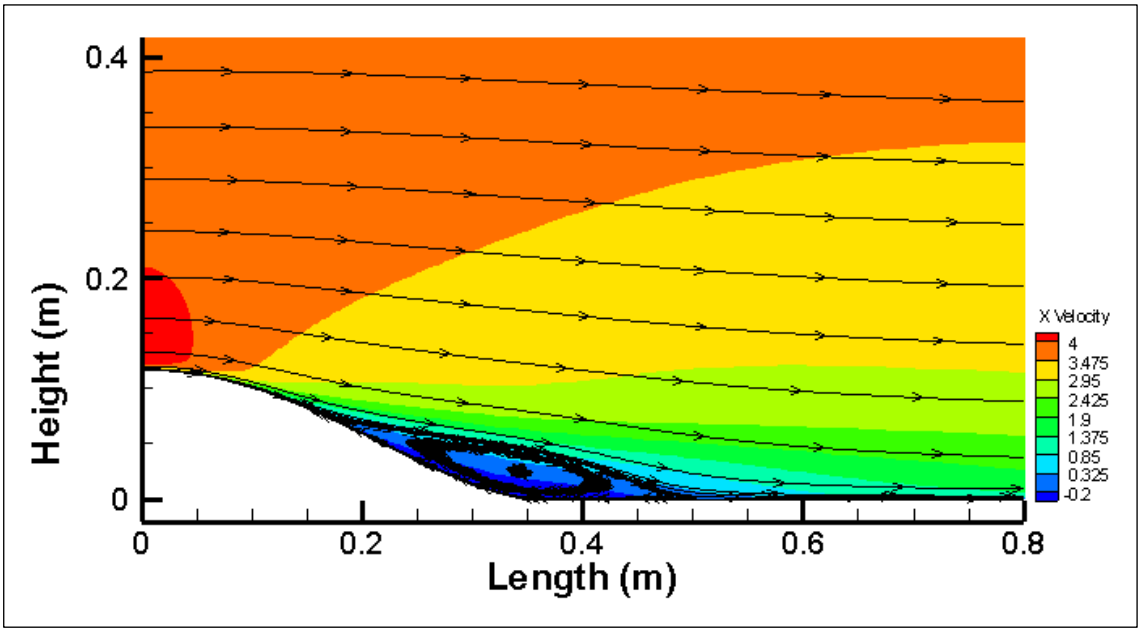

Figure 6-7 Streamlines and contours of horizontal velocity for Spalart-Allmaras model.

As can be observed in Figures 6-5, 6-6, 6-7 and 6-8, the characteristics of the recirculation zone downwind of the hill for these four models are as follows:

Turbulent Models	Separation Point (m)	Reattachment Point (m)
k-ε Standard	0.154	0.469
k-ε RNG	0.134	0.562
k-ε Realizable	0.125	0.590
Spalart-Allmaras	0.125	0.518
Numerical Results	Not available	0.479
Experimental Results	Not available	0.760

Table 6-1 Separation and reattachment points for the four models.

The separation and reattachment points were obtained from Tec plot software. Since the air comes from the left side of the domain, the flow remains unchanged until the obstacle deviates its direction as can be seen from the following section of this chapter. The velocity of the flow is also influenced by the hill and the presence of the obstacles. The velocity of the air increases generally with the height of the domain because of the atmospheric conditions and also when the flow is deviated by the hill or by any other obstacle. The deviation in the flow by the hill has the effect of generating a recirculation bubble downwind of the hill and the size of the recirculation will depend first on the dimension of the hill and second on the model used for the simulations of the case.

The contours of the horizontal velocity are not the same for all models, especially for the Spalart-Allmaras model, as can be observed from Figure 6-7. One of the differences between the k-ε models and Spalart-Allmaras model is that for the latter model, the maximum value of the velocity is at the top of the hill and for the k-ε models the maximum velocity is obtained only when the height of the hill is increased. The k-ε models also have some differences in the recirculation zone. The velocities and the reattachment zone downwind of the hill, vary depending on which model is used.

To conclude this validation part, the k-ε Standard model is the model which agrees most closely with the experimental results in this study. However, the k-ε RNG model also agrees quite well with the experiment, so for the following validation of the source point, both models will be used in order to simulate the cases and the results

will be analysed with a view to finding which model agrees more with the experiment.

6.2. The concentration fields

The examination of pollutant dispersion is represented in this section. An ethylene (C_2H_4) source point has been used for the experimental case as well as for the simulations, with a 15mm diameter porous sphere situated downwind of the hill, at y=0.5H where H is the height of the hill. The source point has been defined with a user defined function (UDF) which can be found in the Appendix. At the beginning, the coordinates of the specific cell where the source point is located have been specified. The modified equation that has been used for the UDF is the equation for the mass flow rate, which is $\dot{m} = \rho u A$ where $\dot{m}$ is the mass flow rate, ρ the density of the gas, u the velocity and A the flow area. The mass flow rate is in kg/sec and is being implemented through the following equation.

Viscosity (kg/ms)	Diffusion coefficient (m^2/s)	Thermal conductivity ($w/m-k$)
1.72×10^{-5}	2.88×10^{-5}	0.0454

Table 6-2 Ethylene properties

The mass flow rate is divided by the volume of the cell, because Fluent computes the mass flow rate by multiplying the strength of the source by the volume of the cell for each cell specified in the UDF.

In the current study, the transport equation of ethylene arises from the conservation of mass where a transport scalar is introduced in (kg / (m^3 sec)) units. The general scalar transport equation is shown below with the four terms (unsteady, flux, diffusivity, and source).

$$\underbrace{\frac{\partial \rho_{eth}}{\partial t}}_{unsteady} + \frac{\partial}{\partial x_i}\left(\underbrace{\rho_{eth} u_i}_{convection} - \Gamma \underbrace{\frac{\partial \rho_{eth}}{\partial x_i}}_{diffusion} \right) = \underbrace{S_\phi}_{sources}$$

Where Γ : diffusion coefficient, S_ϕ : source term (kg / (m^3 sec))

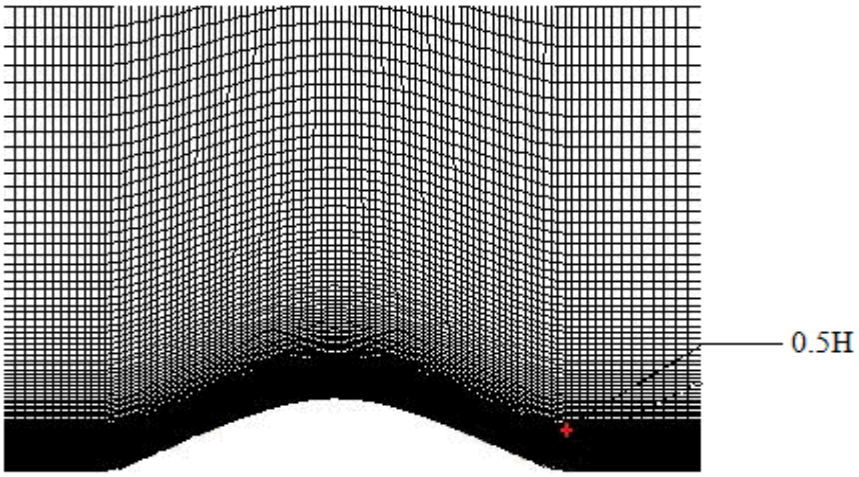

Figure 6-8 Position of the emissions for the single hill case.

Two turbulent models are illustrated in Figure 6-9, the k-ε Standard and the k-ε RNG models.

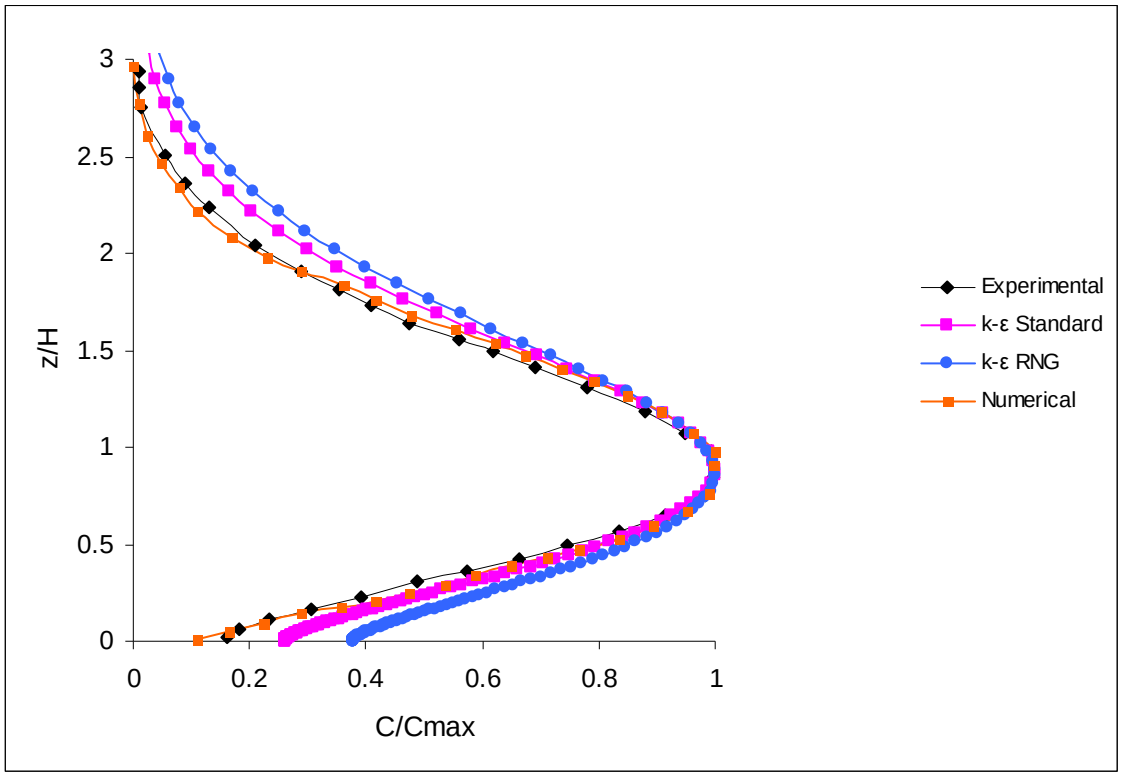

Figure 6-9 Concentration profiles in flat terrain and normalised by the maximum ground level concentration (Cmax).

As can be observed from Figure 6-9, the k-ε Standard model is closer to the experiment, than the k-ε RNG model. At the beginning both lines are not matching

the experiment but the k-ε Standard model is closer to the experiment. Furthermore, the numerical data shows that agreement with experiment is very good.

Figure 6-10 shows the ground level concentrations and the difference between those two models with the experiment. The ground level concentration is normalised by the corresponding maximum ground level concentration over flat terrain. At the beginning the lines are very similar and both lines follow almost the same trend as the experimental line but the line of the k-ε Standard model is closer to the experiment than the k-ε RNG model.

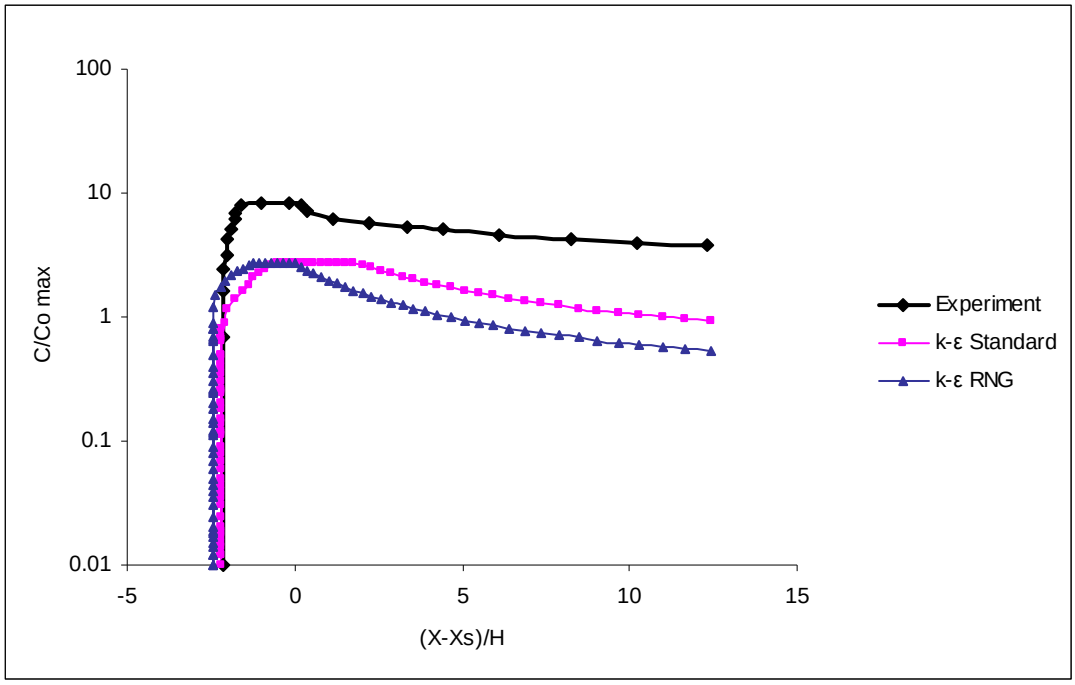

Figure 6-10 Ground level concentrations with source for the single hill case at downwind base and height: 0.5H for the second scheme order.

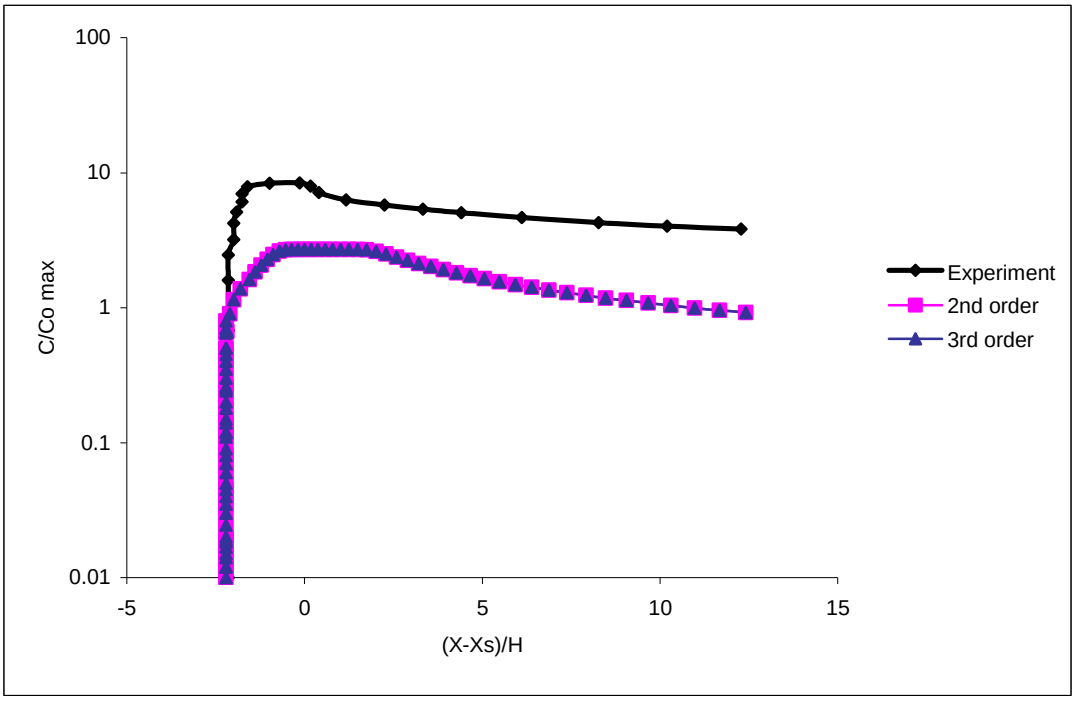

Figure 6-11 Ground level concentrations with source for the single hill case at downwind base and height: 0.5H for the 2nd and 3rd order scheme.

From the graph in Figure 6-10, it can be also seen that the ground level concentration of the k-ε Standard model is lower than the experimental concentrations. In order to be convinced that the k-ε Standard model is the most appropriate for this study, the same case is simulated from the second order to the third order scheme in order to observe if any changes occur with the results. As can be seen from Figure 6-11, there is no difference and the results are still the same. Consequently all the simulations of this study will be based on the second order scheme of the k-ε Standard model.

Chapter 7

7. Results and Discussion

Using the validated model (for inert and reactive flow), which finally is the k-ε Standard turbulent model, and focusing on the validation of previous cases, the work of Kim et al. [8] is going to be extended into a regime where the ratio of the height of the buildings to the height of the hill is smaller. In their paper they did not consider a real life simulation but they have studied more basic fluid mechanics.

They considered the case of gas dispersion in the wake of a hill which also had a number of buildings. In detail they considered, height of the hill to the height of the building ratio of 1.92, 1.47, 1, and 0.65 (where the height of the buildings is more than the half hill's height).

This study considers the ratio of the height of 5.85, (buildings lower than the hill which often occurs in countries like Greece where small towns/villages are located close to large hills) and also this ratio is going to be constant and the location of the source will be varied.

For the analysis of the results, profiles of ethylene in a number of locations are considered. Moreover, these profiles are compared against profiles without obstacles and against flat terrain, in order to check the dispersion of the pollutant in each case, and also to test the reaction and the difference of the pollutant distribution in each case. (The flat terrain case will be examined in order to see how the flow and the emissions react without the presence of any hill or obstacle).

The numerical model is a two-dimensional incompressible steady model. The cases considered in this study are: a single hill with three obstacles (Figure 7-1), a single hill (Figure 7-3), a flat terrain (Figure 7-4), and all these cases with the source points located in eight different positions.

7.1. Computational Set-up

The inlet and the top boundary should be 5H away from the obstacle, where H is the height of the tallest obstacle. The outflow boundary should be positioned at least 15H behind the obstacle to allow flow development, as fully developed flow is normally used as a boundary condition. For the same reason this outflow length should also be applied in an urban area with many obstacles (buildings), where H is to be replaced by Hmax, the height of the tallest obstacle [62].

The computational domain dimensions in the horizontal axis are: x=9360mm and in the vertical axis y=1602mm. These dimensions are chosen for the simulations, which have been validated before. The height of the hill is 117mm and the centre of the hill is located at x=0 mm. The height of the symmetrical obstacles are 20mm, width 25mm and the distance between the obstacles is 35mm.The first obstacle is at x=355mm. The grid at the area of interest is finer, as can be seen at the following figures, this is so that the results are more accurate (near the areas of interest).

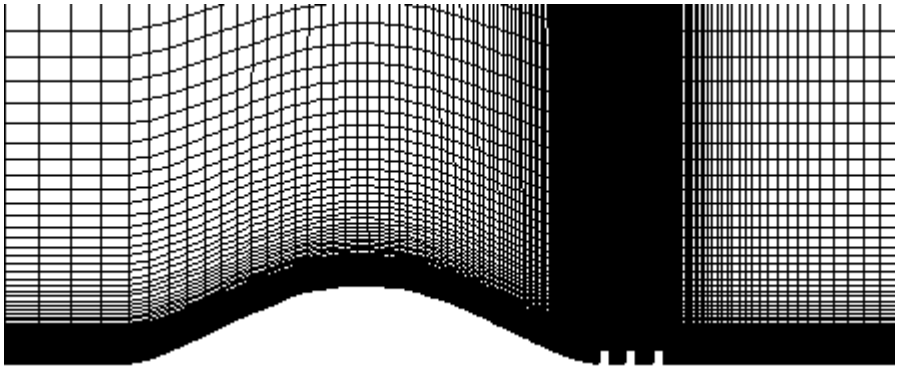

Figure 7-1 Grid of the computational domain for the hill with obstacles.

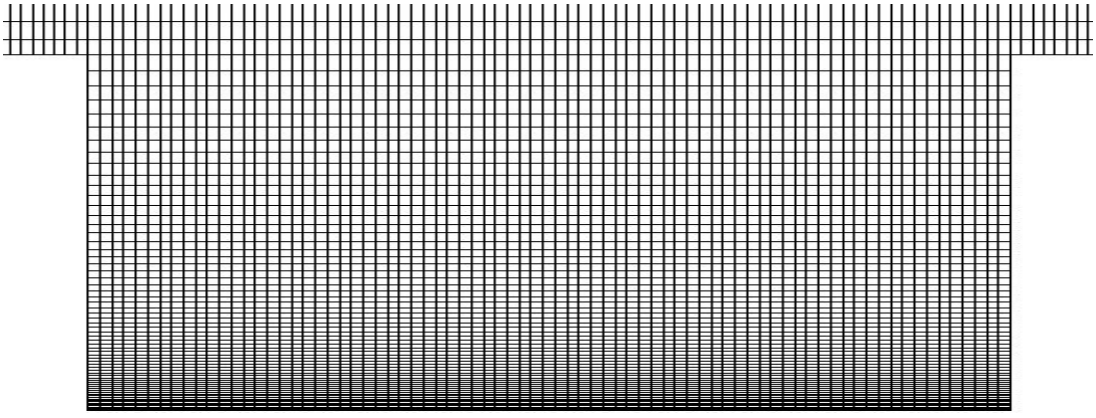

Figure 7-2 Grid between the two obstacles.

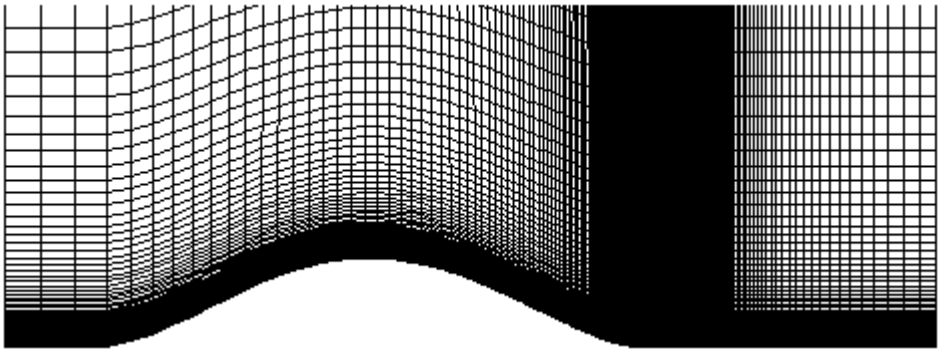

Figure 7-3 Grid of the computational domain for the single hill.

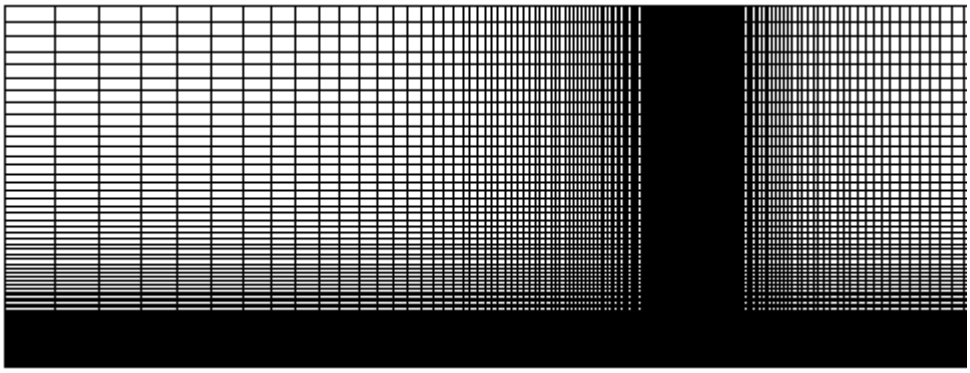

Figure 7-4 Grid of the computational domain for the flat terrain.

The computational domain has quadrilateral cells with a finer resolution close to the ground and in those regions where the emissions take place. The final number of the computational quadrilateral cells is 40725. The smallest cell dimension is 5.52366×10^{-5} m^2 and at the previous grid which was used for the validation study, the number of cells were 32000 and smallest cell was 5.679705×10^{-5} m^2.

7.2. Boundary Conditions

The boundary conditions are classified as follows:

At the inflow boundary a velocity inlet is used, in order to specify the velocity of the domain. Thus, a UDF was used for the inlet velocity profile. This is an atmospheric boundary layer (ABL) velocity profile, used in order to specify the velocity of the domain. At the bottom, where the ground is, a wall boundary is used, to bind fluid and solid regions. At the boundary behind the obstacles, where the fluid leaves the computational domain, an outflow boundary is used [62]. Outflow boundary conditions are used to model flows where the details of the flow and pressure are not known prior to the solution of the flow problem. At the top, a symmetry boundary is set down which enforces the parallel flow. The following subsections are showing the results of simulations of a single hill with one, two and three obstacles without any pollutant in order to understand the flow around this specific area.

7.3. A single obstacle in the recirculation bubble

7.3.1. Without emissions

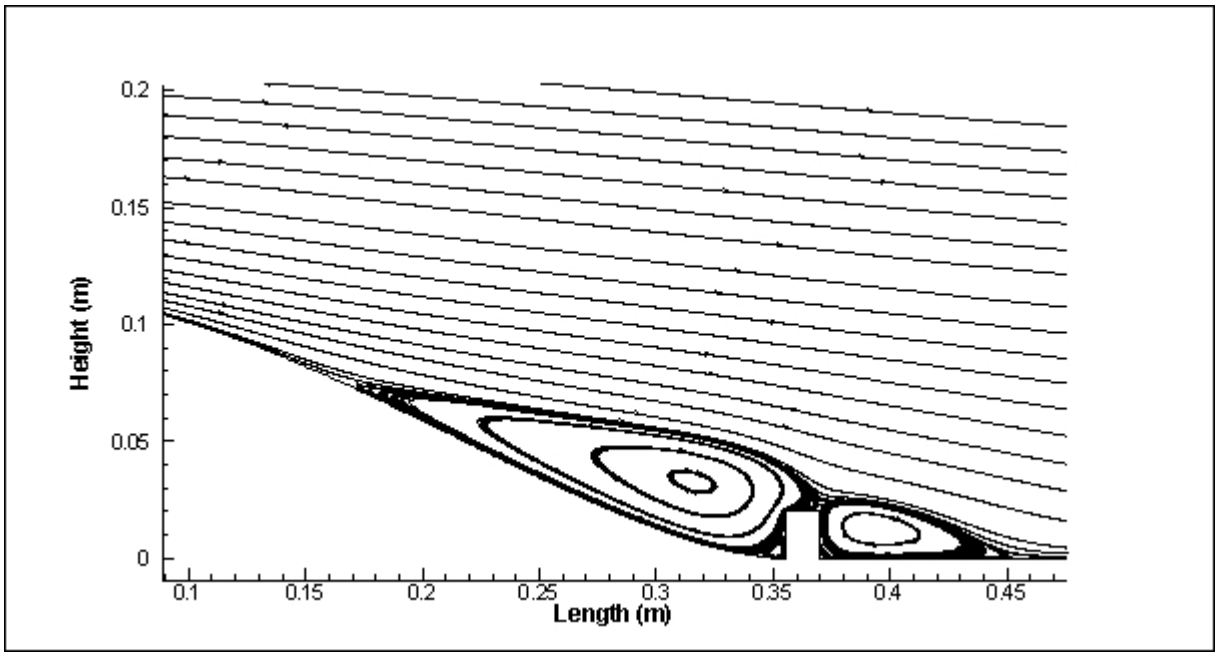

Figure 7-5 Streamlines of velocity for the case of single hill with one obstacle.

In Figure 7-5, streamline fields are represented and show clearly that the flow is characterised by a recirculation zone downwind from the hill. The recirculation zone is cut in the middle by one obstacle corresponding to a building. Two vortices are formed at this area, one upwind of this obstacle and the other downwind of it. The upwind vortex is greater than the downwind which is connected to it at 0.37m. The whole recirculation is located between x=0.154 m and x=0.452m.

7.4. Two obstacles in the recirculation bubble

7.4.1. Without emissions

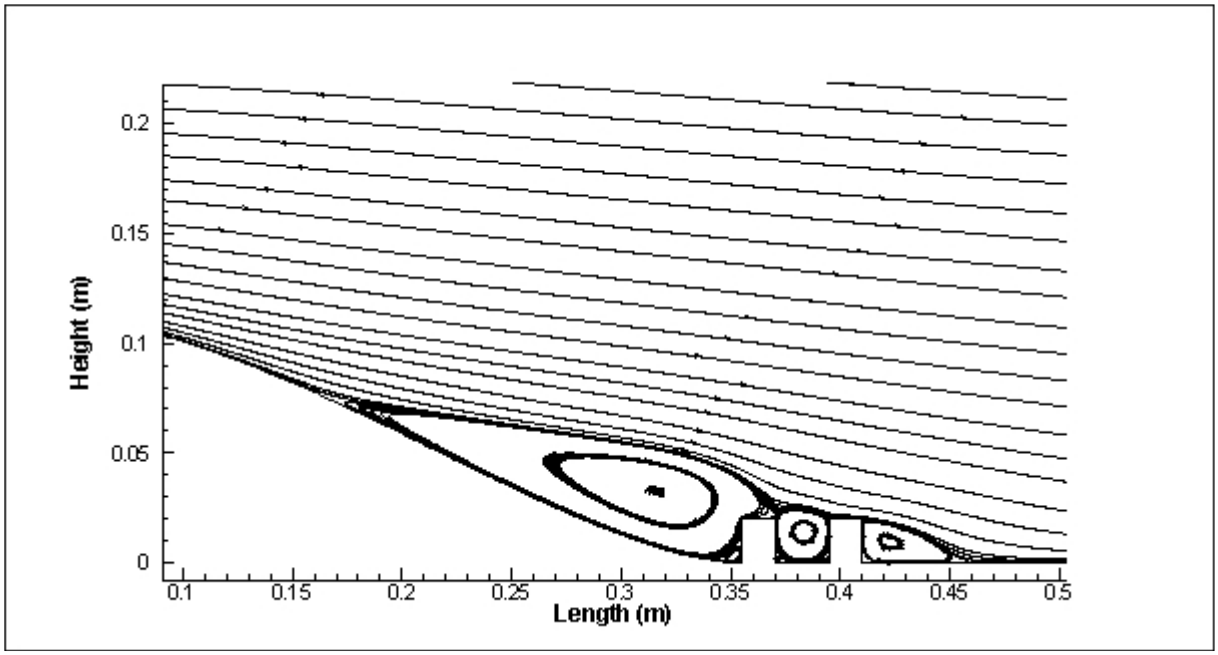

Figure 7-6 Streamlines of velocity for the case of single hill with two obstacles.

In Figure 7-6, streamlines are represented and illustrate the flow which is characterised by a recirculation zone downwind from the hill. In this case the recirculation zone is cut into three parts by two obstacles. Three vortices are formed in this area, one is upwind of the first obstacle, another is between the two buildings (street canyon) and the last vortex is downwind of the last obstacle. The vortices are almost trapped inside the street canyon and their maximum height is almost the height of the obstacles. The strength of the second vortex (inside the street canyon) is greater than the third vortex because the first vortex, which is upwind of the first obstacle, is coming in on the top of the obstacle and is more connected with the second vortex

than the third. At the point of x=0.37m, the biggest vortex is connected to the vortex inside the canyon. Downwind of the last obstacle the recirculation region is between x=0.410m and x=0.461m. For this case the separation is at x=0.154m and the reattachment is at a distance of 0.461m. As far as the reattachment point is concerned, this case has a small difference compared to the first case which has its reattachment point at a distance of x=0.452m.

7.5. Three obstacles in the recirculation bubble

7.5.1. Without emissions

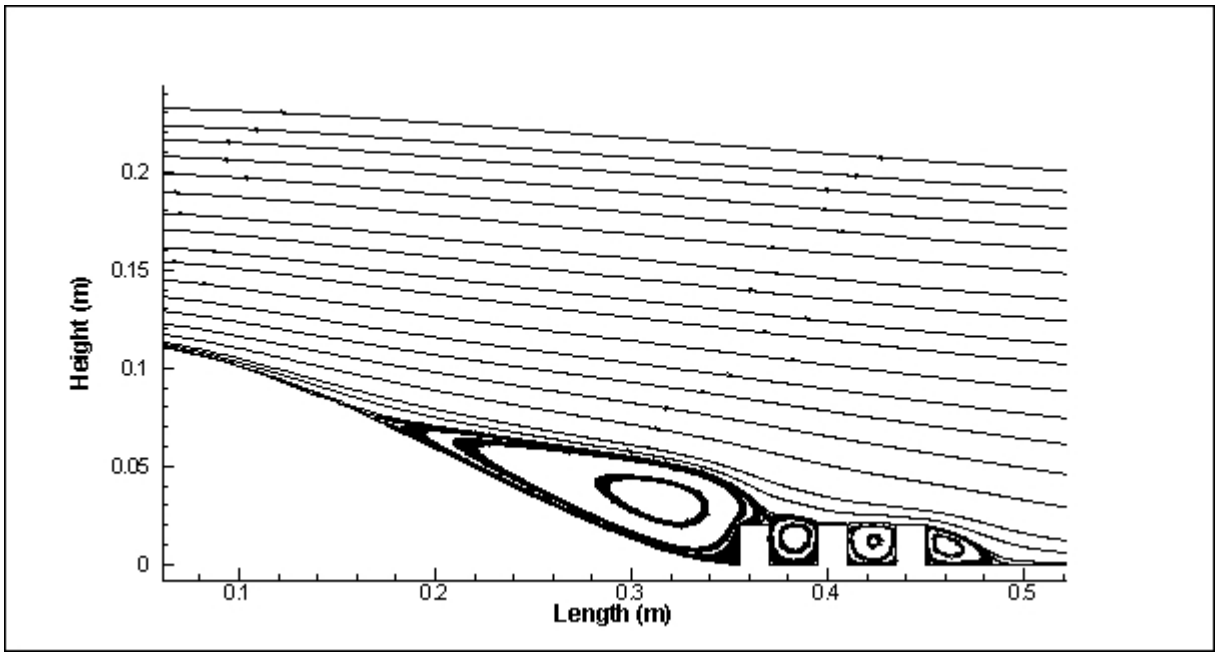

Figure 7-7 Streamlines of velocity for the case of single hill with obstacles.

The same phenomenon occurs for the case with the single hill and the three obstacles (Figure 7-7). The separation for all these cases is the same and is located at x=0.154m. The first vortex is connected with the second one at the same position as in the previous cases, at as distance of x=0.37m. Also, the strength of the second vortex is stronger than the other two and this is due to the first recirculation bubble which is larger, so the first recirculation bubble comes on the top of the second one. The reattachment also changes in this case and is located at x=0.490m. The reattachment point is bigger for this case and this is due to the existence of the three obstacles.

7.6. Dispersion characteristics

A horizontal release of ethylene from a flow area A with a velocity of u at a height of one metre over the ground is examined. The height of the source is chosen to be in the same condition as the experimental study conducted by Khurshdyan et al. [17].
The equation for the source of ethylene is specified by:

$$source = (d * u * A / C\_Volume(c,t))$$

With:
Density (d): 1.178
Velocity (u): 0.09m/s
Cross section area (A): 0.047m^2
Volume of the cell (C_Volume (c,t)):

This equation is used to describe an accidental release from a source like pipelines in the industry.
Ethylene is generally transported by pipelines from the storage area located away from the reaction units in order to be transformed. If a fraction of the pipeline is located near an urban area (for example in a road) a different accident scenario (leak, rupture, damage) can be considered and in this case an ethylene release can happen. Liquid Natural Gas (LNG) is also generally transported by pipelines. Cleaver et al. [68] have investigated for Advantica Ltd the risks of LNG for the environment. Advantica has recently conducted on behalf of BP (British Petroleum) a review of LNG explosions and gas dispersion. For the simulations realised in this project a mass rate release of 0.005kg/s is considered for the case of ethylene release. Advantica has used the same mass flow rate release for an LNG release.
Ethylene acts as a simple asphyxiant and has the capability of displacing the oxygen in the atmosphere. The latter characteristic automatically makes ethylene a significant health hazard. Since it is a gas, it can spread over a wide area. Another characteristic of ethylene is that it can experience a violent chemical reaction at high temperatures. Ethylene produces toxic effects and those can lead to animal deaths or even low growth rate in plants. Large amounts of ethylene can have a huge negative impact on the available amount of oxygen [69].

The main characteristics of ethylene (C_2H_4) are the following:

- Physical state at $20^{\circ}C$: Gas
- Colourless
- Slightly sweet odour
- Flammable gas
- Flammability range [vol% in air]: 2.4 to 34
- Auto-ignition temperature [°C] : 425

Another side-effect of ethylene is anaesthesia which can be caused by exposure to extremely low concentrations of this gas (20%). So, low concentrations of ethylene can cause an oxygen deficient environment, whose symptoms can cause:

- Headaches
- Dizziness
- Drowsiness
- Nausea
- Depression of all senses
- Death (under certain circumstances)

Like all hydrocarbons, ethylene is an asphyxiant and combustible. As an asphyxiant gas, ethylene dilutes or displaces the oxygen-containing atmosphere, leading to death by asphyxiation if breathed long enough.

Concentration	**Symptoms of Exposure**
12-16% Oxygen	Breathing & pulse rate increased, muscular coordination slightly disturbed
10-14% Oxygen	Emotional upset, abnormal fatigue, disturbed respiration
6-10% Oxygen	Nausea & vomiting, collapse or loss of consciousness
Below 6% Oxygen	Convulsive movements, possible respiratory collapse & death

Table 7-1 The symptoms of exposure in functions of concentration [69].

In the petrochemical industry ethylene is being produced by steam cracking. By steam cracking of a wide range of hydrocarbon feed-stocks, ethylene can be produced commercially. Ethylene is obtained mainly from cracking naphtha, gasoil and condensates. This method is widespread in Europe and Asia [70]. In South Africa ethylene is produced by using a different method, where small quantities of dilute ethylene can be obtained from refinery streams. This is a process from gases obtained from coal, gasoil and condensates. Different methods are being used in order to crack crude or residual oil but these are considered to be very expensive.

As far as the production of ethylene is concerned, there are many factors, mainly developmental and environmental, that can affect it. During the life of the plant, ethylene production is stimulated during certain stages of growth such as:

- Germination
- Ripening of fruits
- Abscission of leaves
- Senescence of flowers

Concurrently, ethylene production is stimulated by some external aspects such as:

- Mechanical wounding
- Environmental stresses
- Certain chemicals such as auxin and other regulators

The following cases will be examined by placing the source point at eight different positions downwind of the hill, in order to observe the flow around the hill and to measure the emission concentrations upwind and downwind of the obstacles. The most complex case in this study is the one with the hill and three obstacles which is chosen for the following simulations. The maximal and minimal concentrations of pollutant will also be determined regarding the position of the source and their effect on the emissions.

Position at the x axis (m)	Position at the y axis (m)
0.035	118
0.071	117
0.120	94.2
0.165	75.6
0.208	55.2
0.235	42.4
0.272	25.1
0.310	9.9

Table 7-2 Eight coordinates of each source along the hill.

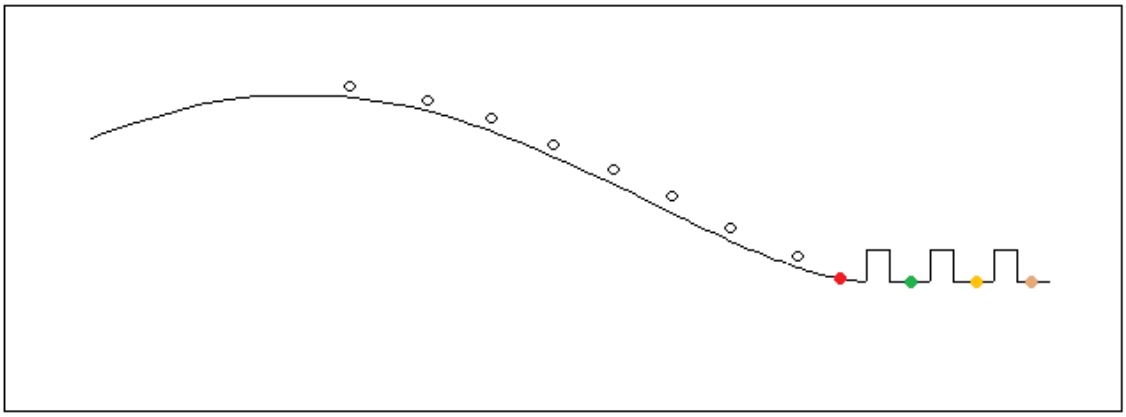

Figure 7-8 Positions where the emissions are along the hill and where the data are collected next to the obstacles.

As can be seen from Figure 7-8, for the case with the hill and obstacles, the first location where the data are selected is at x=0.3425m (●), which is 0.0125m upwind of the first obstacle, the second and the third points are at x=0.3825m (●), and x=0.4225m (●), which are in the middle of the first and second street canyons respectively and the last location is at x=0.4625m (●), which is 0.0125m downwind of the last obstacle. The same locations are also used for the single hill case and for the flat terrain case respectively.

7.7. Determination of ethylene mass fraction upwind of the first obstacle

7.7.1. Hill with obstacles:

Figure 7-9 represents the case of the hill with obstacles and the exact location where the data of the pollutant are collected.

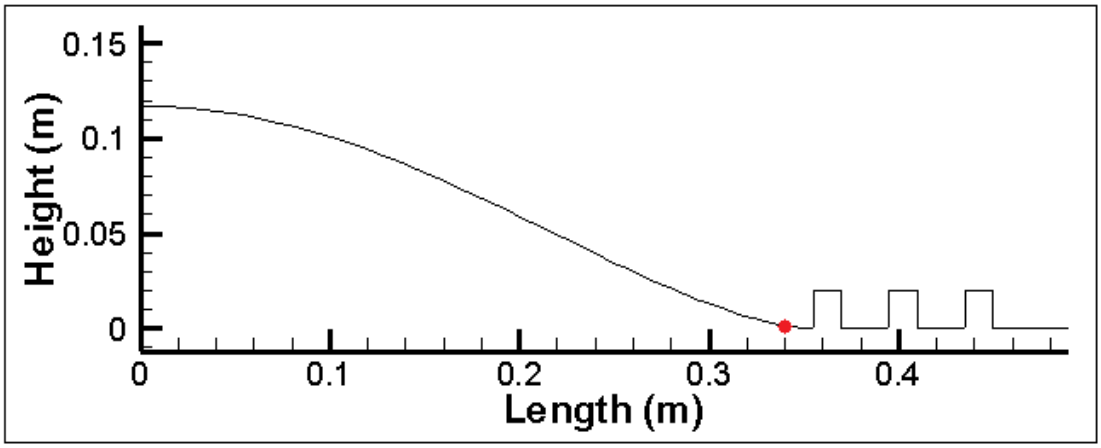

Figure 7-9 Position of collection of the data at x=0.3425m.

The examination of pollutant dispersion at x=0.3425m, with the existence of three obstacles is represented in Figure 7-10:

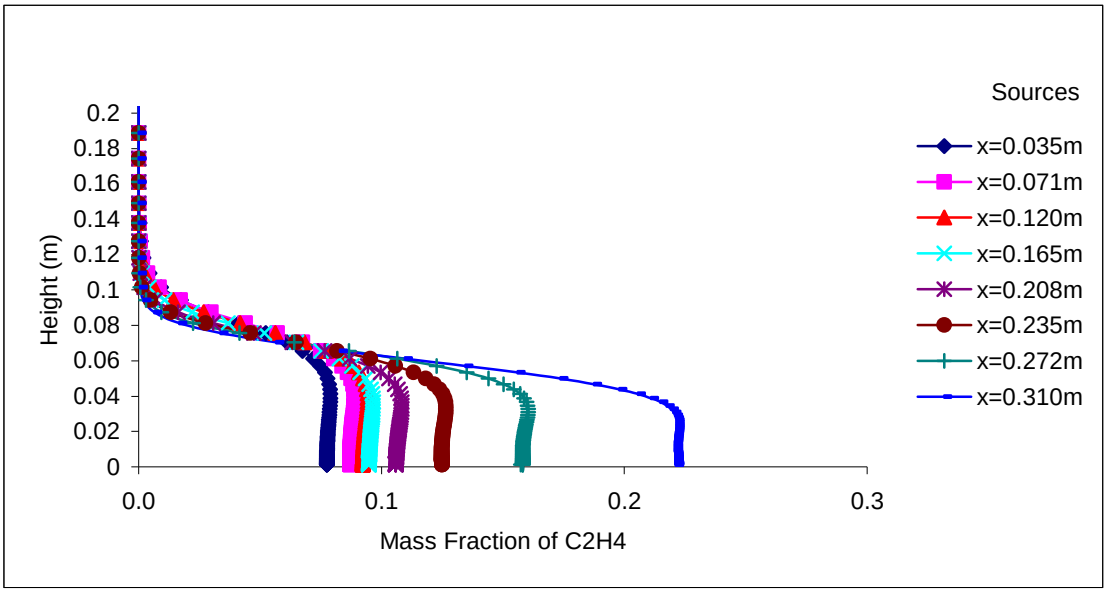

Figure 7-10 Vertical profiles of mass fraction at x=0.3425m, from eight sources, for a single hill with obstacles configuration.

As the air comes from the left side of the domain and the plume passes over the downwind base of a hill, it has been observed that the minimum concentration is 0.078 and is obtained from the source located at x=0.035m, which is far away from the point where the data are collected, as can be observed from Figure 7-11.

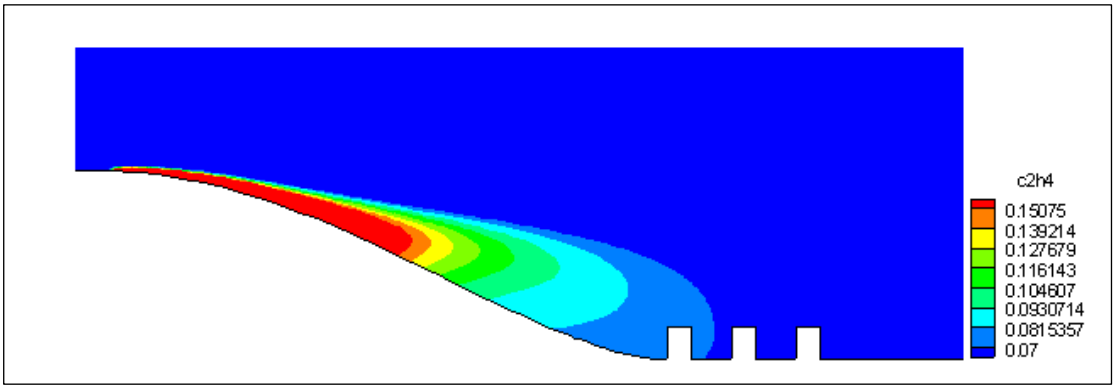

Figure 7-11 Emissions of ethylene from the source located at x=0.035m.

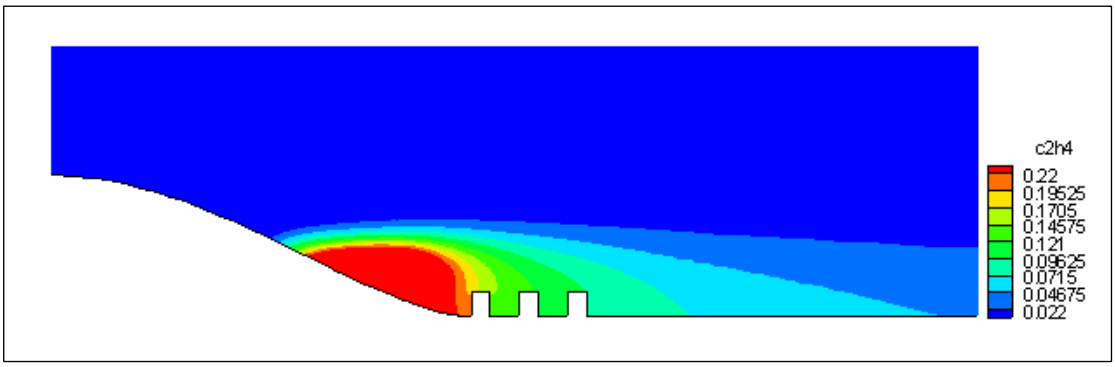

Figure 7-12 Emissions of ethylene from the source located at x=0.310m.

When the source is located at x=0.310m (Figure 7-12), which is the closest source near the first obstacle the maximum mass fraction is 0.22. The next maximum mass fraction is when the source is located at x=0.272m and the next one at x=0.235m with a mass fraction of 0.16 and 0.13 respectively. The mass fractions when the source is located at x=0.120m and x=0.165m are comparable, at 0.094 and 0.096 respectively, even though the first position is outside the recirculation zone.

7.7.2. Single Hill

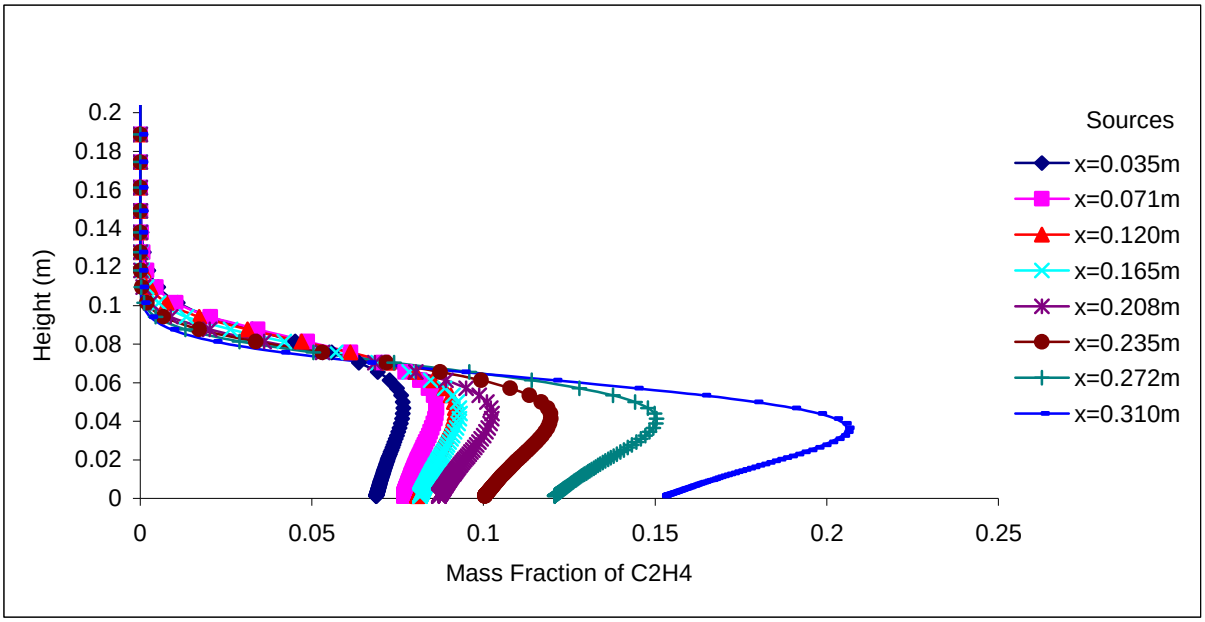

Figure 7-13 Vertical profiles of mass fraction at x=0.3425m, from eight sources, for a single hill configuration.

As shown in Figure 7-13, the minimum mass fraction is 0.0766 when the source is located at x=0.035m and the maximum mass fraction is 0.155 when the source is located at x=0.310m. Figures 7-14 and 7-15 show the contours of a concentration of ethylene and help in understanding (at the location where the data are collected), that the amount of pollutant emitted from the source located at x=0.035m is lower than the emissions from the source at x=0.310m. Moreover, the sources located at x=0.120m and x=0.165m are emitting the same quantity of pollutant, at (0.3425,0) where the data are collected.

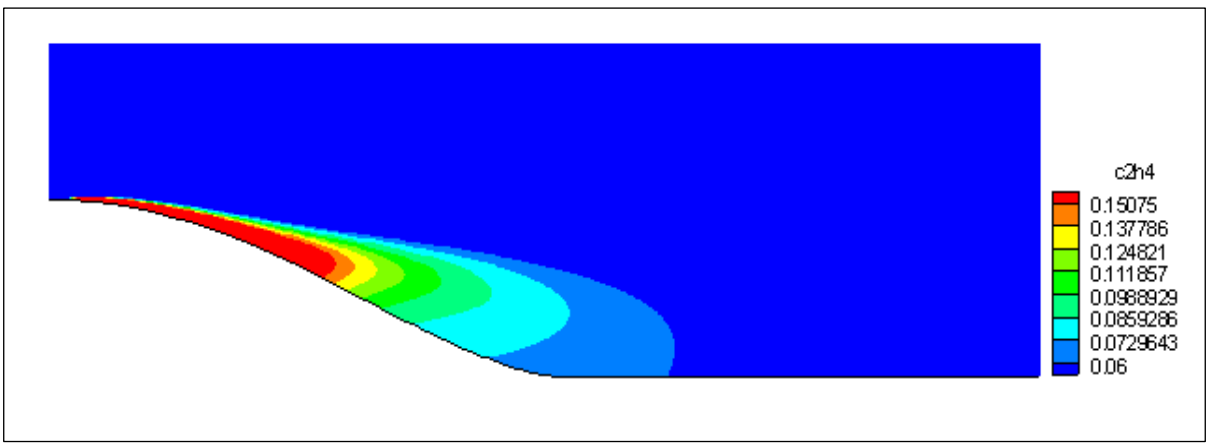

Figure 7-14 Emissions of ethylene from the source located at the top of the hill (x=0.035m).

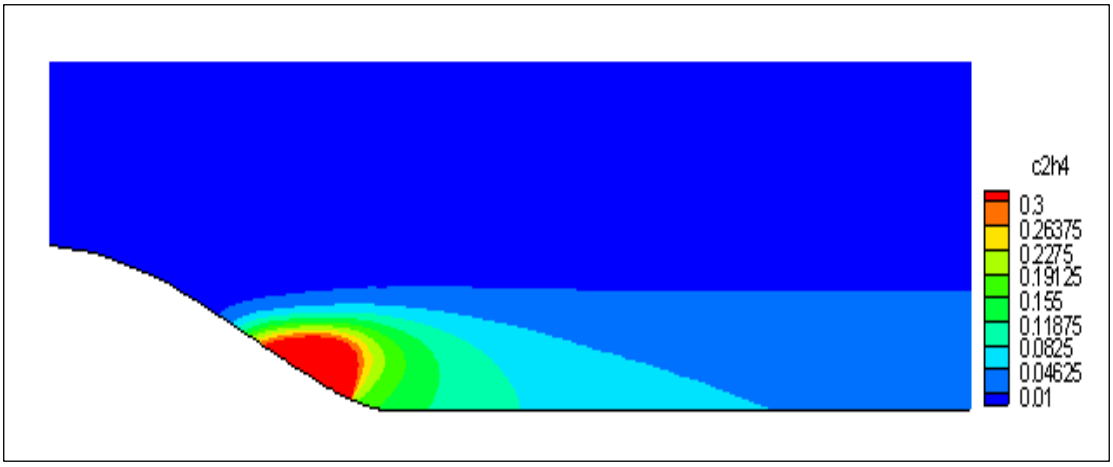

Figure 7-15 Emissions of ethylene from the source located downwind of the hill (x=0.310m).

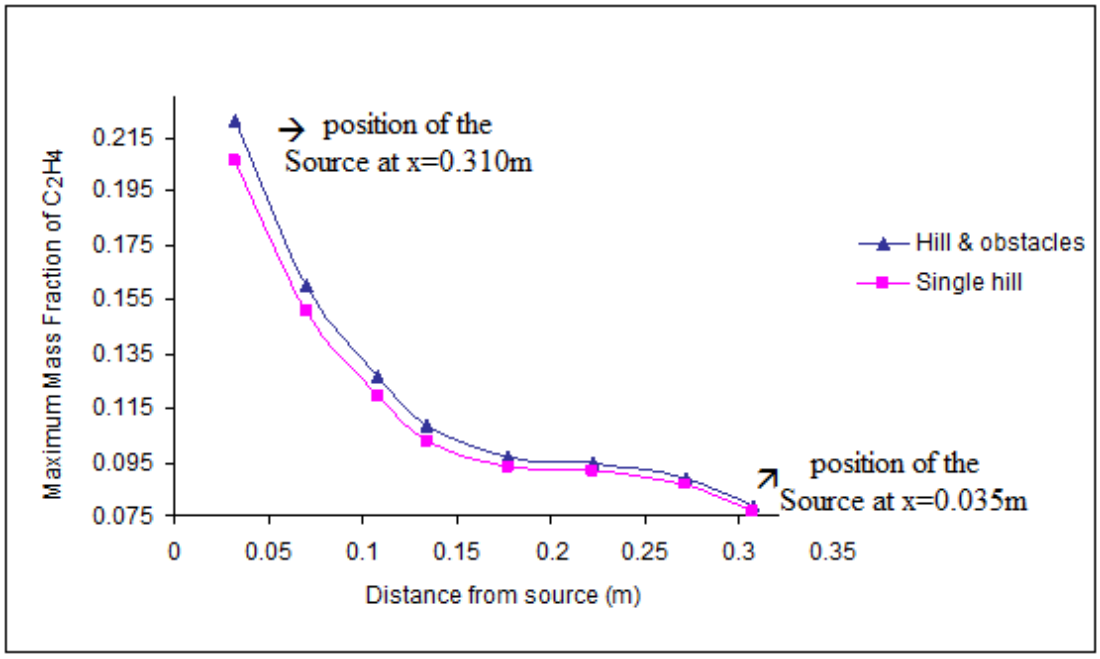

Figure 7-16 Maximum mass fraction of C_2H_4 for two cases.

In Figure 7-16 the x axis represents the distance between the point source (x_s) and the location of extracted the data (x), $(x - x_s)$. The examination of pollutant dispersion for the case of a single hill and hill with obstacles is at (0.3425,0). The point sources are in eight various positions each time. This comparison has been done in order to see in which case between a single hill and a hill with obstacle has less pollutant. Figure 7-16 shows the maximum mass fraction at the same location of the point source for both cases. It can be seen that the mass fraction near the upwind side of the

obstacle is larger for the case of the hill with the obstacles; it has larger values of ethylene than the single hill case. This is due to the vortices that appear upwind of the obstacle where a large amount of pollutant is trapped.

7.7.3. Flat Terrain

For the flat terrain case, by measuring the ethylene at the same position as before, it has been observed that the values of pollutant have increased. By placing the emissions at x=0.035m, the minimum mass fraction is 0.135 and at (0.310, 0) (Figure 7-18) the concentration is 0.89 as can be observed from Figure 7-17:

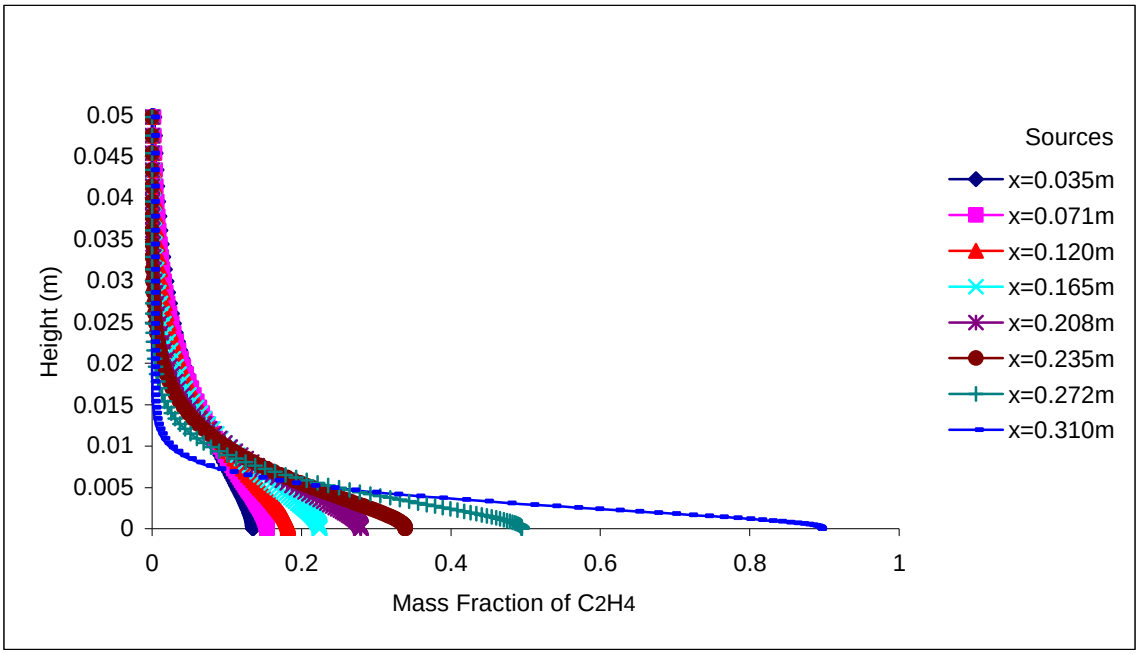

Figure 7-17 Vertical profiles of mass fraction at x=0.3425m, from eight sources, for a flat terrain configuration.

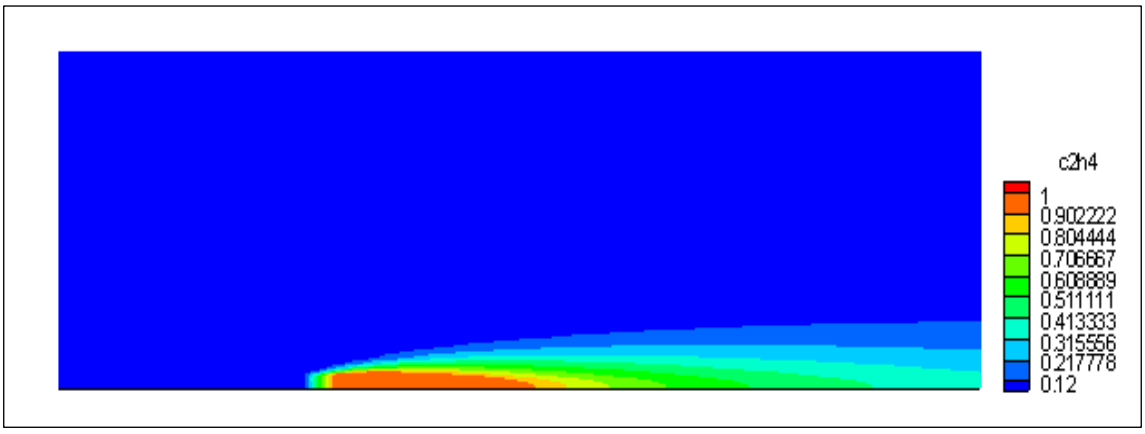

Figure 7-18 Emissions of ethylene from the source located at x=0.310m.

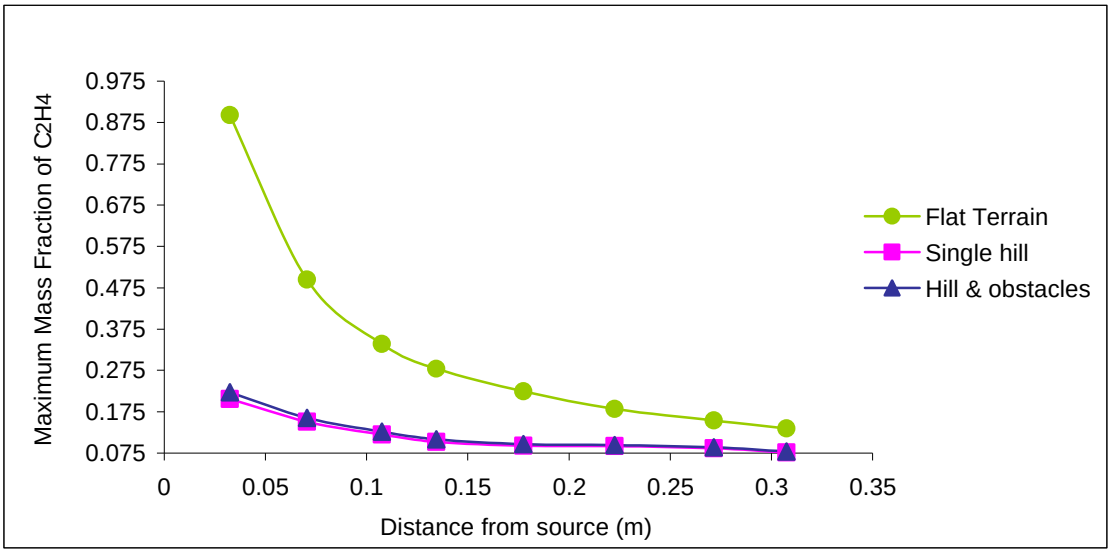

Figure 7-19 Maximum mass fraction of C_2H_4 at x=0.3425m for all cases.

In Figure 7-19 the x axis represents the distance between the point source (x_s) and the location of extracted the data $(x),(x-x_s)$. The examination of pollutant dispersion for the case of a single hill, hill with obstacles, flat terrain is at (0.3425,0). For the case of the flat terrain, all the concentrations of ethylene are higher than the other two cases. On average the pollutant of the flat terrain is 63.8% larger than the case with the hill and the obstacles and 65.7% more than the single hill case.

7.8. Determination of ethylene mass fraction in the middle of the first street canyon

7.8.1. Hill with obstacles:

Figure 7-20 represents the case of the hill with the obstacles and the exact location where the data of the pollutant are collected.

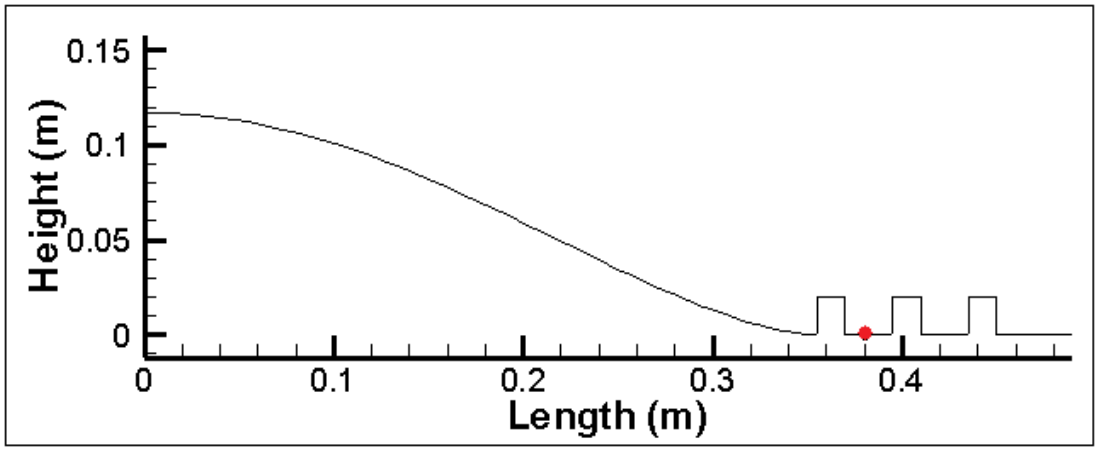

Figure 7-20 Position of collection of the data at x=0.3825m.

Figure 7-21 represents the pollutant inside the street canyon (x=0.3825m).

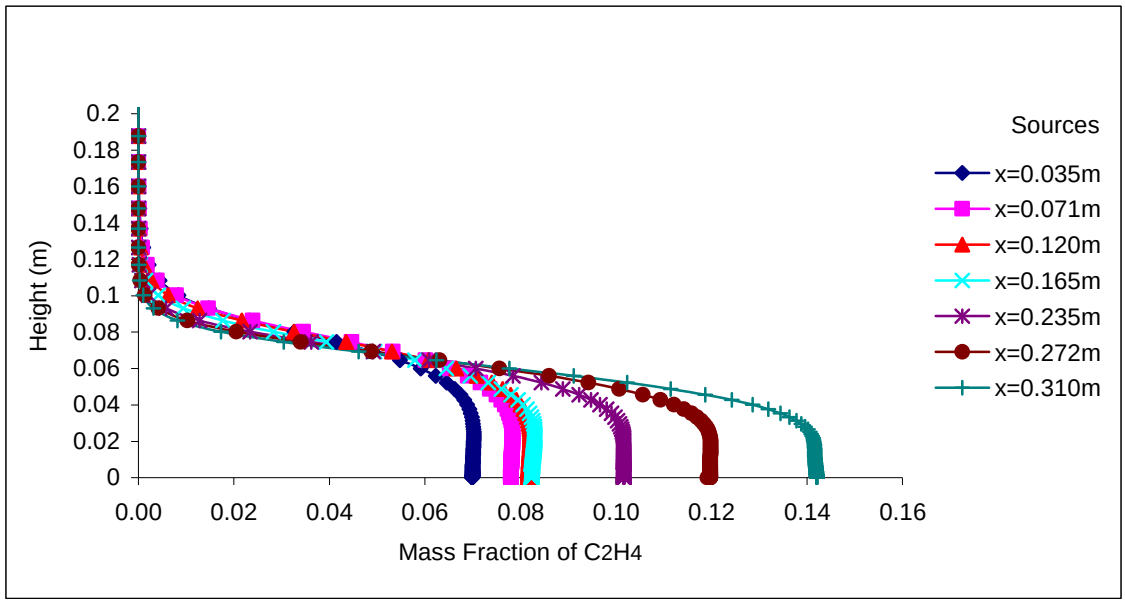

Figure 7-21 Vertical profiles of mass fraction at x=0.3825m, from eight sources, for a single hill with obstacles configuration.

In Figure 7-21, the minimum mass fraction which corresponds to 0.07 is given by the source located at x=0.035m, and the maximum pollutant corresponds to 0.142 for the source located at x=0.310m.

7.8.2. Single Hill

Figure 7-22 shows the vertical profiles of the pollutant emissions for the single hill case:

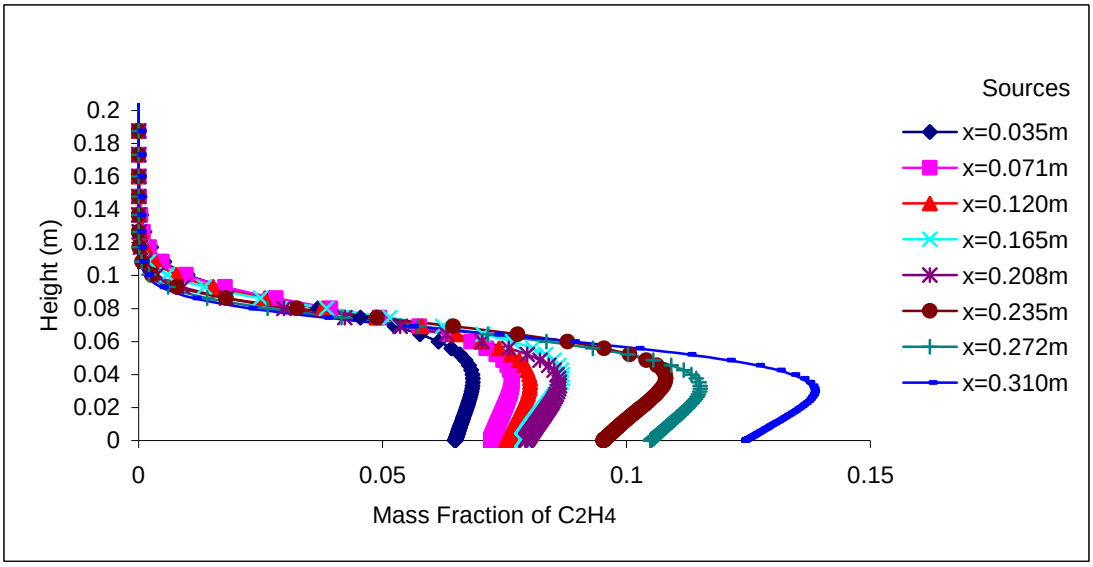

Figure 7-22 Vertical profiles of mass fraction at x=0.3825m, from eight sources, for a single hill configuration.

Figure 7-22 shows the vertical profiles of the mass fraction when the data are collected at x=0.3825m. For this case it can be observed that the values of the mass fraction have decreased, the minimum is 0.068 when the source is located at x=0.035m, and the maximum is 0.14 when the source is located at x=0.310m. Also, when the source is located at x=0.165m and at x=0.208m which are both located inside the recirculation zone, the mass fractions are very close, approximately 0.0868 and 0.0862 respectively.

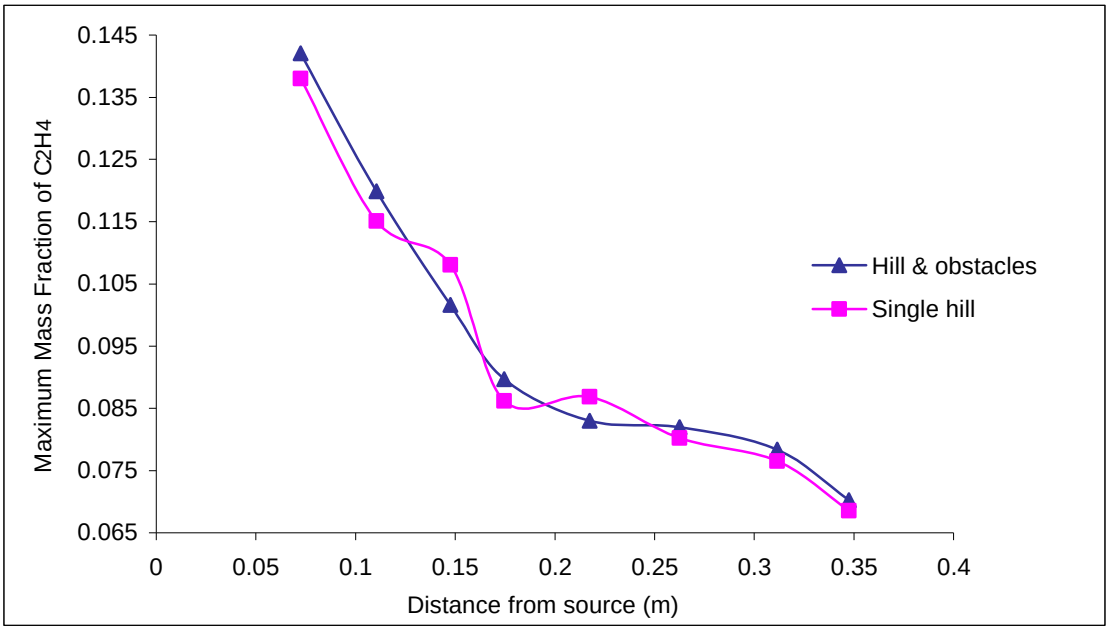

Figure 7-23 Maximum mass fraction of C_2H_4 for two cases.

In Figure 7-23 the x axis represents the distance between the point source (x_s) and the location of extracted the data (x), $(x - x_s)$. The examination of pollutant dispersion for the case of a single hill and hill with obstacles is at (0.3825,0). Figure 7-23 shows the maximum mass fraction at x=0.3825m for two cases, the single hill and the hill with obstacles. It can be seen that the profile of the mass fraction at the middle of the first street canyon, which is investigated in this part, is higher for the case of the hill with obstacles, except when the sources of the emissions are located at x=0.165m and at x=0.235m where the values for the single hill case are higher. These discrepancies they might appear because of the streamlines that they are passing from this specific position of extracted the data and the pollutant is more at this specific points. As it has been pointed out in the previous section, the mass fraction inside the first canyon for the case of the hill with obstacles is higher than the single hill case, and this is due to the vortices inside the canyon, which trap emissions inside the recirculation bubbles.

7.8.3. Flat Terrain

For the case of the flat terrain, by measuring the concentrations at x=0.3825m it can be observed from Figure 7-24, that the minimum mass fraction is from the source located at x=0.035m, which is 0.12, and the maximum is from the source located at x=0.310m with a mass fraction of 0.47.

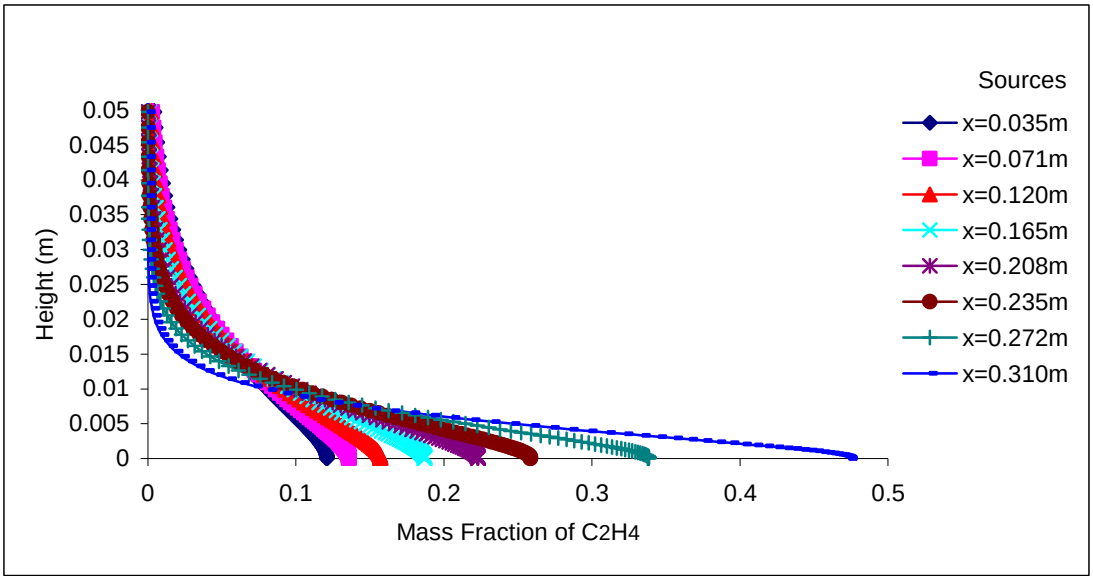

Figure 7-24 Vertical profiles of mass fraction at x=0.3825m, from eight sources, for a flat terrain configuration.

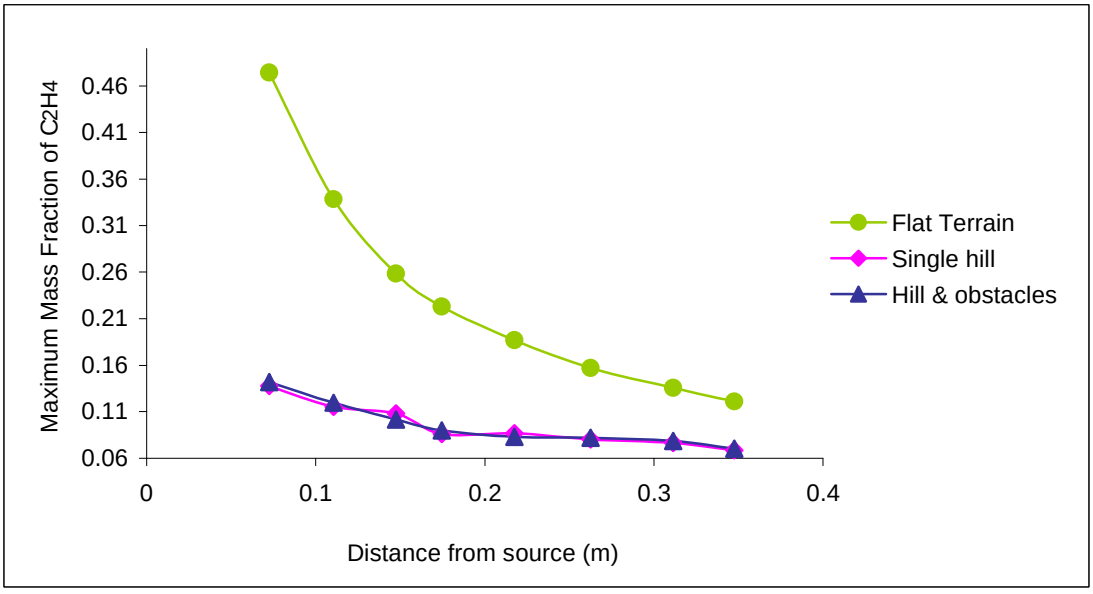

Figure 7-25 Maximum mass fraction of C_2H_4 at x=0.3825m for all cases.

In Figure 7-25 the x axis represents the distance between the point source (x_s) and the location of extracted the data $(x),(x-x_s)$. The examination of pollutant dispersion for the case of a single hill and hill with obstacles is at (0.3825,0). Figure 7-23 shows the maximum mass fraction at x=0.3825m for two cases, the single hill and the hill with obstacles.It can be observed from Figure 7-25 that the case with the higher mass fraction is the flat terrain case. Between the other two cases, the case with the higher mass fraction at the location of x=0.3825m is the case with the hill and

obstacles, which has on average 0.95% larger mass fraction than the single hill case. However, for the single hill case when the location of the source is at x=0.120m and at x=0.208m, the mass fraction is higher than the case of the hill with obstacles.
The flat terrain case has on average 59.52% larger mass fraction than the case of the hill with the obstacles and 59.9% larger mass fraction than the single hill case.

7.9. Determination of ethylene mass fraction in the middle of the second street canyon

7.9.1. Hill with obstacles:

Figure 7-26 represents the case of the hill with obstacles and the exact location where the data of the pollutant are collected.

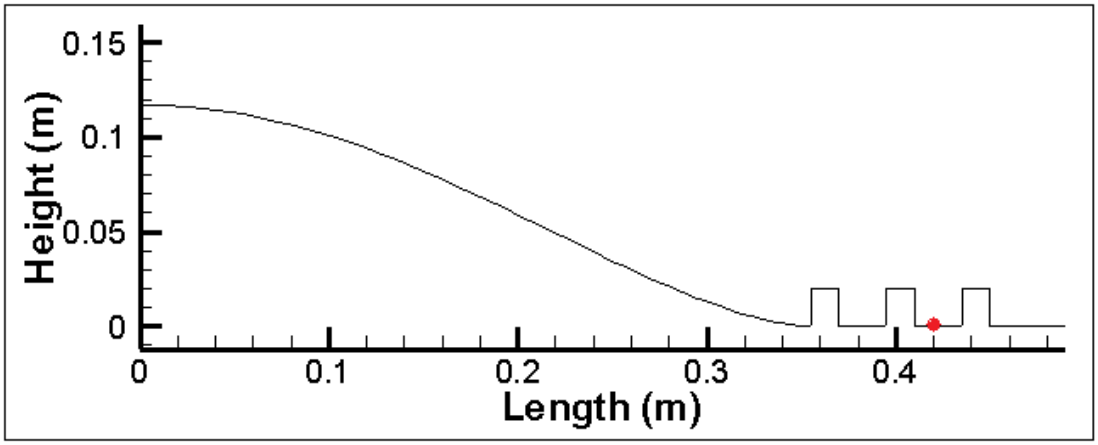

Figure 7-26 Position of collection of the data at x=0.4225m.

Figure 7-27 represents the value of mass fraction in the middle of the second street canyon (at x=0.4225m). The minimum mass fraction is given by the source located at x=0.035m and the maximum when the source is located at x=0.310m. These values have decreased (from 0.07 to 0.063 for the minimum and from 0.22 to 0.109 for the maximum) compared with the previous case, where the data were collected in the middle of the first street canyon.

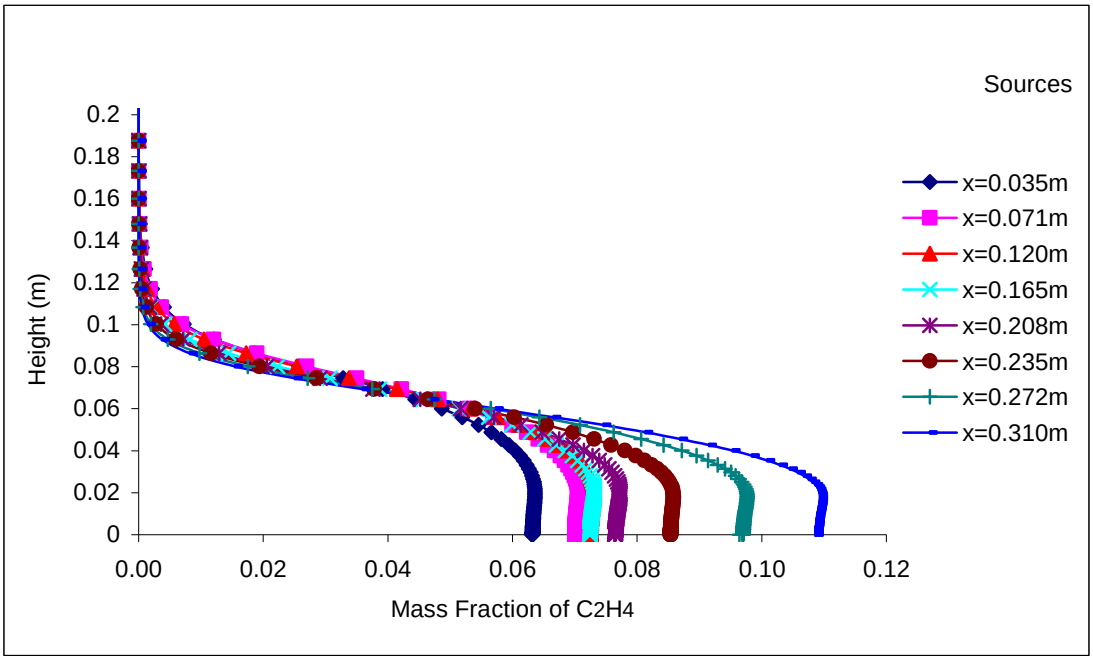

Figure 7-27 Vertical profiles of mass fraction at x=0.4225m from eight sources, for a single hill with obstacles configuration.

7.9.2. Single Hill

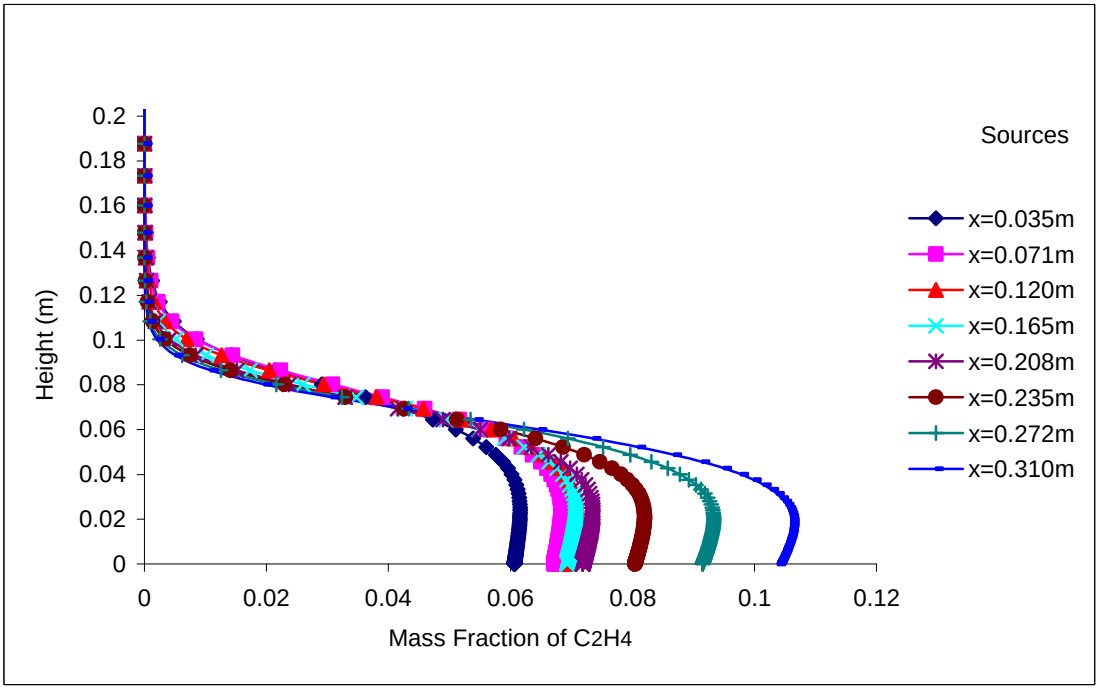

Figure 7-28 Vertical profiles of mass fraction at x=0.4225m from eight sources, for a single hill configuration.

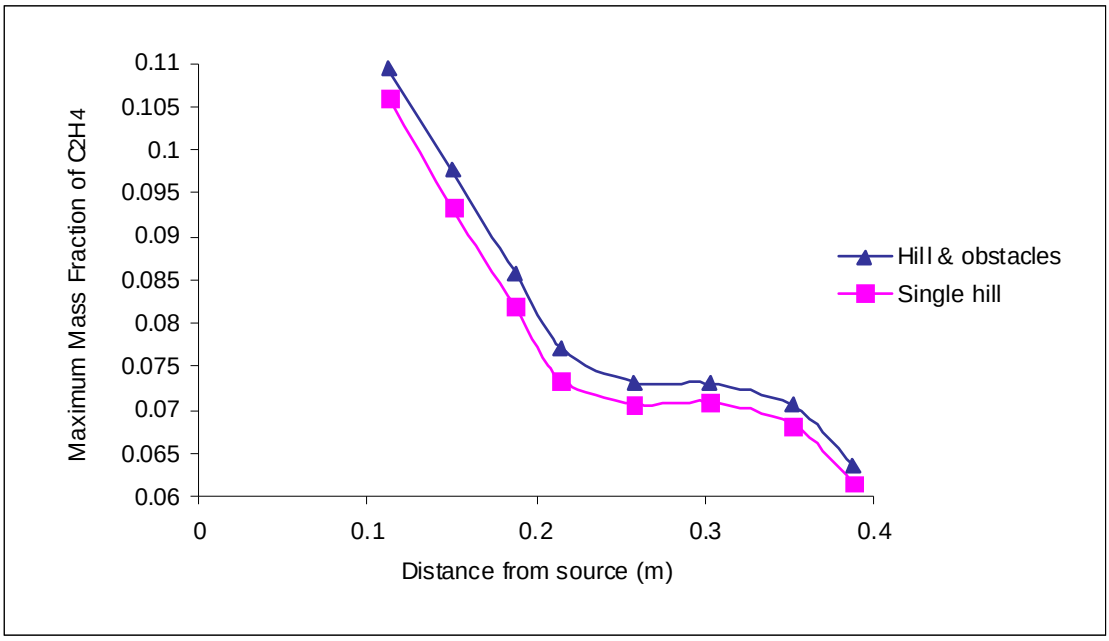

Figure 7-29 Maximum mass fraction of C_2H_4 for two cases.

In Figure 7-29 the x axis represents the distance between the point source (x_s) and the location of extracted the data (x), $(x - x_s)$. The examination of pollutant dispersion for the case of a single hill and hill with obstacles is at (0.4225,0). Figure 7-28 shows the vertical profiles of the mass fraction in the middle of the second street canyon, at x=0.4225m. For this case the values of the mass fraction have decreased and the minimum mass fraction (0.060) is obtained when the source is located at x=0.035m, and the maximum mass fraction (0.10) is obtained when the source is located at x=0.310m.

Figure 7-29 shows the mass fraction in the middle of the second street canyon (x=0.4225m) for two cases, the single hill and the hill with obstacles. It can be observed that the profile of the mass fraction in the middle of the second street canyon is higher for the case of the hill with obstacles. The same observation has been made inside the first street canyon in the same location, but in the second street canyon the mass fraction is lower than in the first canyon.

7.9.3. Flat Terrain

For the case of the flat terrain, by measuring the mass fraction in the middle of the second street canyon (x=0.4225m) it can be seen that all the values of the mass fraction are higher than the previous two cases at this specific location. For this case the minimum mass fraction is 0.11 when the source is located at x=0.035m and the maximum is 0.33 when the source is located at x=0.310m.

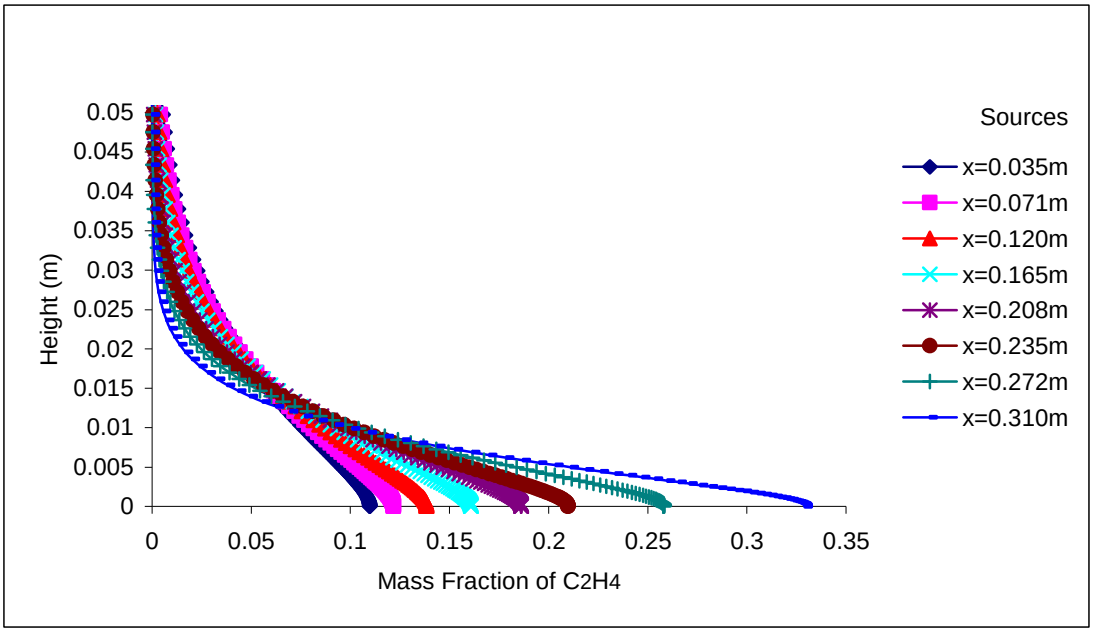

Figure 7-30 Vertical profiles of mass fraction at x=0.4225m, from eight sources, for a flat terrain configuration.

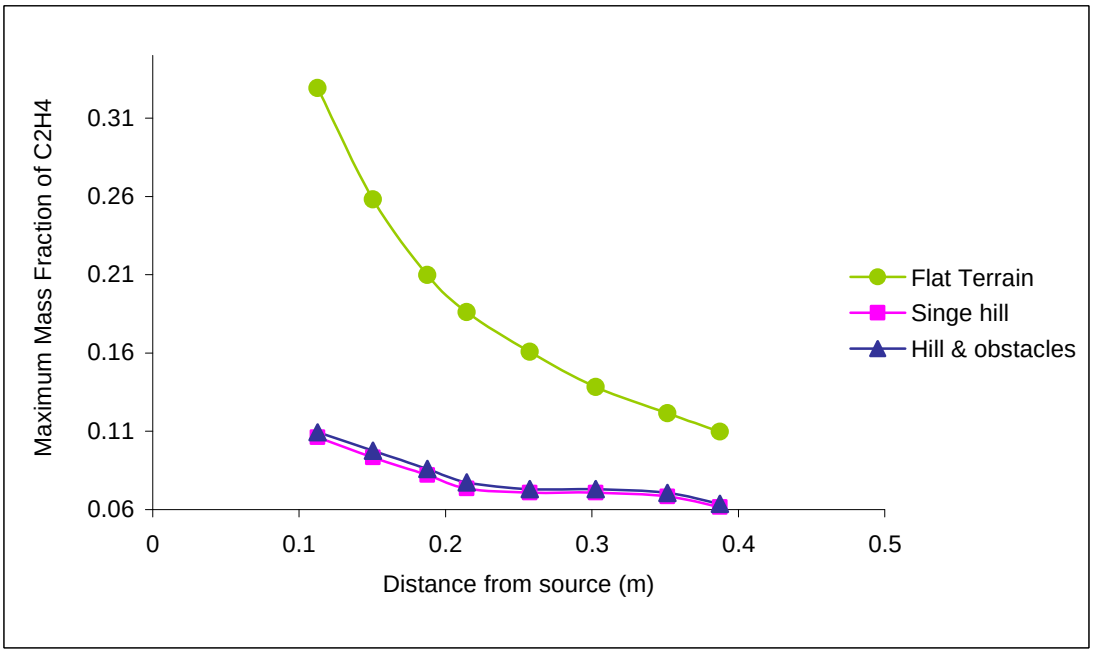

Figure 7-31 Maximum mass fraction of C_2H_4 at x=0.4225m for all cases.

In Figure 7-31 the x axis represents the distance between the point source (x_s) and the location of extracted the data (x), $(x - x_s)$. The examination of pollutant dispersion for the three cases is at (0.4225,0). Figure 7-31 represents the mass fraction in the middle of the second street canyon, for eight different source positions. The flat terrain case has the higher mass fraction, and the case with the hill and obstacles has on average 3.68% larger mass fraction than the single hill case. The flat terrain case has on average 57.04% larger mass fraction than the case of the hill with obstacles and is 58.62% larger than the case of the single hill.

7.10. Determination of ethylene mass fraction downwind of the last obstacle

7.10.1. Hill with obstacles

Figure 7-32 represents the case of the hill with obstacles and the exact location where the pollutant data are collected.

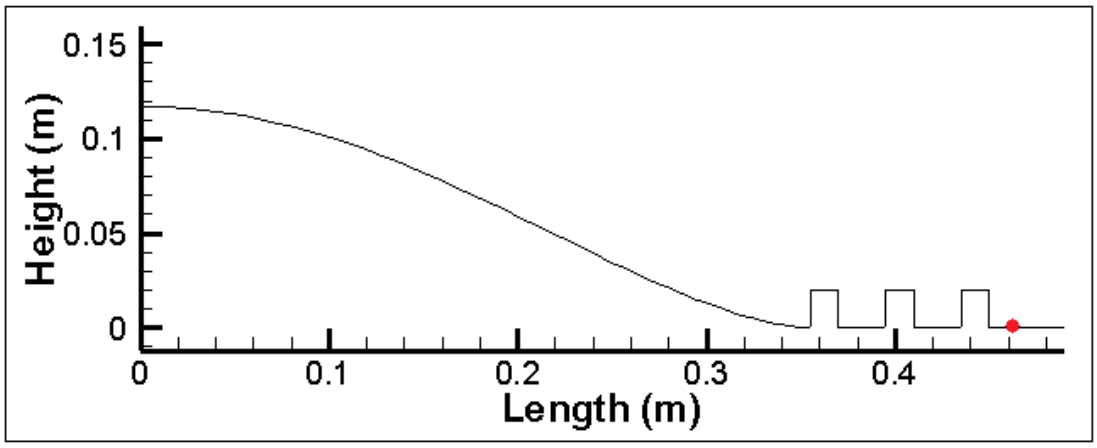

Figure 7-32 Position of collection the data at x=0.4625m.

The vertical profiles of the mass fraction at x=0.4625m, for the hill case with obstacles are represented in Figure 7-33.

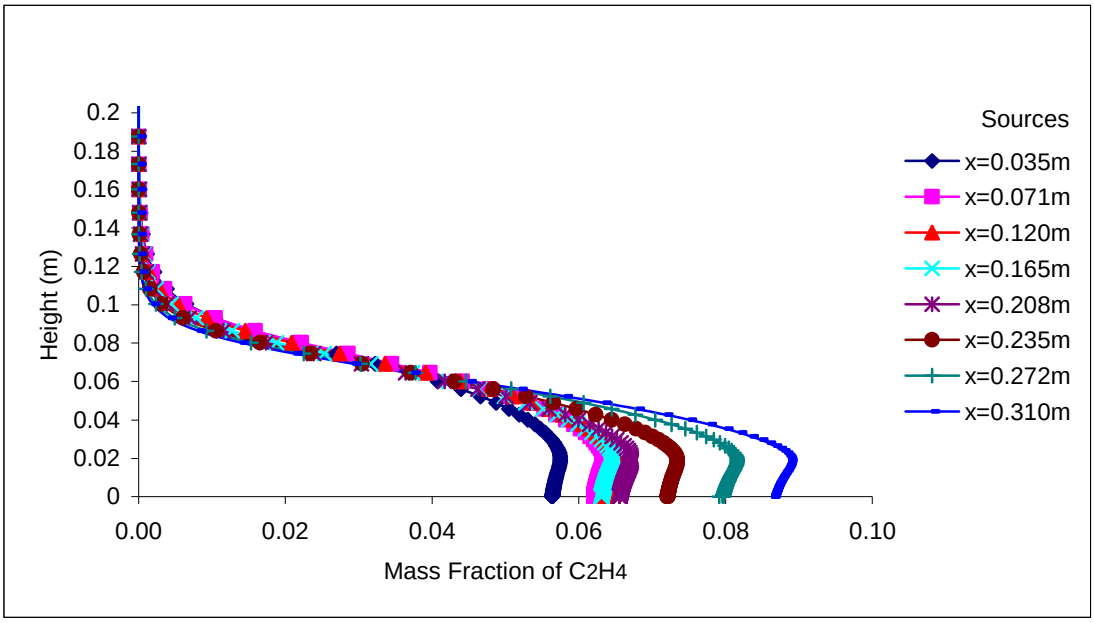

Figure 7-33 Vertical profiles of mass fraction at x=0.4625m, from eight sources, for a single hill with obstacles configuration.

In Figure 7-33, when the emissions are located at x=0.035m, the mass fraction has the lowest value (0.057) and when the source is located at x=0.310m, the mass fraction is maximal (0.088).

7.10.2. Single Hill

The vertical profiles of the mass fraction from eight sources locations for the single hill case are illustrated in Figure 7-34.

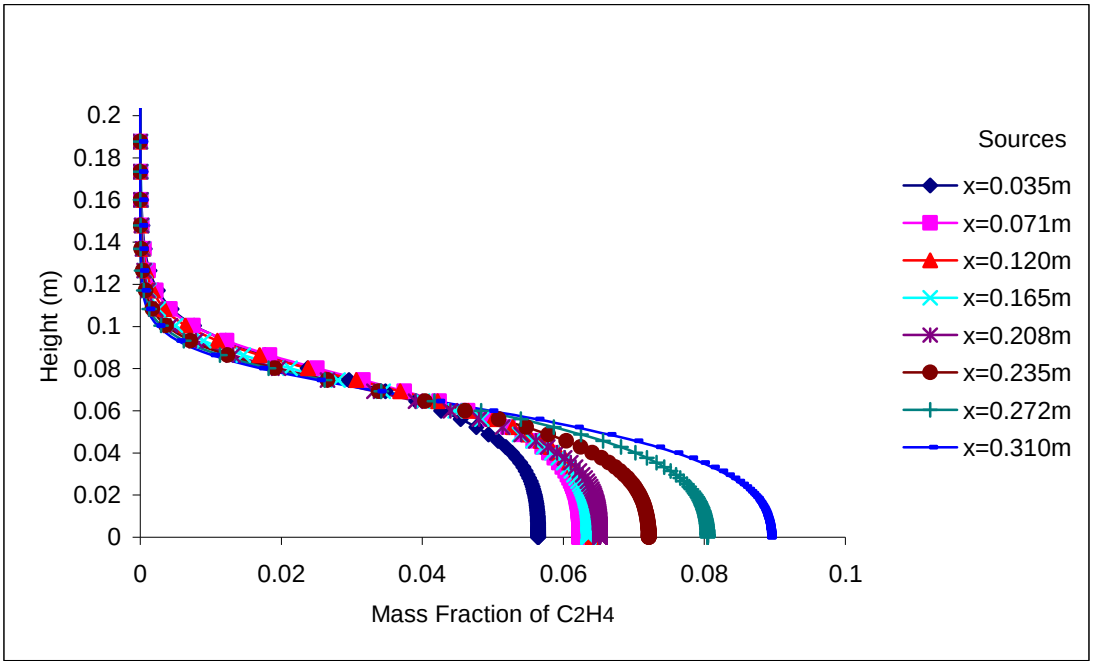

Figure 7-34 Vertical profiles of mass fraction at x=0.4625m, from eight sources, for a single hill configuration.

Downwind of the last obstacle, the minimum concentration is 0.056 and the maximum 0.089 from the sources located at x=0.035m and x=0.310m respectively. When the sources are located at x=0.120m and x=0.165m, the mass fraction is 0.064 and 0.063 respectively. This shows that two different source positions, which are far from each other, can result in very similar levels of pollutant.

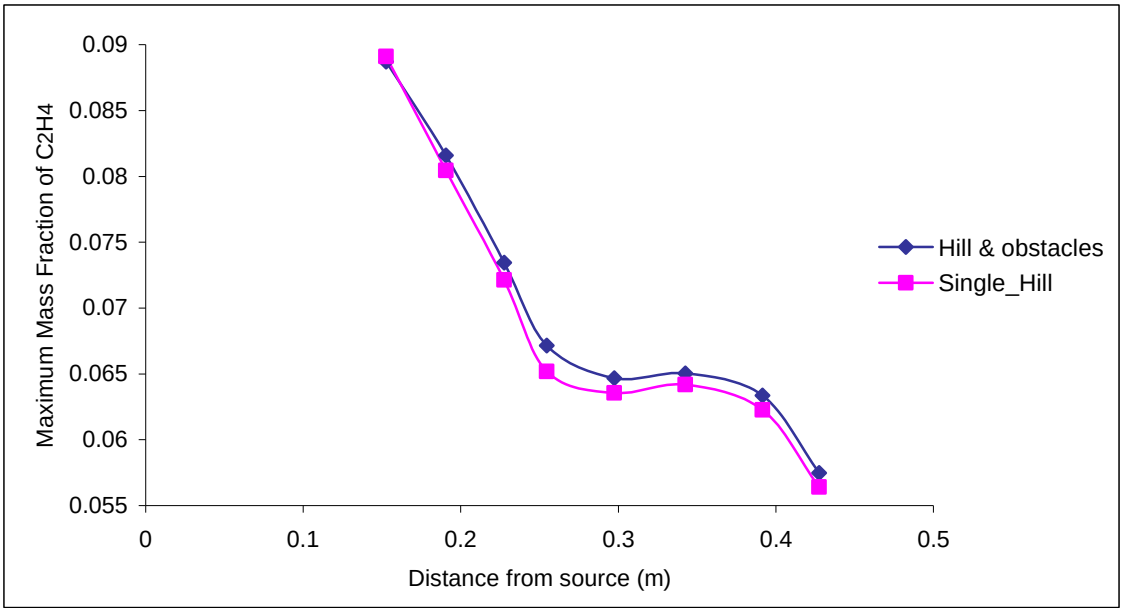

Figure 7-35 Maximum mass fraction of C_2H_4 for two cases.

In Figure 7-35 the x axis represents the distance between the point source (x_s) and the location of extracted the data (x), $(x - x_s)$. The examination of pollutant dispersion for the case of a single hill and hill with obstacles is at (0.4225,0). As well shows the mass fraction downwind of the last obstacle for two cases, the single hill and the hill with obstacles. It can be seen that the profile of the mass fraction is higher for the case of the hill with obstacles.

7.10.3.Flat Terrain

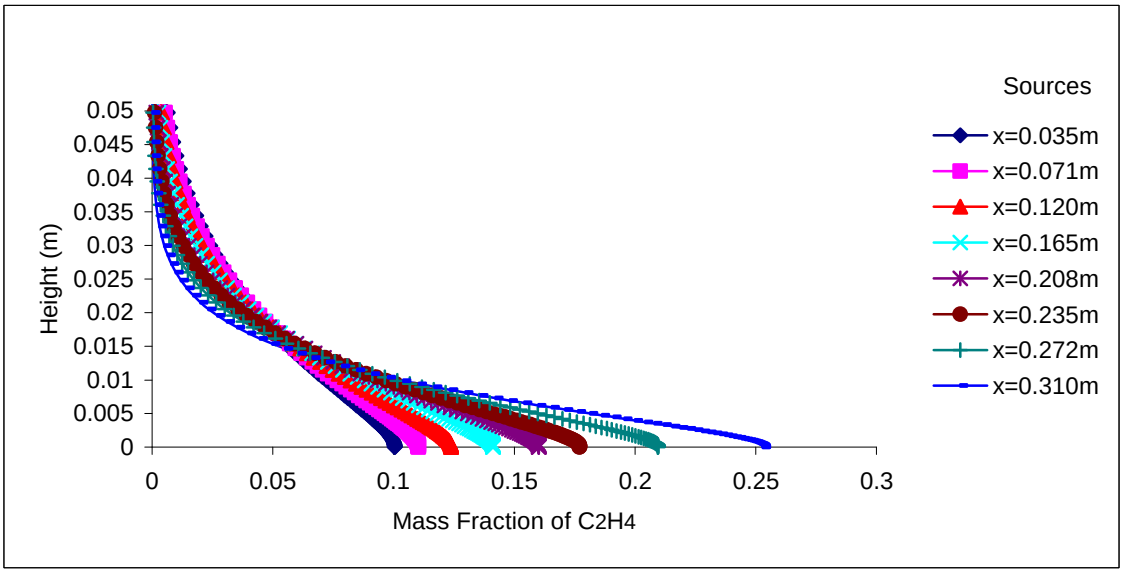

Figure 7-36 Vertical profiles of mass fraction at x=0.4625m, from eight sources, for a flat terrain configuration.

For the case of the flat terrain, measuring the mass fraction downwind of the last obstacle, it can be seen that all the values of the mass fraction are significantly higher compared to the previous cases at this specific point. When the data are collected downwind of the last obstacle, the minimum mass fraction (0.1) is obtained from the source located at x=0.035m and the maximum (0.25) from the source located at x=0.310m.

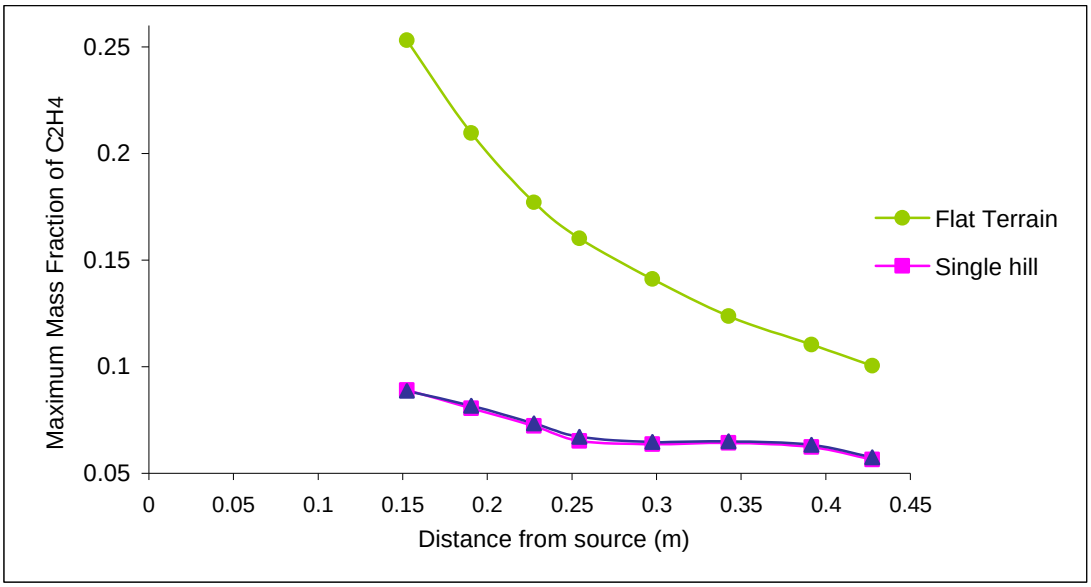

Figure 7-37 Maximum mass fraction of C_2H_4 at x=0.4625m for all cases

In Figure 7-37 the x axis represents the distance between the point source (x_s) and the location of extracted the data (x), $(x - x_s)$. The examination of pollutant dispersion for the three cases is at (0.4625,0). As well represents the mass fraction downwind of the last obstacle for all the cases. The case with the higher mass fraction is the case of the flat terrain as can be seen from Figure 7-37, which is on average 55.98% higher than the case with the hill and obstacles and 56.62% higher than the single hill case. The case with the hill and obstacles has on average 1.45% more mass fraction than the single hill case.

7.11. Characterisation of pollutant distribution: Hill with obstacles

In the previous sections, the mass fraction has been measured, upwind and downwind of the obstacles and in the middle of the street canyons. In this section the mass fraction is measured at the corner of the obstacles.

7.11.1. Upwind of the first obstacle

Figure 7-38 represents the case of the hill with the obstacles and the exact location where the data of pollutant are collected.

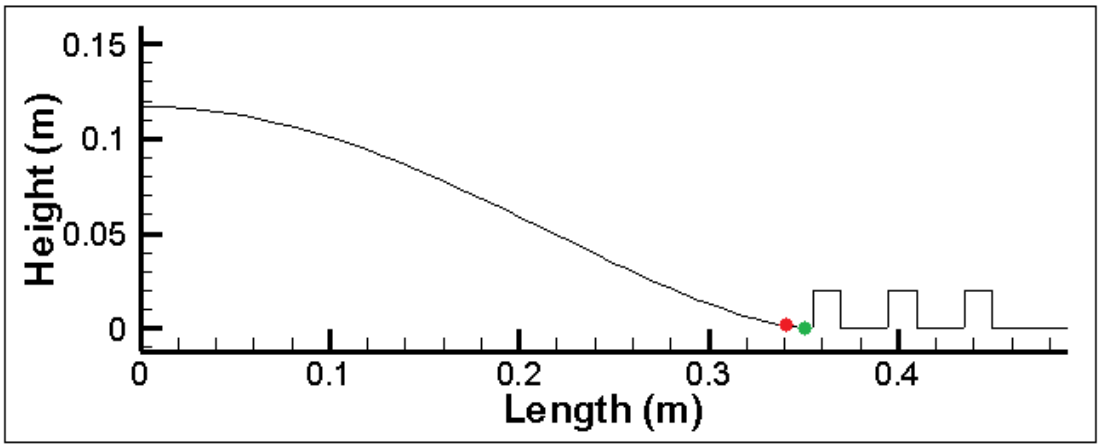

Figure 7-38 Position of data collection before the first obstacle at x=0.3425m (●) and x=0.3545m (●).

As can be seen from Figure 7-38, upwind of the first obstacle at x=0.3545m the emissions emitted from the source located at x=0.035m correspond to the minimum mass fraction. The maximum mass fraction is when the source is located at x=0.310m. The mass fraction from the sources located at x=0.120m and x=0.165m are close to each other, considering that the first source is outside the recirculation zone and the second one is inside.

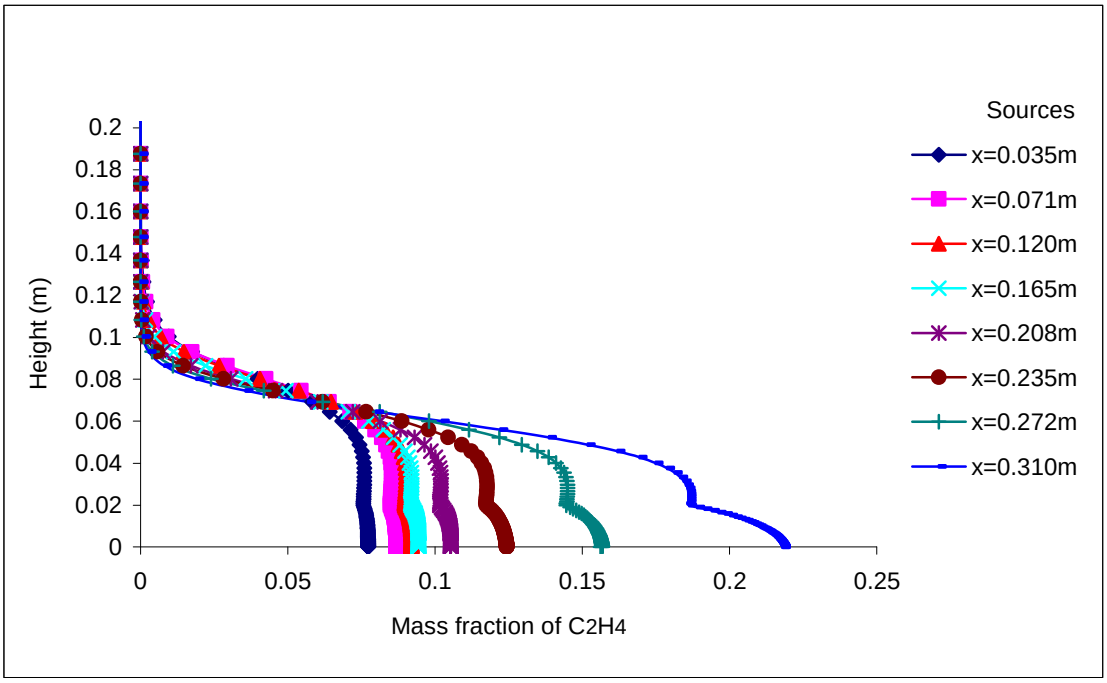

Figure 7-39 Vertical profiles of mass fraction at x=0.3545m, from eight sources, for a hill with obstacles configuration.

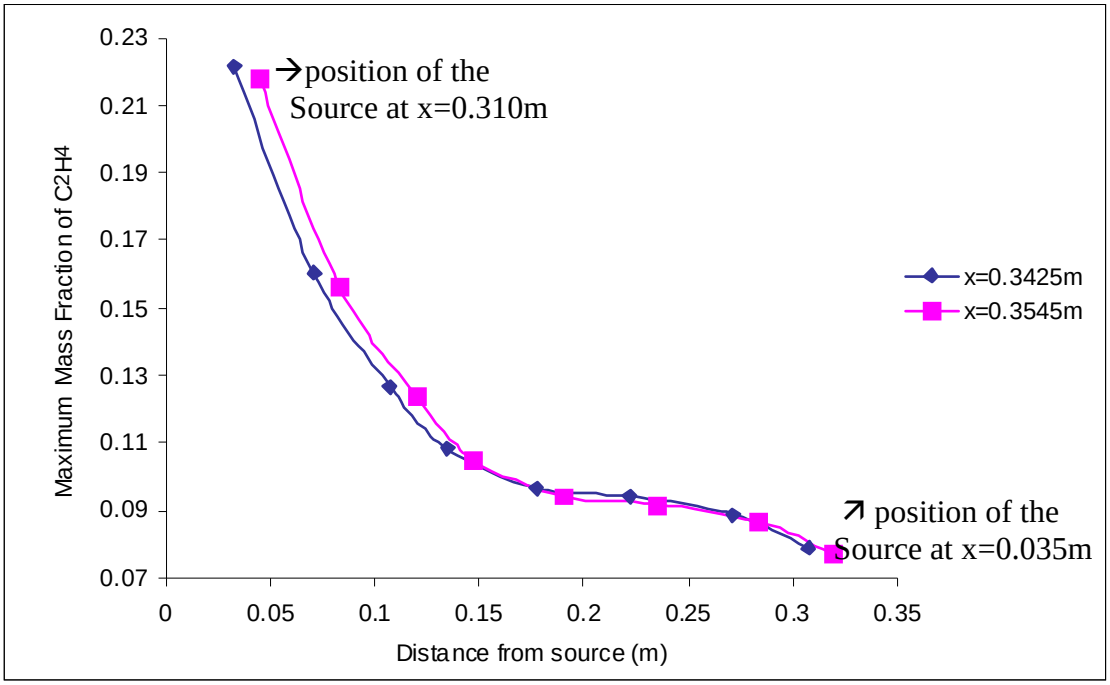

Figure 7-40 Maximum mass fraction of C_2H_4 for two cases.

For this case the data are collected at (0.3425, 0) and at (0.3545, 0) where these two positions are located upwind the first obstacle. The source of ethylene is located in various horizontal positions each time. The horizontal axis (Figure 7-40) demonstrates

the distance between the source and the position of collecting the data: $(x - x_s)$ where x is the position of collecting the data and x_s is the position of the source. The comparison of this figure is between the two positions. The first one is upwind of the first obstacle (0.3425, 0) in comparison with the second one which is the position of the point source in eight different locations along the hill, for instance (0.310, 0). This comparison has been done in order to see where the pollution is less between these two positions. This figure shows that the maximum mass fraction is when the source is located at x=0.310m and as the point sources are getting far from the area near the first obstacle then the mass fraction of ethylene is decreasing.

The mass fraction upwind of the first obstacle (at x=0.3545) is on average 2% larger than the mass fraction next to the corner of the obstacle (at x=0.3425m). This is due to the large recirculation bubble that exists before the first obstacle and also because the location where the data are collected is closer to the sources. Many streamlines pass from the locations of the emissions and go inside the big recirculation bubble. This recirculation carries the emissions and due to the clockwise flow, most of the pollutants are transferred to the region upwind of the first obstacle.

7.11.2. Inside the first street canyon

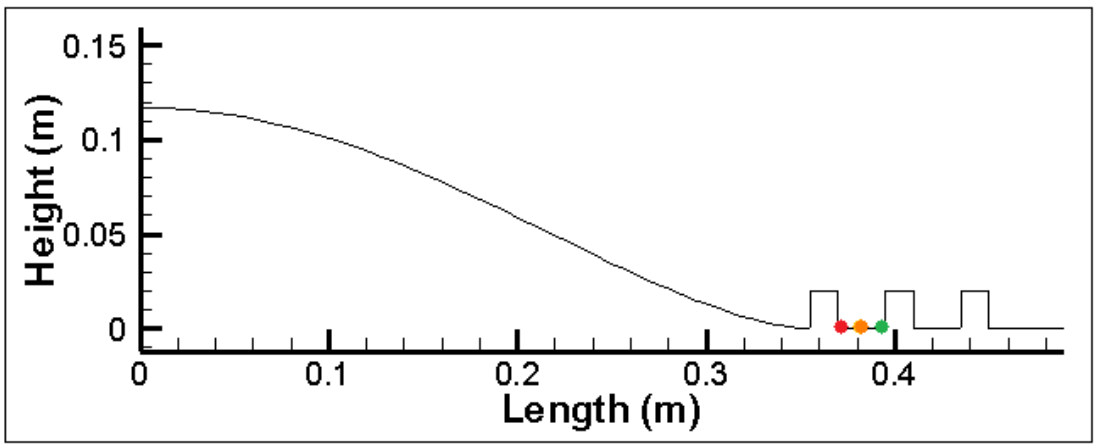

Figure 7-41 Position of collection of the data at x=0.3705m (●), x=0.3825m (●) and x=0.3945m (●).

In this section the mass fraction in the middle of the first canyon is compared with the corners of the obstacles that make up this canyon (x=0.3705m and x=0.3945m respectively).

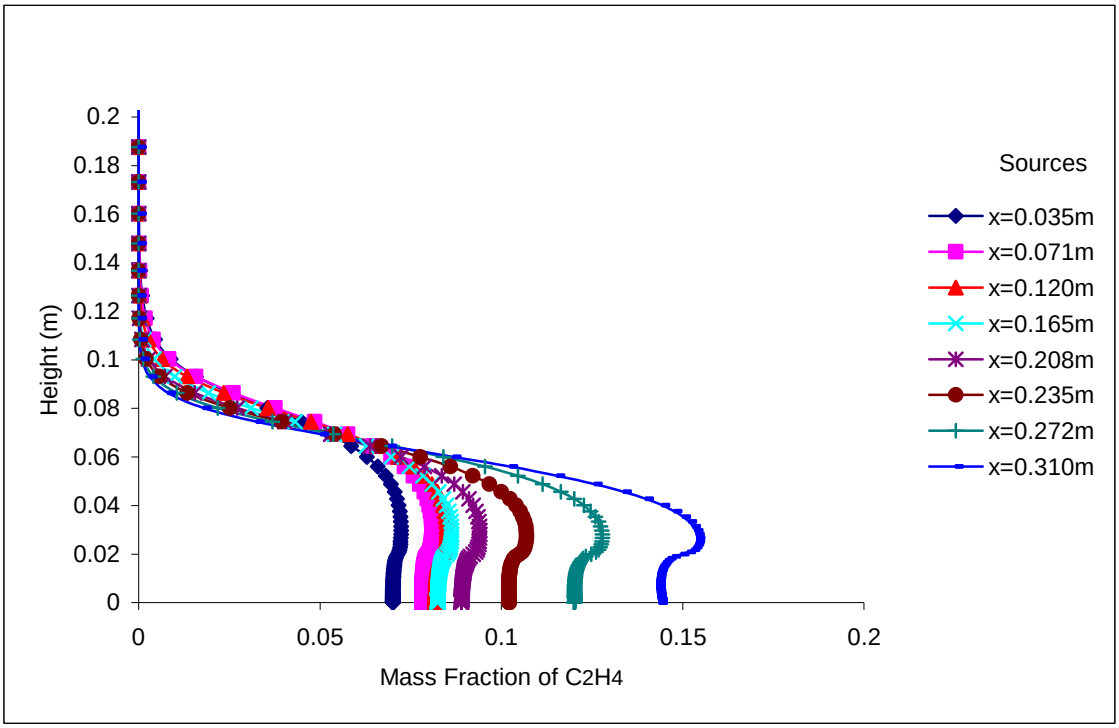

Figure 7-42 Vertical profiles of mass fraction at x=0.3705m, from eight sources, for a hill with obstacles configuration.

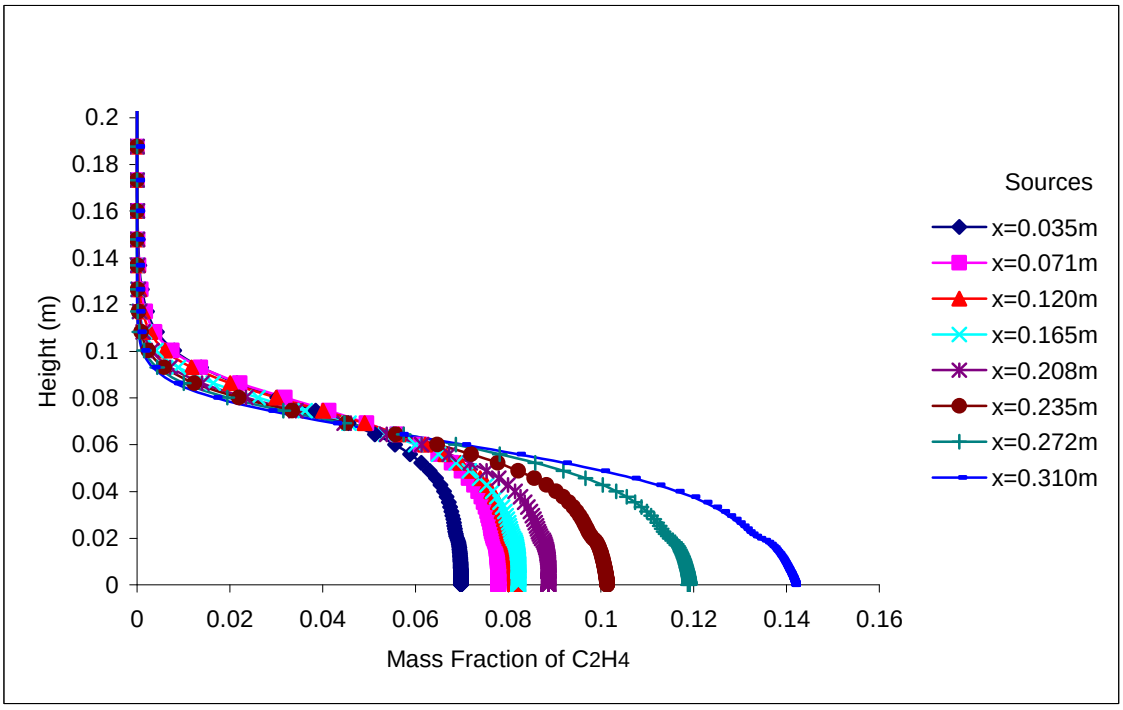

Figure 7-43 Vertical profiles of mass fraction at x=0.3945m, from eight sources, for a hill with obstacles configuration.

From Figures 7-42 and 7-43, it can be seen that when collecting the data on the bottom left corner (x=0.3705m) and bottom right corner (x=0.3945m) of the first street canyon, that the mass fraction upwind (at the bottom left corner) of the canyon is increasing more than the downwind corner when the height exceeds 0.02m which is the height of the building. This observation is shown in Figure 7-42 where the mass fraction increases significantly when the height of the obstacle is reached. In Figures 7-42 and 7-43, when the emissions are located at x=0.035m, the mass fraction has the lowest value and when the source is located at x=0.310m the mass fraction is maximal.

Figure 7-44 represents the comparison between the maximum values of the data which are measured upwind, downwind and in the middle of the first street canyon.

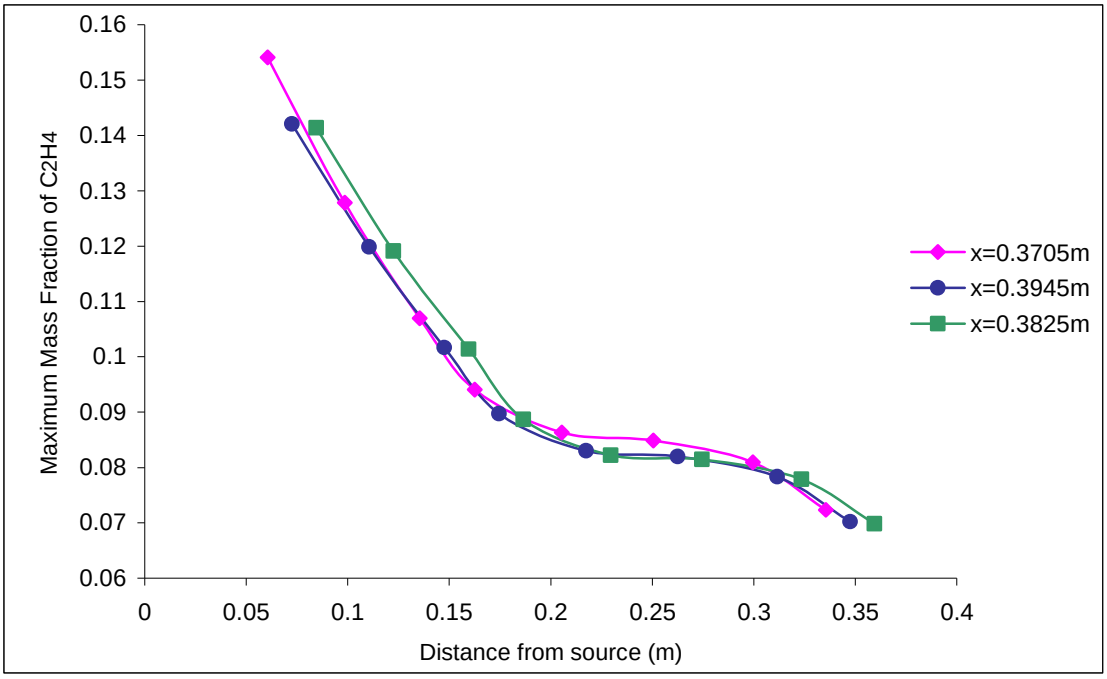

Figure 7-44 Maximum mass fraction of C_2H_4 for the upwind (x=0.3705m), middle (x=0.3825m) and downwind (x=0.3945m) inside the first canyon from eight point sources.

For this case the data are collected at (0.3705, 0) and at (0.3825, 0) and (0.3945, 0) where these three positions are located inside the first street canyon. The source of ethylene is located in various horizontal positions each time. The horizontal axis in Figure 7-44 demonstrates the distance between the point source and the position of collecting the data: $(x - x_s)$ where x is the position of collecting the data and x_s is the position of the source. In Figure 7-44 each point in the graph corresponds to one

source point. For each source point, a mass fraction is measured upwind (0.3705, 0), downwind (0.3945, 0), in the middle of the first street canyon (0.3825, 0) and the values are reported in the graph. For each position of the source the three values will be compared to each other. The mass fraction on the upwind corner of the street canyon is on average 5.2% higher than in the middle and at the downwind corner of the canyon the mass fraction is on average 0.6% higher than in the middle of the canyon. To explain the mass fraction differences inside the canyon, Figure 7-45 shows that one big vortex exists in the middle of the first canyon and two smaller vortices exist upwind and downwind.

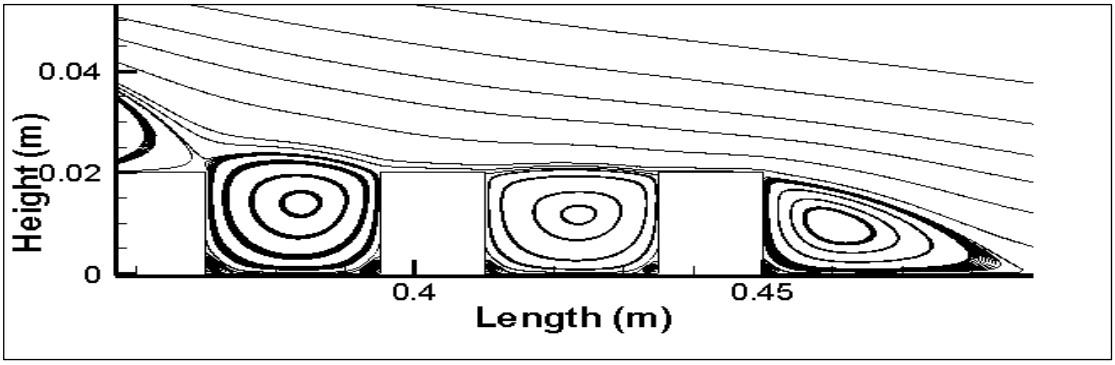

Figure 7-45 Streamlines of velocity for the case of single hill and three obstacles.

As the circulation flow is clockwise, a big recirculation exists inside the canyon, with two small vortices at its corner, which carries the emissions upwind of the canyon, resulting in a higher mass fraction in this area. The emissions are trapped inside the small vortices at the corners of the canyon.

7.11.3. Inside the second street canyon

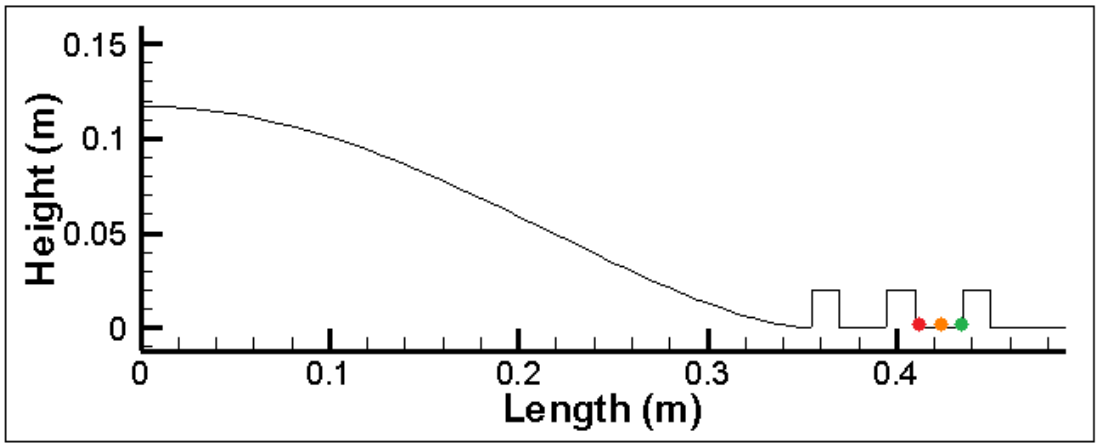

Figure 7-46 Position of collection of the data at x=0.4105m (●), x=0.4225m (●) and x=0.4345m (●).

The mass fraction inside the second canyon (upwind, downwind and in the middle) will be examined in this section as can be seen in Figure 7-46.

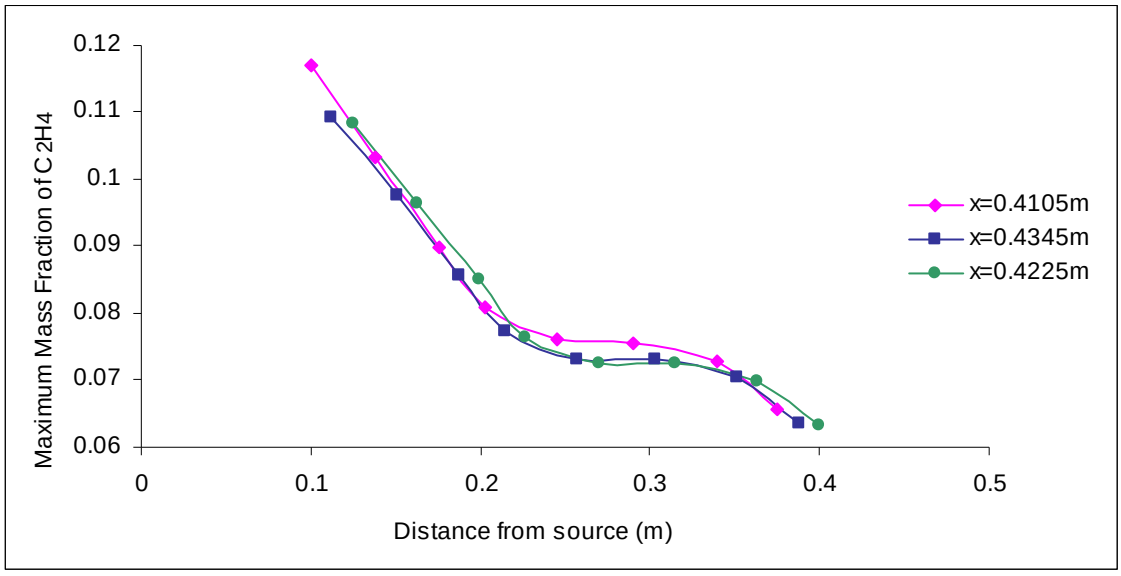

Figure 7-47 Maximum mass fraction of C_2H_4 for all cases.

For this case a mass fraction is measured upwind (0.4105, 0), downwind (0.4345, 0) and in the middle of the second street canyon (0.4225, 0). The source of ethylene is located in various horizontal positions each time. The horizontal axis in Figure 7-47 demonstrates the distance between the point source and the position of collecting the

data: $(x - x_s)$ where x is the position of collecting the data and x_s is the position of the source. In Figure 7-47 each point in the graph corresponds to one source point. As can be seen from Figure 7-47 the pollutant upwind of the street canyon is on average 4.7% higher than in the middle of the canyon. Downwind of the street canyon the pollutant is almost the same compared with the pollutant in the middle of the street canyon but has on average 0.9% higher mass fraction.

For the first and second street canyons the mass fraction at the upwind corner is higher than in the middle of the street canyon or at the downwind corner. This is due to the flow, which is clockwise, and transfers the greater part of the pollutant to the upwind corner of the canyon where the emissions are trapped. There is a small vortex as well at the downwind corner of the canyon (Figure 7-45) which also helps to trap the emissions and explain why the downwind corner has more pollutant than the middle.

7.11.4. Upwind and downwind of the first obstacle:

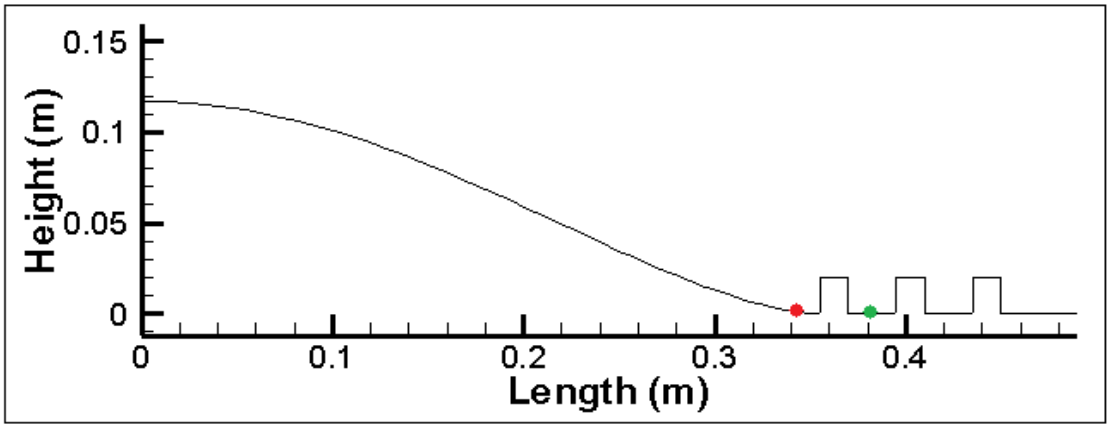

Figure 7-48 Position of collection of the data at x=0.3425m (●) and x=0.3825m (●).

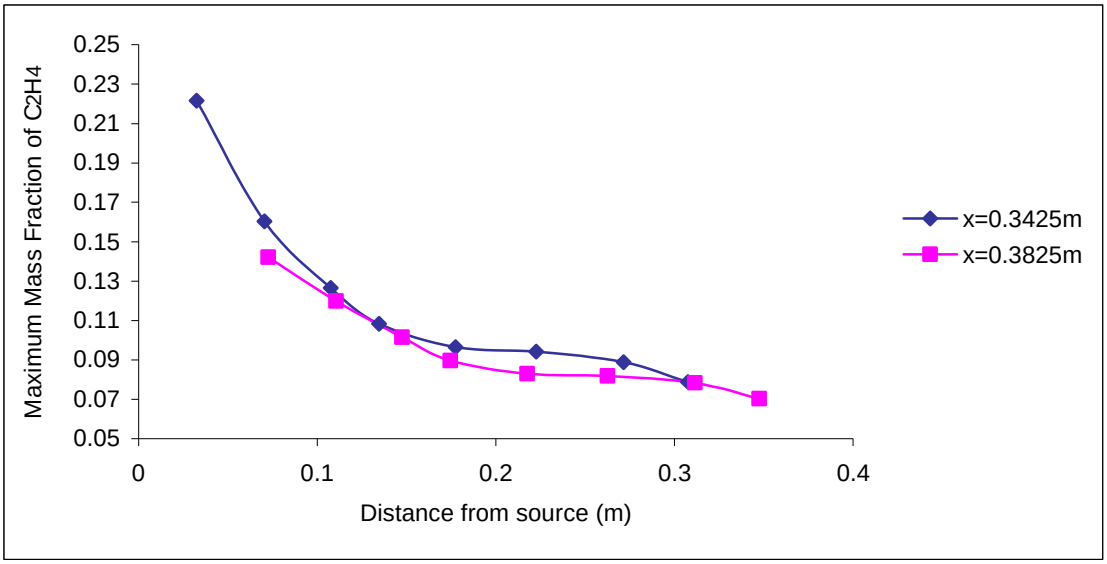

Figure 7-49 Maximum mass fraction of C_2H_4 for two cases.

For this case the data are collected at (0.3425, 0) and at (0.3825, 0) where these two positions are located upwind and downwind the first obstacle. The source of ethylene is located in various horizontal positions each time. The horizontal axis (Figure 7-49) demonstrates the distance between the source and the position of collecting the data: $(x - x_s)$ where x is the position of collecting the data and x_s is the position of the source. This comparison has been done in order to see where the pollution is less between these two positions. This figure shows that the maximum mass fraction is when the source is located at x=0.310m and as the point sources are getting far from the area near the first obstacle then the mass fraction of ethylene is decreasing. As shown in Figure 7-49 the pollutant upwind of the first obstacle (x=0.3425m) is on average 24.4% larger than downwind of it (x=0.3825m). This is due to the pollutant which comes directly from the sources along the hill and a large amount of the emissions are transferred to this region. The biggest vortex upwind of the first obstacle connects with the small vortex inside the first canyon where some of the streamlines are passing inside this canyon, so the amount of the pollutant is less important in this area than upwind of the obstacle.

7.11.5. Downwind of the last obstacle

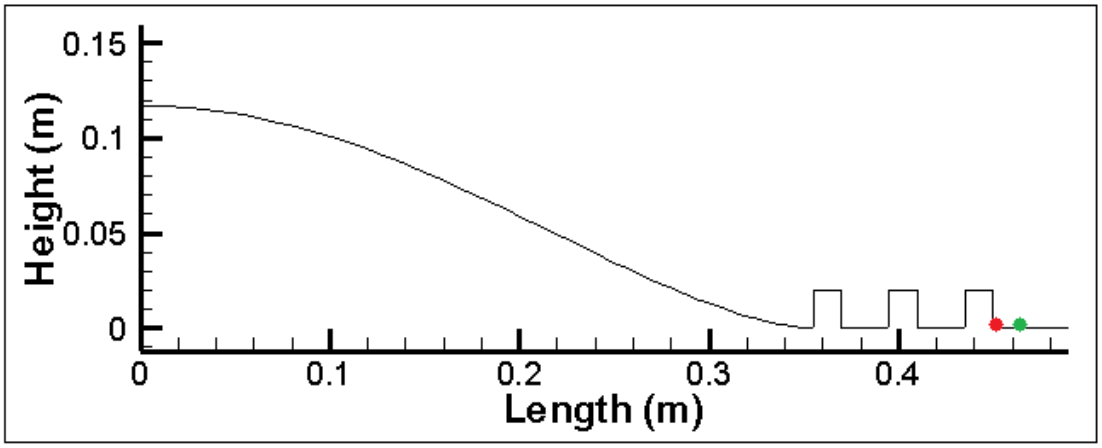

Figure 7-50 Position of collection the data at x=0.4505m (●) and x=0.4625m (●).

Figure 7-51 shows the mass fraction when the data are collected at the downwind corner of the last obstacle at (0.4505, 0). As can be seen from Figure 7-51 the emissions from the source at (0.035, 0) have the minimum mass fraction at (0.4505, 0) and the maximum pollutant is from the source located at (0.310, 0).

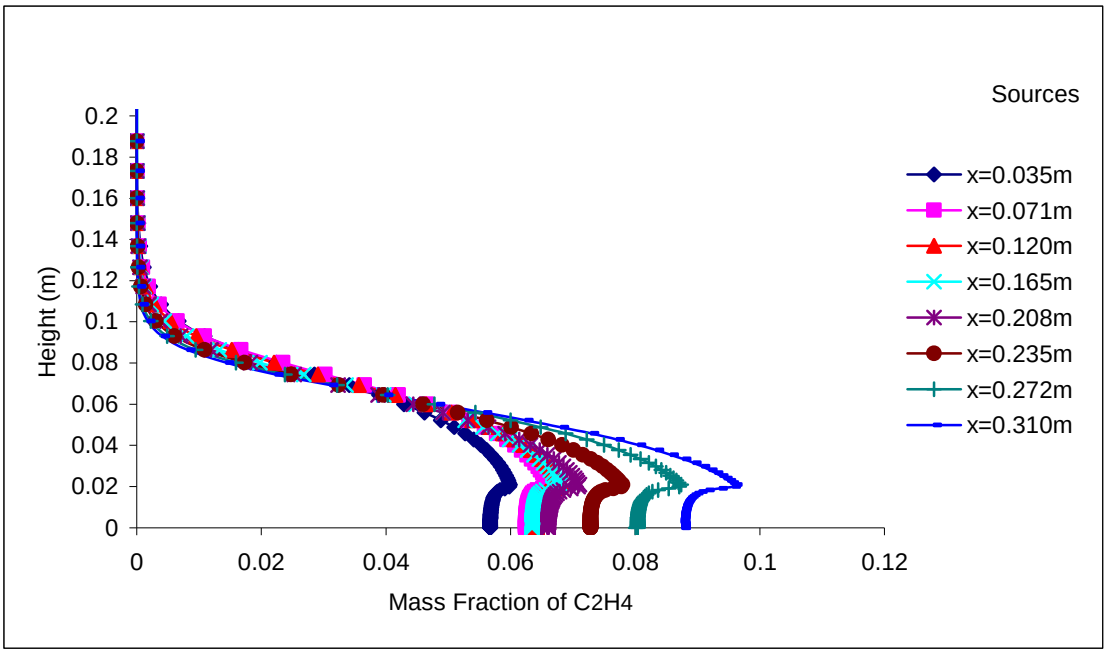

Figure 7-51 Vertical profiles of mass fraction at x=0.4505 m, from eight sources, for a hill with obstacles configuration.

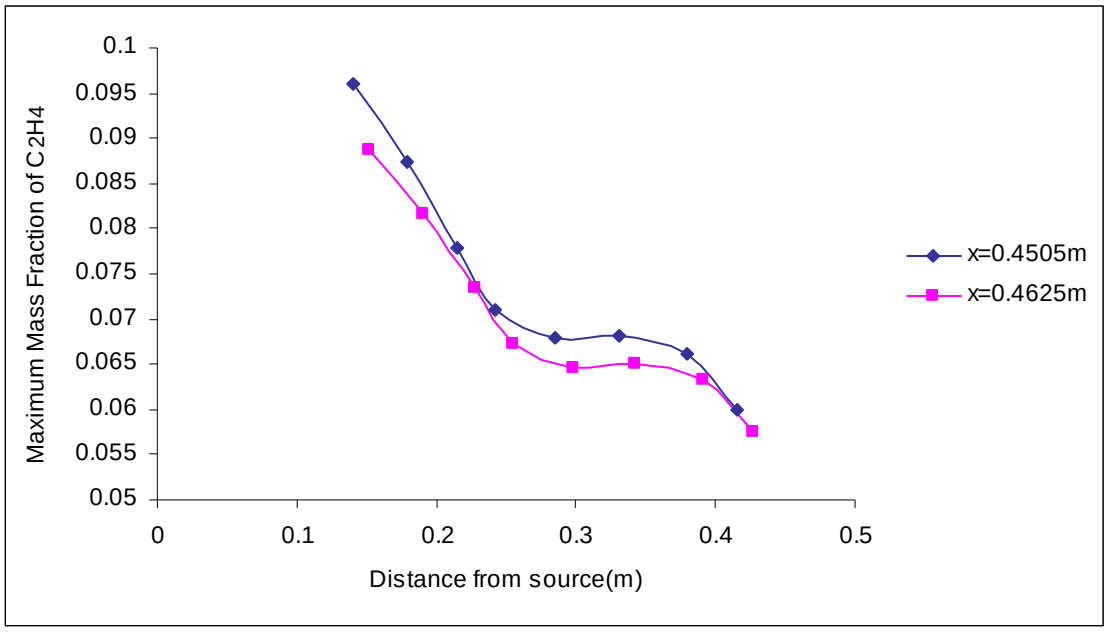

Figure 7-52 Maximum mass fraction of C_2H_4 for two cases.

Figure 7-52 shows the maximum values of the data which are measured at (0.4505, 0) and at (0.4625, 0), where these two positions are located downwind the last obstacle. The source of ethylene is located in various horizontal positions. The horizontal axis (Figure 7-52) demonstrates the distance between the source and the position of collecting the data: $(x - x_s)$ where x is the position of collecting the data and x_s is the position of the source. This figure shows that the maximum mass fraction is when the source is located closer to the obstacles and as the point sources are getting far from the area near the last obstacle then the mass fraction of ethylene is decreasing. The mass fraction when the data are collected on the left corner downwind of the last obstacle (x=0.4505m) is on average 5.5% larger than the mass fraction which is measured at (0.4625 ,0). This is due to the recirculation which exists downwind of the obstacle, where the emissions are trapped, the flow at this location is clockwise and the amount of ethylene is larger in the area next to the corner.

7.11.6. Upwind of the first and downwind of the last obstacle

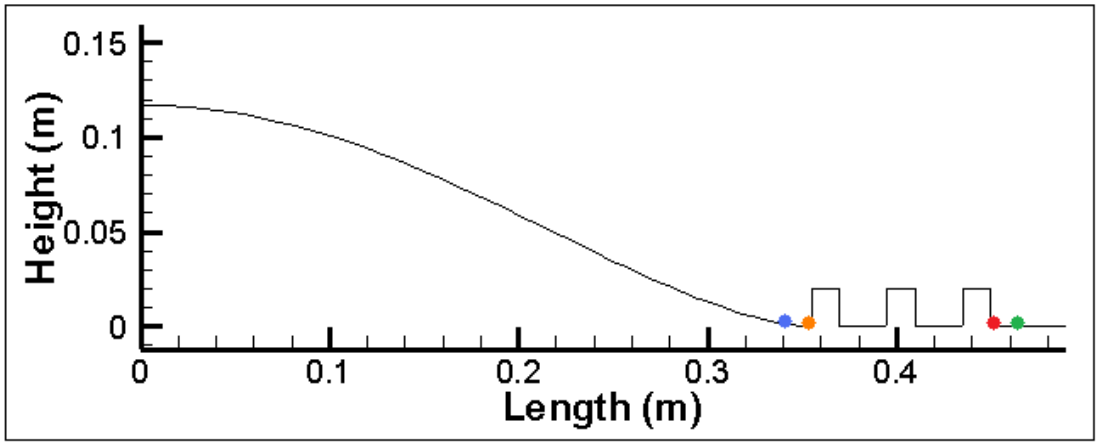

Figure 7-53 Position of collection of the data upwind of the first (x=0.3425m (●), x=0.3545m (●)) and downwind of the last obstacle (x=0.4505m (●), x=0.4625m (●))

For this case the data are collected at (0.3425, 0) and at (0.3545, 0) where these two positions are located upwind the first obstacle and at (0.4505,0), (0.4625,0) where these two positions are downwind of the last obstacle. The source of ethylene is located in various horizontal positions each time. The horizontal axis in Figure 7-54 demonstrates the distance between the source and the position of collecting the data: $(x - x_s)$ where x is the position of collecting the data and x_s is the position of the source. A difference is observed between the pollutant upwind in the first and downwind in the last obstacle (Figures 7-54). The mass fraction upwind of the first obstacle is on average 40% larger than the pollutant downwind of the last obstacle. This is due to the emissions which are in the most part transported inside the first vortex downwind of the hill and upwind of the first obstacle. Figure 7-54 demonstrates that as the data are collected far away from this first big vortex and the point sources then the mass fraction will decrease, this also explains why the amount of pollutant downwind of the last obstacle is less than upwind of the first obstacle.

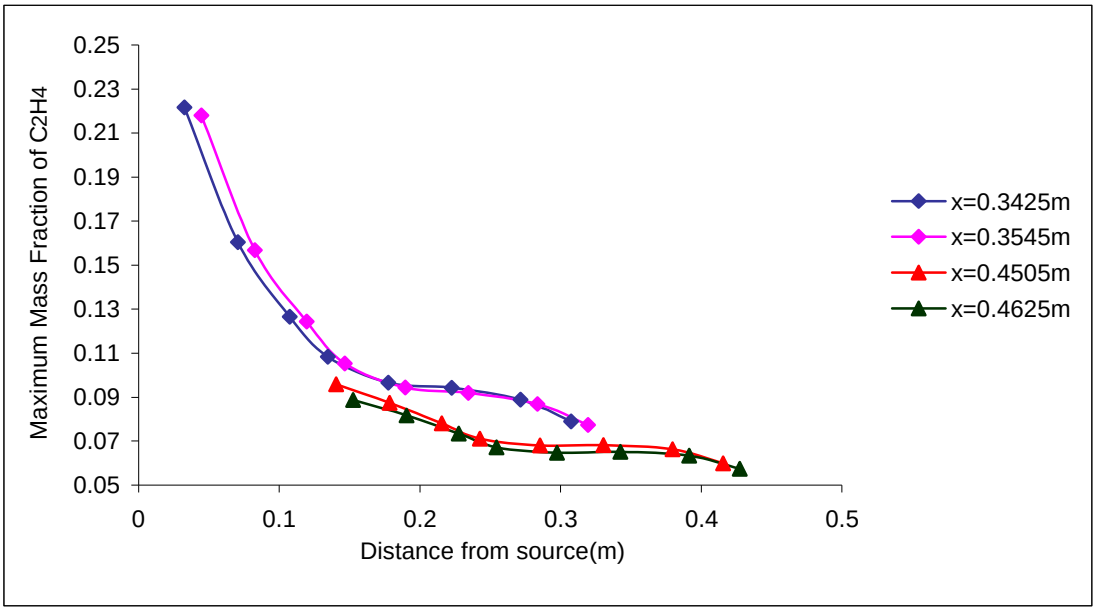

Figure 7-54 Maximum mass fraction of C_2H_4 for all cases.

7.11.7.Comparison of ethylene mass fraction inside the two street canyons

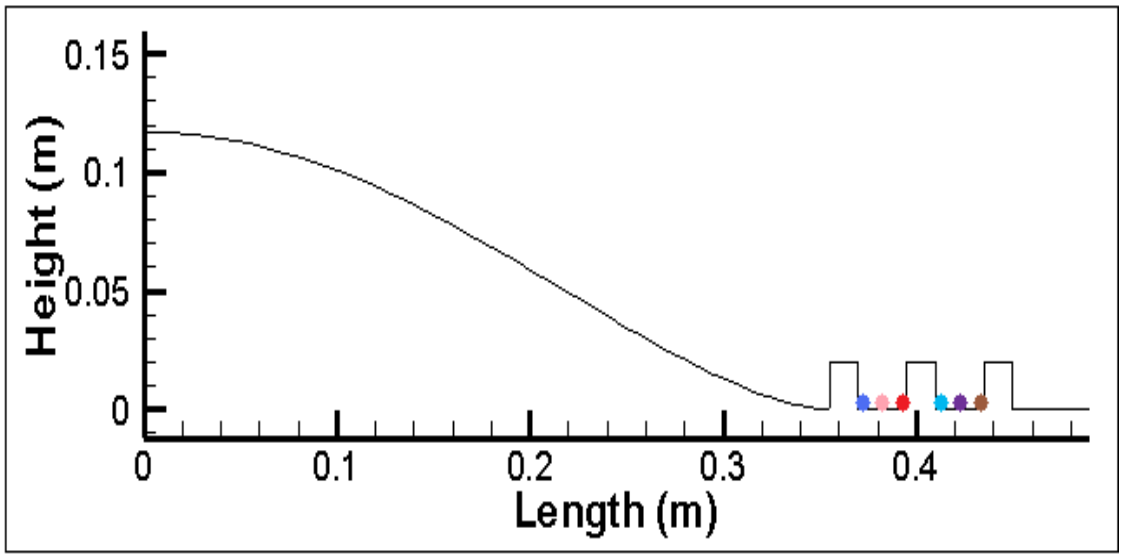

Figure 7-55 Position of collection the data inside the first (x=0.3705m (●), x=0.3825m (●), x=0.3945m (●)) and second (x=0.4105m (●), x=0.4225m (●), x=0.4345m (●)) street canyons.

For each source point, a mass fraction is measured upwind (0.3705, 0), downwind (0.3945, 0), in the middle of the first street canyon (0.3825, 0) and for the second street canyon the data are collected upwind at (0.4105, 0) downwind at (0.4345, 0) and in the middle at (0.3945,0).

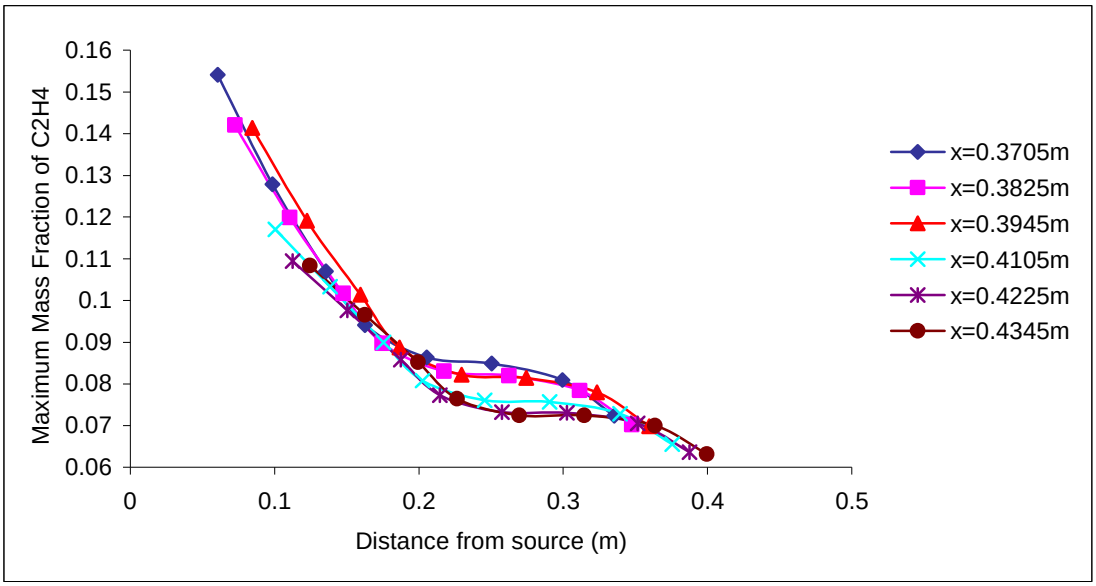

Figure 7-56 Maximum mass fraction of C_2H_4 inside the two street canyons.

The horizontal axis (Figure 7-56) demonstrates the distance between the source and the position of collecting the data: $(x - x_s)$ where x is the position of collecting the data and x_s is the position of the source. As can be seen from Figures 7-56 and 7-57, the pollutant on the left corner (0.3705, 0) of the first canyon is on average 20% larger than in the second street canyon (0.4105, 0) at the same position. On the right corner of the first street canyon (0.3945,0), the mass fraction is on average 15.4% larger than the pollutant at the right corner of the second street canyon (0.4345, 0). In the middle of the canyons, the first street canyon has on average 15.2% larger mass fraction than the second. Considering the entire canyon, the pollutant inside the first street canyon has on average 15.4% higher mass fraction than the second canyon.

Figure 7-57 shows the distribution of ethylene around the street canyons and especially in the corners.

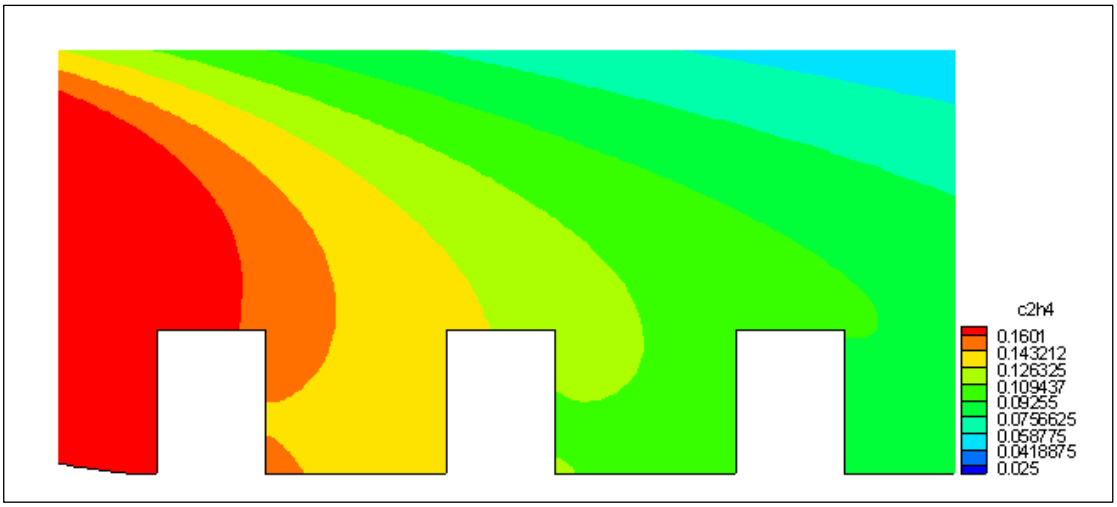

Figure 7-57 Contours of C_2H_4 Concentration.

The fact that the first canyon has more pollutant than the second is due to the big recirculation bubble along the hill. This large vortex which transports emissions connects directly with the vortices inside the first canyon and consequently the vortex inside the first street canyon is stronger than the vortex inside the second. At the corners of the canyons, the concentration of the emissions is more important than in the middle of the canyons and this is due to the small vortices which have the effect of trapping the pollutant in this area (Figure 7-57). The circulation flow is also clockwise and carries most of the emissions to these corners. Figure 7-57 shows clearly that the corners concentrate more pollutant than in the middle of the canyons.

7.12. Summary of Results

Comparisons of the mass fraction of ethylene at various locations have been made for the cases of: hill with obstacles, single hill and flat terrain when a continuous source is located at eight different positions. It has been observed that in all simulations, the maximum mass fraction of ethylene is higher in the flat terrain case.

The flat terrain simulations have been conducted in order to see how the emissions react and how the flow is developed without having any obstacle or hill to interrupt the flow. The wind comes from the left side to the right side of the domain. For the flat terrain case, nothing exists between the emissions and the location where the data are collected so the velocity will not be reduced and there will not be any recirculation zone to change the flow, so the pollutant is transferred in high concentrations from one location to another.

Comparing the single hill case with this of the hill with obstacles, it has been observed that the maximum concentration in specific positions is higher for the second case. For the case of the hill with obstacles, the pollutants are trapped inside the canyons, the vortices are moving clockwise and the pollutants are blocked between the obstacles. Without any obstacles, the pollutants do not concentrate in a specific area, except in the vortex generated by the flow over the hill. As a consequence, the case with the obstacles presents higher pollutant concentration than the single hill case at the same distance from the sources where the data are collected. By following the streamlines of Figure 7-57, how the flow affects the emissions and the concentrations of pollutant between the obstacles for the case of the hill with obstacles can be observed.

On the right side of the hill there exists a big recirculation bubble (vortex) which contains the highest mass fraction of ethylene because all the emissions are funnelled into this particular area. This first vortex, which is stronger than all the others, is connected to the vortex of the first street canyon. The vortex of the second street canyon is less connected to the first vortex but is stronger than the last vortex located downwind of the last obstacle.

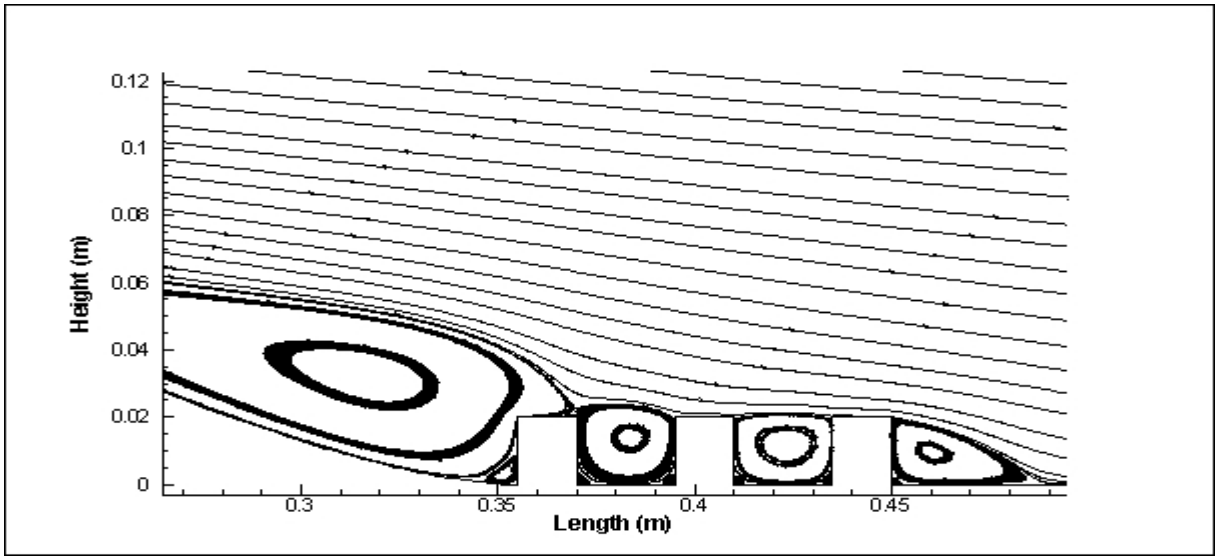

Figure 7-58 Streamlines of velocity downwind of the hill and next to the obstacles.

Consequently, the amount of pollutant transported to the first street canyon is greater than the amount carried to the second street canyon. This is because the emissions convect directly inside the first street canyon. The vortex upwind of the first obstacle which transports the largest amount of mass fraction has on average 24.4% larger mass fraction than the middle of the first street canyon.

The concentrations of pollutant 0.012m upwind of the first obstacle and next to its corner are also compared. Moreover it has been observed that the data collected upwind of the obstacle have on average 2% larger mass fraction than next to the corner of the obstacle. This is due to the emissions which are in the most part transported inside the first vortex downwind of the hill. As the data is collected further away from this first vortex the mass fraction will decrease. This also explains why the amount of pollutant upwind of the first obstacle is 40% larger than downwind of the last obstacle. Compared to downwind of the last obstacle the concentration of pollutant in the second street canyon is higher. This is because more emissions are transferred inside the second street canyon than downwind of the last obstacle.

The mass fraction on the left and right corners as well as in the middle of the first and second street canyons was examined. It has been observed for both canyons and also for the last obstacle that the left corner has the maximum mass fractions of ethylene. The presence of small vortices in each corner of the canyons (Figure 7-58) explains why in this area the mass fraction of pollutant is higher than in the middle.

The result of the circulation flow which is clockwise is to facilitate the transport of pollutants and to keep them on the left corner which presents the highest concentration of emissions.

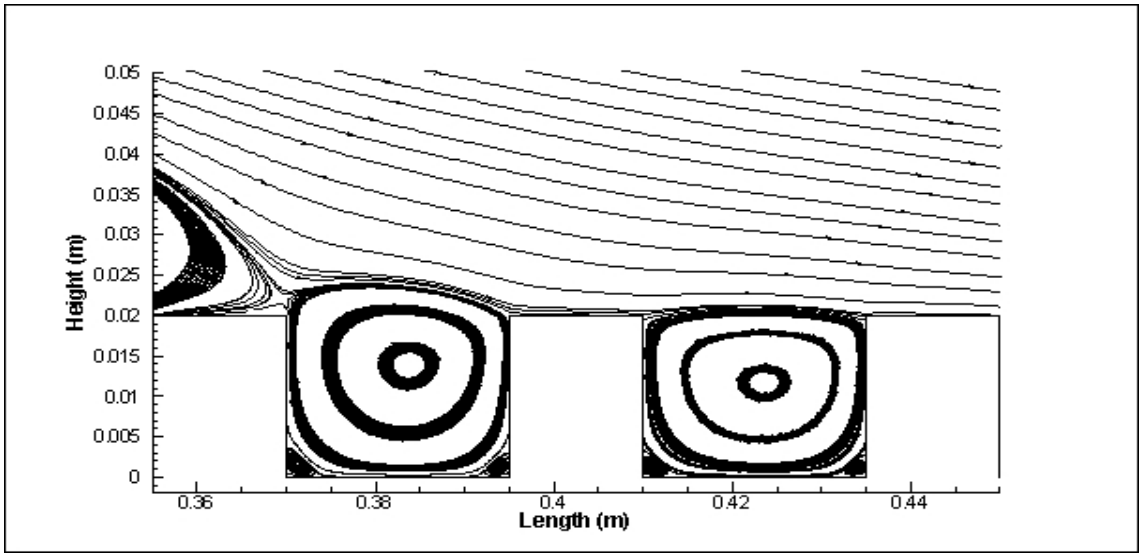

Figure 7-59 Streamlines of velocity inside the street canyons.

The mass fraction on the left corner of the first street canyon is on average 5.2% higher than in the middle of the street canyon. On the right corner the emissions are on average 0.6% higher than in the middle of the street canyon. For the second street canyon, the mass fraction on the left and the right corners is respectively 4.7% and 0.9% higher on average than at the middle of the street canyon. Measuring the mass fraction next to the corner of the last obstacle and comparing it with the mass fraction 0.012m away from this obstacle, it has been found that the mass fraction in the corner of the last obstacle is on average 5.5% larger.

Comparing the pollutant between the first and the second street canyons, the first has on average 15.4% more pollutant than the second. The pollutants on the left corner of the first canyon are 20% bigger than on the second street canyon at the same position. On the right corner of the first street canyon, the pollutants are 15.4% higher on average than the pollutants on the right corner of the second street canyon. In the middle of the canyons, the first street canyon has a 15.2% larger pollutant than the second. The fact that the first canyon has more pollutant than the second is due to the recirculation bubble which is next to the hill. In addition, it is connected more with the first street canyon than the second.

Chapter 8

8. Conclusion and Further work

The flow around a hill and obstacles with gas dispersion has been studied using CFD. This project presented a comprehensive set of results on wind flow near the hill as well as the hill with obstacles. The results included comparisons of the flow downwind of the hill, around the obstacles and inside the street canyons.

- A grid convergence study has been conducted in order to check the dependency of the results compared to four different mesh sizes. The analysis of the results has shown that the mesh with 90000 cells produces the same results as the mesh with 32000 cells, but doubles the simulation time. Therefore, the mesh with 32000 cells was used and preferred for the simulations.

  The validity of this numerical set-up developed in the present work has been assessed by comparing the obtained results with the experimental and numerical data of Khurshudyan et al. [17] and Castro and Apsley [18] respectively, with the help of the commercial software packages Fluent 6.3.26 and Tecplot 360.

- Velocity profiles at the upwind base, summit and downwind base of the hill have been validated. Additionally the validity of the emissions has been done by comparing the concentration profiles in flat terrain and also the ground level concentrations downwind of the hill for a specific height.

  Results from the performed simulations of this study have shown that between Spalart-Allmaras, k-ε Standard, k-ε RNG and k-ε Realizable turbulence models, the k-ε Standard turbulence model was acceptable and showed a good agreement with the experimental and numerical measurements.

  The k-ε Standard turbulence model, with a very fine mesh in the downwind area of the hill and around the obstacles, has better predicted the flow and has been compared well with experimental data.

- Simulations for the flat terrain case have been conducted in order to see how the emissions react and how the flow is developed with no obstacles or hill to interrupt the flow. When the ground was flat the pollutant was transferred from one location to another. The flow was completely unobstructed, unlike the other two cases.

  Some interesting features of the flow around a single hill have been presented in this study. A recirculation zone has been observed downwind of the hill. This had also been observed in the validation stage for both experimental and numerical cases examined. The study has shown that the formation of the vortex downwind of the hill resulted in a higher concentration of the pollutant in that area.

- The hill with obstacles case has shown that the area of intense recirculation was located downwind of the hill and the basic flow in the street canyon was a recirculating flow filling the canyon.
  The source points of ethylene have been located in various positions along the hill and the outcome of this study was that the hill affects the emissions. Moreover, higher pollutant concentrations have been observed around the first obstacles and this was due to the big recirculation zone which trapped most of the pollutant in these areas. When the source was placed near the middle of the recirculation bubble, the recirculation zone had a large effect on the emissions and slightly moving the source, did not vary a lot the mass fraction profiles at downwind locations.
  Comparing the single hill case with the case of the hill with obstacles showed that the maximum concentration in specific positions was higher in the second case. As mentioned above, some vortices were observed inside the street canyons.

- In this study analysis of the results has shown that the existence of the vortices helps the pollutant to be trapped near and within the canyons and the presence of obstacles has as an effect the high concentration of the pollutant.

The amount of pollutant transported to the first street canyon was greater than the amount carried to the second street canyon. This was because the first vortex downwind the hill helped the convection of the emissions directly inside the first street canyon. Compared to downwind of the last obstacle the concentration of pollutant in the first and second street canyons was higher. As the data were collected further away from this first vortex the concentration of pollutant observed decreased.

It has been observed for both canyons and also for the last obstacle that the left corner had the maximum mass fractions of ethylene and this was due to the particularity of the flow in that area. The presence of small vortices in each corner of the canyons explained why in that area the mass fraction of pollutant was higher than in the middle.

Without any obstacles, the pollutants did not concentrate in a specific area, except in the vortex generated by the flow over the hill and the obstacles.

- Study of three dimensional geometries with more building arrays could produce important results and lead to more conclusions on the improved placement of rural zones close to industrial and other hazardous areas. Another factor to consider could be the velocity of the wind, i.e. to have various wind speeds which are significantly affected by the presence of the obstacles. These simulations could be a useful tool, in the case of planning a new building area next to an industrial area or even if there was a danger of pollutants which were emitted by accident. In this case, it is possible to examine the effect of pollutants on the planned building area and how close or far the building site should be located from commercial areas.

References

[1] Merrington G., Winder L., Parkinson R., Redman M., Agricultural Pollution, Environmental Problems and Practical Solutions, Taylor and Francis Group, Spon Press, 2002

[2] Krupa S.V. Air Pollution, People and Plants, Aps Press, The American Phytopathological Society, 1977

[3] Mavroidis I., Grifiths R.F., Local characteristics of atmospheric dispersion within building arrays, Atmospheric Environment 35 (2001) 2941}2954

[4] Boris J. The threat of chemical and biological terrorism: Preparing a response, US Naval Reasearh Laboratory, pp. 22-31

[5] Thornber B., CFD for Environmental Flows, Lecture notes 2009 (unpublished), Fluid Mechanics & Computational Science, Cranfield University

[6] Pope S.B., Turbulent Flows, Cambridge University Press, 2000

[7] Barratt R., Atmospheric Dispersion Modelling: An Introduction to Practical Application, Earthscan. London, Sterling, VA, (2001)

[8] Kim J-J , Baik J-J, Chun H-Y, Two-dimensional numerical modelling of flow and dispersion in the presence of hill and buildings, J.Wind Eng. Ind. Aerodyn., 89 (2001) 947-966.

[9] Griffiths A.D., Middleton J.H., Simulations of separated flow over two-dimensional hills, J.Wind Eng.Ind.Aerodyn.98 (2010), 155-160

[10] Ferreira A.D., Lopes A.M.G., Viegas D.X., Sousa A.C.M., Experimental and numerical simulation of flow around two-dimensional hills, J. Wind Eng.Ind.Aerodyn 54/55 (1995) 173-181

[11] Pearse J.R., Lindley D., Stevenson D.C., Wind flow over ridges in simulated atmospheric boundary layers, Depart.Mechanic.Engin.,1980

[12] Gayev, Y. and E. Savory, 1999: Influence of street obstructions on flow processes with urban canyons, J. Wind Eng. & Ind. Aerodyn., 82, 89-103).

[13] Meroney R.N., Wind-tunnel simulation of the flow over hills and complex terrain, Journal of industrial Aerodynamics, 5 (1980) 297-321

[14] Carpenter P., Locke N., Investigation of wind speeds over multiple two-dimensional hills, Journal of Wind Engineering and Industrial Aerodynamics 83 (1999) 109-120

[15] Pearse J.R., Wind flow over conical hills in a simulated atmospheric boundary layer, J.Wind.Eng.Ind.Aerodyn., 10 (1982) 303-313

[16] Castro I.P. and Snyder W.H., A wind tunnel study of dispersion from sources downwind of three-dimensional hills, Atmospheric Environment Vol.16, No.8, pp.1869-1887, (1982)

[17] Khurshudyan L.H., Snyder W.H. and Nekrasov I.V, Flow dispersion of pollutants over two dimensional hills. United States Environmental Protection Agency Report EPA-600/4-81-067, (1981)

[18] Castro I.P and Apsley D.D, Flow and dispersion over topography: a comparison between numerical and laboratory data for two dimensional flows, Atmospheric Environment Vol.31, No.6, pp.839 850,(1997)

[19] Arya S.P.S., Capuano M.E. and Fagent L.C., Some fluid modelling studies of flow and dispersion over two-dimensional low hills, Atmospheric Environment Vol.21.No.4.pp.753-764, (1987)

[20] Lai N.T.N and Chan A.T., Pollutant dispersion by a turbulent wind flow near a low hill

[21] Young-Rae J., Keun P., Warn-Gyun P., Ok-Hyun P., Numerical analysis of flow and pollutant dispersion over 2-D bell shaped hills, International Journal, Vol. 17 No.7, pp.1054 -1062, (2003)

[22] Egan B.A.,Transport and diffusion in complex terrain. Boundary-Layer Met.30, 3-28), (1984)

[23] Arya S.P.S, Gadiyaram P.S. An experimental study of dispersion in the wakes of three-dimensional low hills. J Atmospheric Environment 1986; 20(4):129–40

[24] Finardi S., Morselli M.G., Jeannet P., Wind Flow Models over Complex Terrain for Dispersion Calculations, Cost Action 710, Pre-processing of Meteorological Data for Dispersion Models, Report of Working Group 4, (May 1997)

[25] Mello P.E.B., Yanagihara J.I., Numerical prediction of gas concentrations and fluctuations above a triangular hill within a turbulent boundary layer, J. Wind Eng. Ind. Aerodyn. 98 (2010) 113–119

[26] Apsley,D.D., Castro,I.P., 1997. Flow and dispersion over hills: comparison between numerical predictions and experimental data. Journal of Wind Engineering and Industrial Aerodynamics 67,375–386

[27] Bocon, F.T.,Maliska,C.R.,2000.Application of an anisotropic turbulence model to stable atmospheric flows and dispersion over 3D topography. Journal of the Brazilian Society of Mechanical Sciences 22,105–118

[28] Chatzipanagiolidis A., Olivary D., Pollutant dispersal downstream of a hill in different wind conditions, Wind Eng. Ind. Aerodyn, 64 (1996) 233-248

[29] Nicholson S.E., Air pollution model for street level air, Atmos. Environ. 9 (1975) 19–31.

[30] Oke T.R., Street design and urban canopy layer climate, J. Energy Buildings 11 (1988) 103–113.

[31] Stathopoulos T., Storms R., Wind environmental conditions in passages between buildings, Journal of Wind Engineering and Industrial Aerodynamics, 24 (1986) 19-31

[32] Chang C-H, Meroney R.N., Concentration and flow distributions in Urban street canyons: wind tunnel and computational data, J. Wind Eng. Ind. Aerodyn., 91 (2003) 1141-1154

[33] Meroney, R.N., Leitl, B.M., Rafailidis, S., Schatzmann, M., 1999. Wind-tunnel and numerical modelling of flow and dispersion around several building shapes. Journal of Wind Engineering and Industrial Aerodynamics 81, 333–345

[34] Zhang Y.Q., Huber A.H., Arya S.P.S., Snyder W.H., Numerical simulation to determine the effects of incident wind shear and turbulence level on the flow around a building, J. Wind Eng.Ind.Aerodyn.46&47 (1993) 129-134

[35] Castro I.P., Robins A.G., The flow around a surface-mounted cube in uniform and turbulent streams, J. Fluid Mech.70 (1977) 307-335

[36] Chang P.C., Wang P.N., A. Lin, Turbulent diffusion in a city street, Proceedings of the Symposium on Air Pollution and Turbulent Diffusion, Las Cruces, New Mexico, 1971, pp. 137–144

[37] Higson, H.L., Griffiths, R.F., Jones, C.D., Hall, D.J., 1996. Flow and dispersion around an isolated building. Atmospheric Environment 30 (16), 2859–2870

[38] Wedding J.B., Lombardi D.J., Cermak J.E., A wind tunnel study of gaseous pollutants in city street canyons, J. Air Pollut. Control Assoc. 27 (1977) 557–566

[39] Mavroidis, I., Griffiths, R.F., Hall, D.J., 2003. Field and wind tunnel investigations of plume dispersion around single surface obstacles. Atmospheric Environment 37 (21), 2903–2918

[40] Snyder W.H., Guide line for fluid modelling of atmospheric diffusion, Report No. 600/8-81-009, USEPA, Research Triangle Park, NC 27711, 1981.

[41] Delaunay D., Numerical and wind tunnel simulation of gas dispersion around a rectangular building, J.Wind Eng.Ind.Aerodyn.67-68 (1997) 721-732

[42] Robins, A.G., Castro, I.P., 1977. A wind tunnel investigation of plume dispersion in the vicinity of a surface mounted cube-I. The flow field. Atmospheric Environment 11, 291–297

[43] Robins, A.G., Castro, I.P., 1977. A wind tunnel investigation of plume dispersion in the vicinity of a surface mounted cube-II. The concentration field. Atmospheric Environment 11, 299–311

[44] Galani A., Neofytou P., Venetsanos A., Bartzis J., Neville S., Prediction and study of pollutant dispersion in a street canyon in London using computational fluid dynamics techniques, Global NEST Journal, Vol 11, No 4, pp 434-439, 2009

[45] Hoydysh W.G., Ogawa Y., Griffiths R.A., A scale model study of dispersion of pollution in street canyons, APCA Paper No. 74–157, 67th Annual Meeting of the Air Pollution Control Association, Denver, CO, 9–13 June 1974

[46] Ahmad K., Khare M., Chaudhry K.K. ,Wind tunnel simulation studies on dispersion at urban street canyons and intersections—a review, Journal of Wind Engineering and Industrial Aerodynamics 93 (2005) 697–717

[47] Ogawa, Y., Oikawa, S., Uehara, K., 1983. Field and wind tunnel study of the flow and diffusion around a model cube – I. Flow measurements. Atmospheric Environment 17, 1145–1159

[48] Blocken B., Carmeliet J., Stathopoulos T., CFD evaluation of wind speed conditions in passages between parallel buildings-effect of wall-function roughness modifications for the atmospheric boundary layer flow, Journal of Wind Engin.Industrial Aerodyn. 95 (2007) 942-962

[49] Stathopoulos, T., Wu, H., Bedard, C., 1992. Wind environment around buildings: a knowledge-based approach. J. Wind Eng. Ind. Aerodyn. 41–44, 2377–2388

[50] Chu A.K.M., Kwok R.C.W., Yu K.N., Study of pollution dispersion in urban areas using Computational Fluid Dynamics (CFD) and Geographic Information System (GIS), Environmental Modelling & Software 20, (2005) 273-277

[51] Tampieri F., Trombettti F., Giostra U., A case study of dispersion in the lee of an obstacle, Vol.13C, N.6, (1990)

[52] Kim J-J., Baik J-J, Effects of inflow turbulence intensity on flow and pollutant dispersion in an urban street canyon, Journal of Wind Engineering and Industrial Aerodynamics 91 (2003) 309-329

[53] Vardoulakis S. Fisherb B.E.A, Pericleousa K. Gonzalez-Flescac N., Modelling air quality in street canyons: a review, Atmospheric Environment 37 (2003) 155–182

[54] Baik J-J and Kim J-J., A numerical study of flow and pollutant dispersion characteristics in urban street canyons, Journal of applied Meteorology,Vol.38, (1998)

[55] Sagrado A.P.G., van Beeck J., Rambaud P., Olivari D., Numerical and experimental modelling of pollutant dispersion in a street canyon, Journal of Wind Engineering and Industrial Aerodynamics 90 (2002) 321–339

[56] Vardoulakis S., Fisher B.E.A., Pericleous K., Gonzalez-Flesca N., Modelling air quality in street canyons: a review, Atmospheric Environment 37 (2003) 155–182

[57] Nazridoust K., Ahmadi G., Airflow and pollutant transport in street canyons, Journal of Wind Engineering and Industrial Aerodynamics 94(2006)491-522

[58] Ayata T., Investigation of building height and roof effect on the air velocity and pressure distribution around the detached house in Turkey, Applied Thermal Engineering 29 (2009) 1752-1758

[59] Davidson M.J., Snyder W.S., Lawson R.E., Hunt J.C.R., Wind tunnel simulations of plume dispersion through groups of obstacles, Atmospheric Environment Vol. 30, No. 22, pp. 3715 3731, 1996

[60] Cao S., Tamura T., Experimental study on roughness effects on turbulent boundary layer flow over a two-dimensional steep hill, J.Wind Eng.Ind.Aerodyn 94 (2006) 1-19

[61] Arya S.P.S., Gadiyaram P.S., An experimental study of flow and dispersion in the wakes of three dimensional low hills, Atmos. Environ. 20 (1986) 729–740

[62] Franke J., Hirsch C., Jensen A.G., Krus H.W., Schatzmann M., Westbury P.S., Miles S.D.,Wisse J.A., Wright N.G., Recommendations on the use of CFD in predicting pedestrianwind environment, Cost Action C14,"Impact of Wind and Storms on the City life and built Environment", Working group 2-CFD techniques, Version 1.0. (2004)

[63] Massey B., Ward-Smith J., Mechanics of Fluids, 8th edition, Taylor and Francis Group (2005)

[64] Narasimhan S., Chaen K., Stenger F., The solution of Incompressible Navier-Stokes Equations using the Sinc Collocation Method, 2000 Inter Society Conference on Thermal Phenomena.

[65] Wilcox D.C, Turbulence Modeling for CFD, DCW Industries, 2006.

[66] Modeling Turbulent flows, (2010). http://turbulencecontrol.com/tuboard/board/table/papers/upload/Fluent.05.turbulence.ppt (Accessed 14th March 2010)

[67] Fluent Users Guide, http://my.fit.edu/itresources/manuals/fluent6.3/help/index.htm , (Accessed 10th March 2010)

[68] Cleaver P., Johnson M., Ho B., A summary of some experimental data on LNG safety, Journal of Hazardous Materials 140 (2007) 429-438, Available online 20 October 2006

[69] Material Safety Data Sheet, Airgas, http://www.ebsinfo.com/Tech-pdf-files/MSDS-Ethylene.pdf, (Accessed 20th March 2010)

[70] Ethylene Production and Manufacturing Process, (2010). http://www.icis.com/V2/Chemicals/9075778/ethylene/process.html , (Accessed 20th March 2010).

Appendix A

UDF only for the single hill case without emissions:

```
#include "udf.h"

DEFINE_PROFILE(inlet_x_velocity, thread, index) /* velocity in x-direction */
{

double position[ND_ND];
double y;
face_t f;
double Zo = 0.00016;
double h=0.9838;

begin_f_loop(f, thread)
{
 F_CENTROID(position, f, thread);
     y = position[1];
  //F_PROFILE  (f, thread, index)=y;
if (y>h) F_PROFILE(f, thread, index)= 4;
else F_PROFILE(f, thread, index)= 0.4585*log(y/Zo);
}
end_f_loop(f, thread)
}

DEFINE_PROFILE(kinetic_energy, thread, index)
{

double position[ND_ND];
double y;
double h=0.9838;
face_t f;

begin_f_loop(f, thread)
{
 F_CENTROID(position, f, thread);
     y = position[1];

if (y>0.9*h) F_PROFILE(f, thread, index)= 0.1178*pow((1-0.9*h/h),2);
else F_PROFILE(f, thread, index)= 0.1178*pow((1-y/h),2);
}
end_f_loop(f, thread)
}

DEFINE_PROFILE(dissipation_rate, thread, index)
{

double position[ND_ND];
```

```
double y;
double h=0.9838;
double Cm=0.09;
double k=0.41;
double ken;
face_t f;

begin_f_loop(f, thread)
{
 F_CENTROID(position, f, thread);
    y = position[1];

if (y>0.9*h) ken= 0.1178*pow((1-0.9*h/h),2);
else ken=0.1178*pow((1-y/h),2);
F_PROFILE(f, thread, index)= pow(Cm,0.75)*pow(ken,1.5)/(k*y);
}
end_f_loop(f, thread)
}
```

UDF only for the single hill case with emissions:

```
#include "udf.h"

DEFINE_PROFILE(inlet_x_velocity, thread, index) /* velocity in x-direction */
{

double position[ND_ND];
double y;
face_t f;
double Zo = 0.00016;
double h=0.9838;

begin_f_loop(f, thread)
{
 F_CENTROID(position, f, thread);
    y = position[1];
  //F_PROFILE  (f, thread, index)=y;
if (y>h) F_PROFILE(f, thread, index)= 4;
else F_PROFILE(f, thread, index)= 0.4585*log(y/Zo);
}
end_f_loop(f, thread)
}

DEFINE_PROFILE(kinetic_energy, thread, index)
{

double position[ND_ND];
double y;
double h=0.9838;
face_t f;
```

```
begin_f_loop(f, thread)
{
 F_CENTROID(position, f, thread);
    y = position[1];

if (y>0.9*h) F_PROFILE(f, thread, index)= 0.1178*pow((1-0.9*h/h),2);
else F_PROFILE(f, thread, index)= 0.1178*pow((1-y/h),2);
}
end_f_loop(f, thread)
}

DEFINE_PROFILE(dissipation_rate, thread, index)
{

double position[ND_ND];
double y;
double h=0.9838;
double Cm=0.09;
double k=0.41;
double ken;
face_t f;

begin_f_loop(f, thread)
{
 F_CENTROID(position, f, thread);
    y = position[1];

if (y>0.9*h) ken= 0.1178*pow((1-0.9*h/h),2);
else ken=0.1178*pow((1-y/h),2);
F_PROFILE(f, thread, index)= pow(Cm,0.75)*pow(ken,1.5)/(k*y);
}
end_f_loop(f, thread)
}

DEFINE_SOURCE(emissions, c, t, dS, eqn)
{
  double position [ND_ND];
  double H = 0.117;
  double source;
  double A=0.047;
  double d=1.178;
  double x1=351*0.001;
  double x2=361.826*0.001;
  double y1=57.11*0.001;
  double y2=59.78*0.001;

  C_CENTROID(position, c, t);
  dS[eqn] = 0;
```

```
  if (position[0] <x2  && position[1] <y2 &&  position[0] >x1  && position[1] >y1)
  source = d*(C_U(c,t))*A / C_VOLUME(c,t);
else
source = 0.;
  return source;
}
```

UDF for the cases of flat terrain, single hill and hill with obstacles (for example for the emissions located at x=0.310m):

```
#include "udf.h"

DEFINE_PROFILE(inlet_x_velocity, thread, index) /* velocity in x-direction */
{

double position[ND_ND];
double y;
face_t f;
double Zo = 0.00016;
double h=0.9838;

begin_f_loop(f, thread)
{
 F_CENTROID(position, f, thread);
     y = position[1];
  //F_PROFILE  (f, thread, index)=y;
if (y>h) F_PROFILE(f, thread, index)= 4;
else F_PROFILE(f, thread, index)= 0.4585*log(y/Zo);
}
end_f_loop(f, thread)
}

DEFINE_PROFILE(kinetic_energy, thread, index)
{

double position[ND_ND];
double y;
double h=0.9838;
face_t f;

begin_f_loop(f, thread)
{
 F_CENTROID(position, f, thread);
     y = position[1];

if (y>0.9*h) F_PROFILE(f, thread, index)= 0.1178*pow((1-0.9*h/h),2);
else F_PROFILE(f, thread, index)= 0.1178*pow((1-y/h),2);
}
end_f_loop(f, thread)
}
```

```
DEFINE_PROFILE(dissipation_rate, thread, index)
{

double position[ND_ND];
double y;
double h=0.9838;
double Cm=0.09;
double k=0.41;
double ken;
face_t f;

begin_f_loop(f, thread)
{
 F_CENTROID(position, f, thread);
    y = position[1];

if (y>0.9*h) ken= 0.1178*pow((1-0.9*h/h),2);
else ken=0.1178*pow((1-y/h),2);
F_PROFILE(f, thread, index)= pow(Cm,0.75)*pow(ken,1.5)/(k*y);
}
end_f_loop(f, thread)
}

DEFINE_SOURCE(emissions, c, t, dS, eqn)
{
  double position [ND_ND];
  double source;
  double y1;
  double y2;
  double A=0.047;
  double d=1.178;
  double u=0.09;
  double x1=308.78*0.001;
  double x2=311.12*0.001;

  C_CENTROID(position, c, t);
  dS[eqn] = 0;
  y1=-0.34*position[0]+115.7652*0.001;
  y2=-0.34*position[0]+115.6752*0.001;

  if (position[0] <x2  && position[1] >y2 &&  position[0] >x1  && position[1] <y1)
{
  source = fabs(d*u*A / C_VOLUME(c,t));
  printf("And the source is: %f at %f for velocity %f\n",source,position[0],C_U(c,t));
}
else
source = 0;
  return source;
}
```

Appendix B

Second-Order Upwind Scheme

When second-order accuracy is desired, quantities at cell faces are computed using a multidimensional linear reconstruction approach. In this approach, higher-order accuracy is achieved at cell faces through a Taylor series expansion of the cell-centered solution about the cell centroid. Thus when second-order upwinding is selected, the face value ϕ_f is computed using the following expression:

$$\phi_{f,sou} = \phi + \nabla_\phi \cdot \vec{r}$$

Where ϕ and ∇_ϕ are the cell-centered value and its gradient in the upstream cell, and $\vec{r}$ is the displacement vector from the upstream cell centroid to the face centroid. This formulation requires the determination of the gradient ∇_ϕ in each cell. Finally, the gradient ∇_ϕ is limited so that no new maxima or minima are introduced. Second-order upwind is available in the pressure-based and density-based solvers.